ADA051534

⑫

6 ONE METER KrF LASER SYSTEM.

10 J.C. Hsia, J.H. Jacob, J.A. Mangano and M. Rokni

Avco Everett Research Laboratory, Inc.
2385 Revere Beach Parkway
Everett MA 02149

11 22 Aug 77   13 104 p.

9

Semi-Annual Report. 23 February 77 to 22 August 77.

15 N00014-76-C-1032, DARPA order—3125

APPROVED FOR PUBLIC RELEASE; DISTRIBUTION UNLIMITED.

DDC FILE COPY.

D D C
RECEIVED
MAR 21 1978
D

048 450

FOREWORD

DARPA Order No.: 3125

Program Code No.:

Contractor: Avco Everett Research Laboratory, Inc.

Effective Date of Contract: August 23, 1976

Contract Expiration Date: November 23, 1977

Contract No.: N00014-76-C-1032

Short Title of Work: One Meter KrF Laser System

Principal Investigator and Phone No.: J.A. Mangano,
(617) 389-3000, Ext. 725

Scientific Officer: Director Physics Program, Physical Sciences Div.
Office of Naval Research
800 North Quincy Street
Arlington, VA 22217

Amount of Contract: $588,758

REPORT DOCUMENTATION PAGE		READ INSTRUCTIONS BEFORE COMPLETING FORM
1. REPORT NUMBER	2. GOVT ACCESSION NO.	3. RECIPIENT'S CATALOG NUMBER
4. TITLE (and Subtitle) One Meter KrF Laser System		5. TYPE OF REPORT & PERIOD COVERED Semi Annual Report 23 Feb. 1977 - 22 Aug. 1977
		6. PERFORMING ORG. REPORT NUMBER
7. AUTHOR(s) J. C. Hsia, J. H. Jacob, J. A. Mangano and M. Rokni		8. CONTRACT OR GRANT NUMBER(s) N00014-76-C-1032
9. PERFORMING ORGANIZATION NAME AND ADDRESS Avco Everett Research Laboratory, Inc. 2385 Revere Beach Parkway Everett, Massachusetts 02149		10. PROGRAM ELEMENT, PROJECT, TASK AREA & WORK UNIT NUMBERS
11. CONTROLLING OFFICE NAME AND ADDRESS Defense Advanced Research Projects Agency DARPA Order No. 1806		12. REPORT DATE
		13. NUMBER OF PAGES 107
14. MONITORING AGENCY NAME & ADDRESS(if different from Controlling Office) Office of Naval Research Department of the Navy Arlington, Virginia 22217		15. SECURITY CLASS. (of this report) Unclassified
		15a. DECLASSIFICATION/DOWNGRADING SCHEDULE

16. DISTRIBUTION STATEMENT (of this Report)

Approved for public release; distribution unlimited.

17. DISTRIBUTION STATEMENT (of the abstract entered in Block 20, if different from Report)

18. SUPPLEMENTARY NOTES

19. KEY WORDS (Continue on reverse side if necessary and identify by block number)

Rare Gas-Halide Lasers	E-Beam Controlled Discharge Excitation
High Power UV/Visible Lasers	Laser Kinetics
KrF Lasers	Laser Modeling
XeF Lasers	Magnetically Guided E-Beams
Electron Beam Excitation	

20. ABSTRACT (Continue on reverse side if necessary and identify by block number)

This interim report covers research directed towards efficient high power UV/visible lasers. The key issues being addressed are: (1) e-beam and e-beam controlled discharge excitation, (2) laser kinetics and modeling, (3) discharge stability and enhancement, (4) laser medium gain, adsorption and energy extraction and (5) intrinsic laser efficiency and scaling. Using e-beam controlled discharge pumping of a one meter KrF laser, 75 joules of laser output was obtained with 10% intrinsic efficiency at a specific energy of 10 J/liter. The use of an externally applied magnetic field to guide the e-beam is shown

DD FORM 1473 1 JAN 73   EDITION OF 1 NOV 65 IS OBSOLETE

20. Abstract

to effectively prevent e-beam steering by the discharge current and thus allow this excitation technique to be scaled to large laser apertures and very large single pulse energies. For efficient discharge pumping spatial e-beam energy deposition uniformity is shown to be important and methods of improving the deposition uniformity are proposed. Using pure e-beam excitation of XeF, a laser output of 36 joules was obtained with 2.6% intrinsic efficiency at a specific energy of 8 J/liter. Processes limiting XeF laser efficiency are identified and remedies proposed.

REPORT SUMMARY

A. PROGRAM SCOPE AND OBJECTIVE

This interim report covers the period 23 February 1977 to 22 August 1977. We report on research directed toward demonstrating efficiency, energy density and scalability of rare gas monohalide laser systems for development of high average power lasers applicable to DARPA missions.

During the previous reporting period, using pure e-beam excitation of KrF^*, we were able to obtain single pulse laser outputs of 102 J in an active laser volume of 8.5 ℓ (12 J/ℓ) with intrinsic laser efficiency of 9% (laser energy out/e-beam energy deposited in the laser medium). For this reporting period a portion of the effort had been directed toward e-beam controlled discharge pumping of KrF^*. Discharge pumping offers the potential for higher laser efficiency and reduced foil loading for high rep-rate operations.

A major portion of the effort for this period had been devoted to studying the XeF^* system. In order to carry out this research in an efficient manner, the effort has been three-pronged. First, various parts of the underlying physics are resolved on a small scale (20 cm) device. Second, the results of the small scale experiments are incorporated into comprehensive laser models which predict laser performance and scaling. Third, large scale e-beam excited XeF^* laser experiments are carried out on the one-meter device to check the predictive capability of the laser models.

1

B. ACCOMPLISHMENTS AND FINDINGS

The major results obtained in this reporting period are summarized as follows:

(1) Using e-beam controlled discharge excitation of KrF^*, a laser output energy of 75 J was obtained in an active volume of 7.5 ℓ (10 J/ℓ) at an intrinsic laser efficiency of 10%. The discharge enhancement ratio (discharge energy into the medium/e-beam energy absorbed in the medium) was 2.

(2) The use of an externally applied dc magnetic field to guide the e-beam is shown to remove the limit on aperture scaling of e-beam controlled discharge excited KrF^* lasers imposed by e-beam pinching due to the magnetic field associated with the discharge current.

(3) The discharge enhancement ratio (and consequently the efficiency) was shown to be severely limited by spatial and temporal e-beam nonuniformities.

(4) Kr_2F^* formation in KrF^* laser mixtures is shown to occur predominantly from reactions involving KrF^* as a precursor and consequently this channel of energy lost is saturable with KrF^* laser cavity flux.

(5) Important XeF^* formation and quenching rates have been measured.

(6) An XeF^* formation chain in Ne rich mixtures is proposed and shown to be consistent with all the experimental observations.

(7) XeF^* formation is shown to proceed with unit branching in e-beam excited Ar and Ne rich mixtures.

(8) Using pure e-beam excitation, an XeF^* laser output of 36 J
was obtained in ac active volume of 4.5 ℓ (8 J/ℓ) at an intrinsic
efficiency of 2.6%.

(9) The laser efficiency is shown to be limited by the slow vibra-
tional mixing in the upper level manifold and bottlenecking in
the lower level.

(10) Methods of improving XeF^* laser efficiency are proposed.

Plans for Next Period

For the next 6-month period a heated cell capable of operation up
to 250°C will be assembled and fitted to the one-meter device. Experi-
ments will then be performed with e-beam excitation of XeF^* at elevated
temperatures, to demonstrate improved extraction by increased rate of
lower level deactivation. With the same cell we will also look at efficiency
and energy scaling of e-beam and e-beam controlled discharge pumped
$HgCl^*$ lasers.

3

TABLE OF CONTENTS

LIST OF ILLUSTRATIONS

8

I. INTRODUCTION

The objective of the present program is to determine whether the rare gas-monohalide laser systems can be used to make efficient, high power lasers applicable to DARPA missions. During the previous reporting period we have demonstrated 12 J/ℓ with a 9% intrinsic laser efficiency from KrF* using pure e-beam pumping. These results agree well with a comprehensive laser model developed to reliably predict the performance of large scale KrF* lasers. We showed that e-beam pumped KrF* lasers can be scaled efficiently to very high single pulse energies.

In this reporting period a portion of the research effort had been devoted to studying the performance and scaling of e-beam controlled discharge pumping of KrF* lasers. Discharge pumping is interesting for two reasons: (1) it offers the possibility of higher laser efficiency because the upper laser level can be pumped through neutral metastable channels and (2) foil heating is much less severe because only a small portion of the pump power needs to be applied through a foil. Theoretical and small scale experimental studies carried out at AERL have shown that under suitable conditions stable discharges can be maintained in rare gas-halide laser mixtures. The studies showed that under carefully controlled discharge conditions, KrF* laser efficiencies of 15% at a discharge enhancement ratio of 4 (discharge energy into the laser medium/e-beam energy absorbed) should be possible.

A major portion of the effort had also been directed towards demonstrating efficiency and energy scaling of the XeF* system. XeF* is

11

I. INTRODUCTION

The objective of the present program is to determine whether the rare gas-monohalide laser systems can be used to make efficient, high power lasers applicable to DARPA missions.   During the previous reporting period we have demonstrated 12 J/ℓ with a 9% intrinsic laser efficiency from KrF* using pure e-beam pumping.   These results agree well with a comprehensive laser model developed to reliably predict the performance of large scale KrF* lasers.   We showed that e-beam pumped KrF* lasers can be scaled efficiently to very high single pulse energies.

In this reporting period a portion of the research effort had been devoted to studying the performance and scaling of e-beam controlled discharge pumping of KrF* lasers.   Discharge pumping is interesting for two reasons: (1) it offers the possibility of higher laser efficiency because the upper laser level can be pumped through neutral metastable channels and (2) foil heating is much less severe because only a small portion of the pump power needs to be applied through a foil.   Theoretical and small scale experimental studies carried out at AERL have shown that under suitable conditions stable discharges can be maintained in rare gas-halide laser mixtures.   The studies showed that under carefully controlled discharge conditions, KrF* laser efficiencies of 15% at a discharge enhancement ratio of 4 (discharge energy into the laser medium/e-beam energy absorbed) should be possible.

A major portion of the effort had also been directed towards demonstrating efficiency and energy scaling of the XeF* system.   XeF* is

11

attractive because at 350 nm the laser output lies in a wavelength region where atmospheric scattering and absorption is low. To carry out this study expeditioulsy a small scale (20 cm) device was used to measure various cross sections, quenching rate constants and to study the formation kinetics in various mixtures and pressures. The results of these experiments are then used to develop a comprehensive laser model which accurately predicts the performance and scaling of large scale XeF^* lasers. The predictive capability of the model is then checked with laser experiments on the one-meter device.

During this reporting period some key issues were raised concerning the formation kinetics in KrF^* lasers. Specifically, the question arose as to the formation mechanism for Kr_2F^*. It has been our contention that Kr_2F^* is formed mainly through reactions with KrF^* and as such the energy lost to Kr_2F^* formation is saturable with laser cavity flux. However, the possibility of Kr_2F^* formation via channels which intercepted the formation of KrF^* was raised. Therefore, a small portion of our effort in this period was devoted to settling this.

In this report the results of KrF^* and Kr_2F^* formation studies will first be presented. Then the current status of e-beam controlled discharge pumped KrF^* laser studies will be reported. Finally, results of e-beam pumped XeF^* laser studies will be described and methods of improving laser efficiency will be proposed.

12

II. KrF^* AND Kr_2F^* SIDELIGHT EXPERIMENTS

In the previous semi-annual report[1] we reported the observation of strong wide-band fluorescence from typical e-beam excited KrF^* laser mixtures centered about 415 nm. We attributed this fluorescence to the $^2B_2 \rightarrow A_1$ transition in the excited triatomic Kr_2F^*. We have further shown that in typical KrF^* laser mixtures, Kr_2F^* is formed predominantly through the reactions:

$$KrF^* + Kr + M \rightarrow Kr_2F^* + M \qquad (1)$$

and

$$KrF^* + Ar + M \rightarrow ArKrF^* + M \qquad (2)$$

followed by

$$ArKrF^* + Kr \rightarrow Kr_2F^* + Ar$$
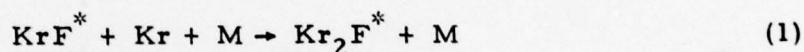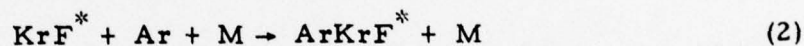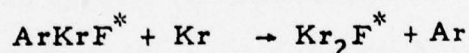
We pointed out that since KrF^* is the precursor to Kr_2F^* formation, the energy loss due to Kr_2F^* formation can be made small with a suitably high KrF^* laser cavity flux; that is, the loss is saturable.

Another possibility is that Kr_2F^* is formed predominanatly through reactions which intercepted the formation of KrF^*, e.g.,

$$Kr_2^+ + F^- + M \rightarrow Kr_2F^* + M \qquad (3)$$

or

$$Kr_2^* + F_2 \rightarrow Kr_2F^* + F \qquad (4)$$
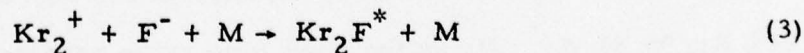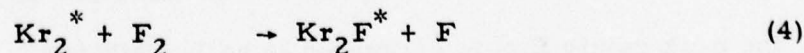
If this is the case then the energy lost to Kr_2F^* formation cannot be reduced by KrF^* laser cavity flux, and the ultimate attainable KrF^* laser efficiency will thus be seriously limited.

(1) Hsia, J.C., Jacob, J.H., Mangano, J.A. and Rokni, M., "One Meter KrF Laser System", Semi-Annual Report, 23 August 1976 to 22 February 1977.

13

To confirm that this is not the case, a series of laser sidelight measurements were performed. A schematic diagram of the experimental apparatus is shown in Figure 1. KrF^* (248 nm) and Kr_2F^* (410 nm) fluorescence perpendicular to the laser optical axis (sidelight) were monitored using photodiodes and narrow band filters. Measurements were taken with and without an optical resonator under otherwise identical conditions. Comparison of KrF^* sidelight intensities will then show the effect of gain saturation. The ratio of the sidelight intensities at 248 nm with and without a laser flux should be given by

$$\frac{I_{248} (\phi = \phi_{cav})}{I_{248} (\phi = 0)} = \frac{1}{1 + \phi_{cav}/\phi_{sat}} \tag{5}$$

where ϕ_{sat} is the saturation flux defined previously.[1]

If Kr_2F^* is formed predominantly through the collisional quenching of KrF^*, then one would expect to see a corresponding variation in Kr_2F^* sidelight as the cavity flux is varied. However, if the formation of Kr_2F^* occurs predominantly through reactions that compete with the formation of KrF^*, then no such variation would be expected.

Figure 2 shows oscillograms obtained by two successive shots with and without an optical resonator cavity, in 1.5 atm mixtures of 0.2% F_2/ 4% Kr/95.8% Ar. Using the quenching rates reported previously,[1] ϕ_{sat} is calculated to be 1.14 MW/cm^2. For the laser shot shown in Figure 2, the peak cavity flux is estimated to be 1.1 MW/cm^2. From the oscillograms, the ratio of KrF^* fluorescence at the peak of the pulse is

$$\frac{I_{248} (\phi = 1.1 \text{ MW/cm}^2)}{I_{248} (\phi = 0)} \approx 0.52$$

14
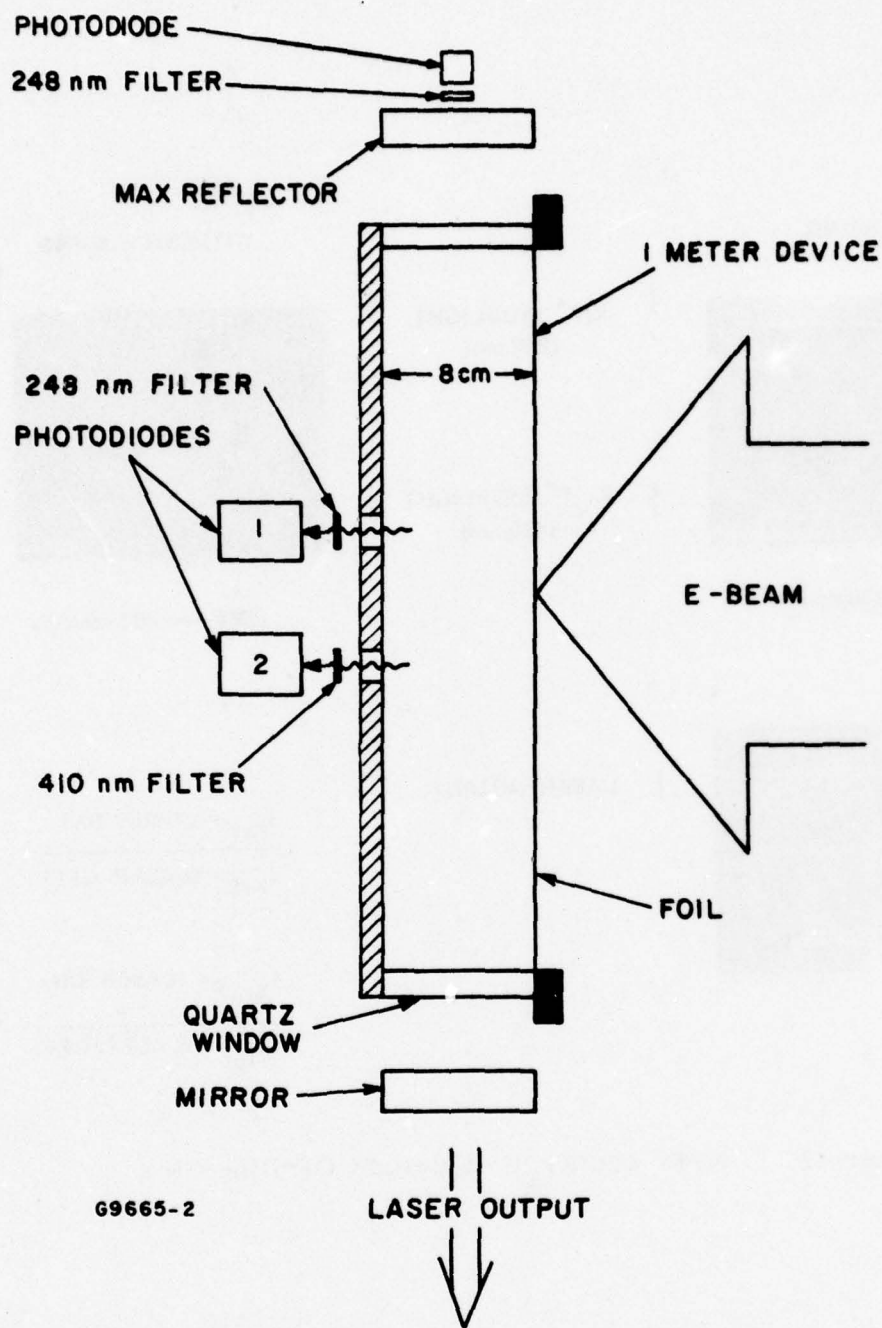
Figure 1 KrF^* and Kr_2F^* Sidelight Measurement Apparatus

WITH LASING   **WITHOUT LASING**

↓ KrF* SIDELIGHT ↓
(248 nm)

↑ Kr₂F* SIDELIGHT ↑
(410 nm)

→ TIME 200 ns/div   TIME → 200 nsec/div

↓ LASER OUTPUT

$$\frac{I_{KrF^*} \text{ (LASER ON)}}{I_{KrF^*} \text{ (LASER OFF)}} = .52$$

H3725

$$\frac{I_{Kr_2F^*} \text{ (LASER ON)}}{I_{Kr_2F^*} \text{ (LASER OFF)}} = .5$$
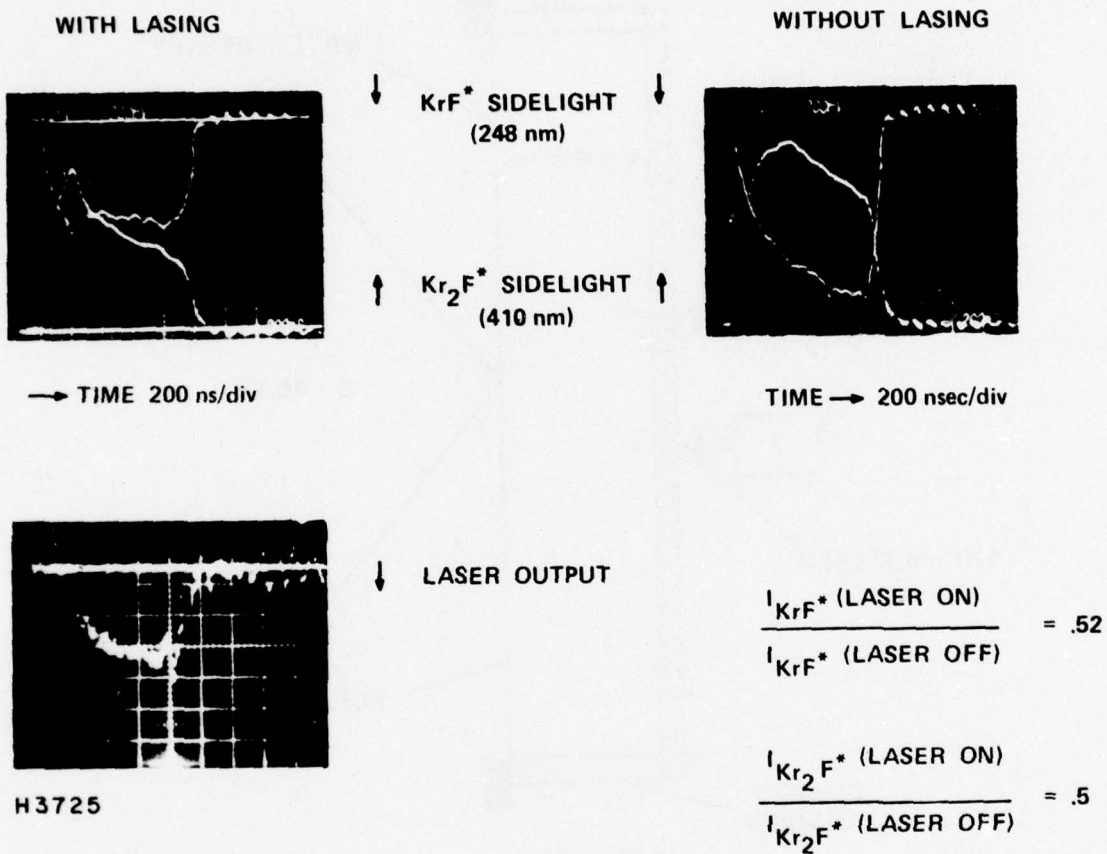
Figure 2   KrF* and Kr₂F* Sidelight Oscillograms

16

which agrees well with Eq. (5), and confirms the validity of our quenching rate measurements.

Furthermore, at the same time the Kr_2F^* fluorescence showed a corresponding decrease. In fact, the ratio of Kr_2F^* fluorescence measured with KrF^* laser cavity flux to that measured without is the same as the ratio of the corresponding KrF^* fluorescence. This indicates that essentially all of the Kr_2F^* formation occurred through reactions involving KrF^* as a precursor. The droop in the Kr_2F^* fluorescence towards the end of the pulse was probably due to (probably by electrons) quenching of Kr_2F^*.

The important conclusion drawn from these experiments is that the loss process which led to Kr_2F^* formation is a saturable loss and can be made small with a suitably high laser cavity flux.

III. E-BEAM CONTROLLED DISCHARGE PUMPING OF KrF* LASER

In e-beam controlled discharge pumping, a discharge voltage is applied across the laser mixture which is ionized by an e-beam. The secondary electrons are heated by the applied field and they produce the excited states which then lead to upper laser state formation. Potential advantages over pure e-beam pumping are higher efficiency and lower foil heating. The key technical issues that must be resolved are discharge energy channeling, enhancement and stability. In this section these issues are briefly discussed. The results of kinetic model calculations and small scale discharge experiments are summarized. Finally, the results of discharge pumped 1 m KrF* laser experiments are presented.

A. REVIEW OF KEY TECHNICAL ISSUES AND MODELING RESULTS

In discharge pumping of KrF* the formation of the upper laser state proceeds predominantly via the rare gas metastable channel. The formation kinetics are summarized in Figure 3 for mixtures containing $Ar/Kr/F_2$. The secondary electrons gain energy from the applied e-field and excite argon and krypton metastables. The krypton metastables then form KrF* with unit branching[2] via the harpoon reaction with F_2 ($Kr^* + F_2 \rightarrow KrF^* + F$). Similarly Ar^* forms ArF* with a branching ratio of 0.6.[2] The ArF* can either radiate or the Ar can be replaced by a Kr to form KrF*. Because of the lower excitation energy to form Kr^* (10 eV for Kr^* compared to 11.5 eV for Ar^*) and higher branching to form KrF*, the formation efficiency will be larger if most of the discharge energy can be channeled into Kr^*. The fraction of the energy deposited in Kr^* depends on the percentage of Kr in the

---

(2) Chen, C. H., Judish, J. P., and Payne, M. G., "Energy Transfer Processes in Ar-Xe and Ar-F_2 Mixtures" (Unpublished).

19
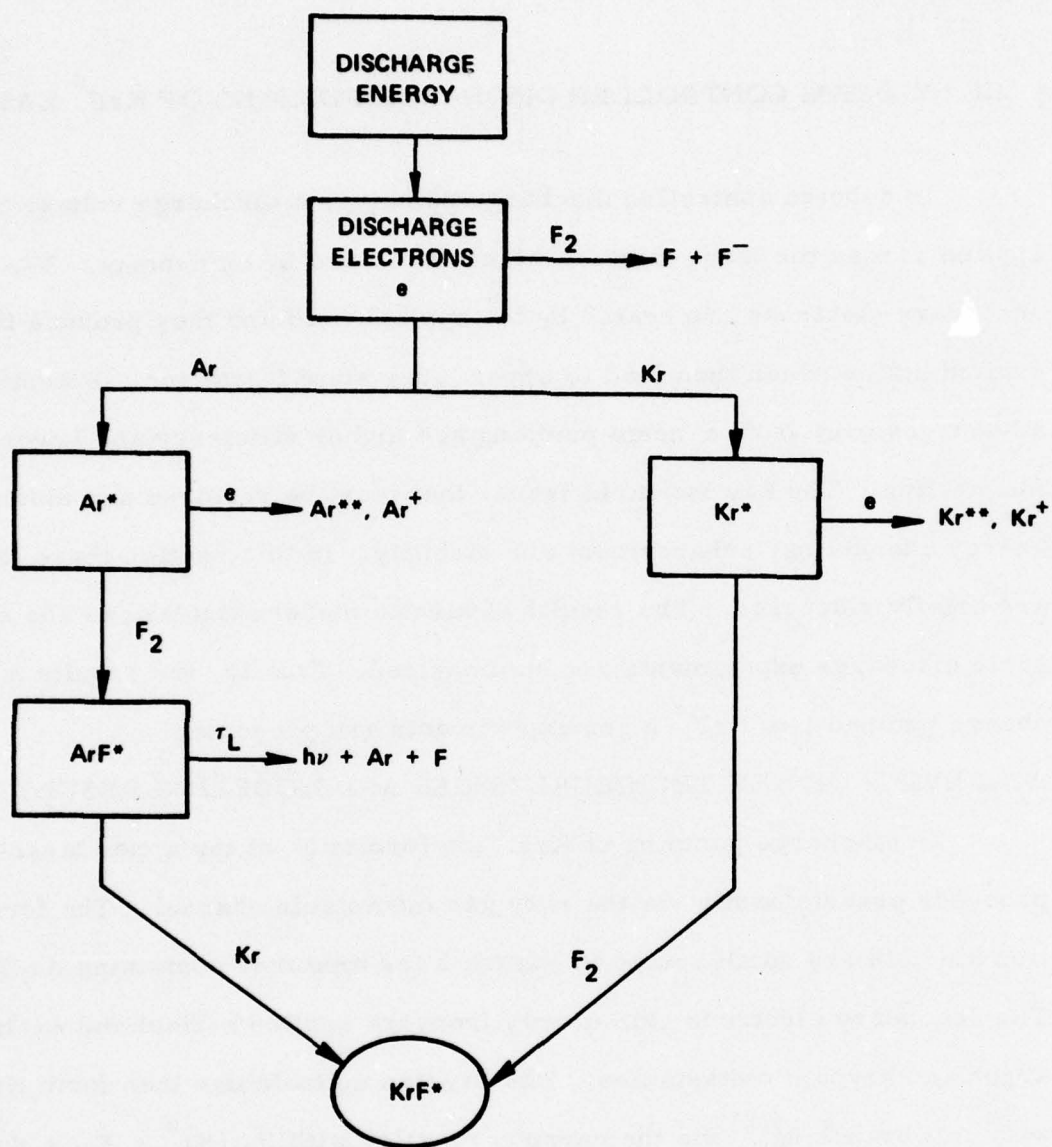
Figure 3   KrF* Formation Kinetics in Discharge Excited
Ar/Kr/F₂ Mixtures

20

mixture and the applied electric field. However, since Kr quenches KrF^* much more rapidly than Ar, the Kr concentration must be kept small for efficient extraction.

The fraction of discharge energy channeled to the production of rare gas metastables depends also on the fractional metastable population. For fractional metastable population (metastable density/ground state density) $\gtrsim 3 \times 10^{-5}$, a significant fraction of the discharge energy will go into exciting the metastables to higher lying levels and also into ionizing the metastables. These effects are shown in Figures 4 and 5. These are results of calculations using a computer code which solves the Boltzmann electron transport equation. The code takes the various collision cross section data and the electric field and calculates the self-consistent electron energy distribution and the energy partitioning amongst the various excited states. For these calculations we have approximated the krypton metastable cross sections with that of ground state rubidium. Similarly for Ar^* we used cross sections for potassium. These approximations are justified physically by the atomic similarity between rare gas metastables and the alkalis.[3] Some of the electron impact cross sections used in our model are shown in Figure 6.

Figure 4 shows the percentage of discharge energy that goes into the production of Ar^* and Kr^* as a function of fractional metastable density for various applied electric fields. Note the fraction of energy into metastable production falls dramatically for fractional metastable density $\gtrsim 3 \times 10^{-5}$. The reason is that the peak metastable excitation cross section ($5_s \rightarrow 5_p$) is 30 times higher than the peak value of the excitation cross section from the ground state. Also, since the excitation threshold for $5_s \rightarrow 5_p$

(3) Brau, C. A., and Ewing, J. J., J. Chem. Phys., 63, 4640 (1975).

21
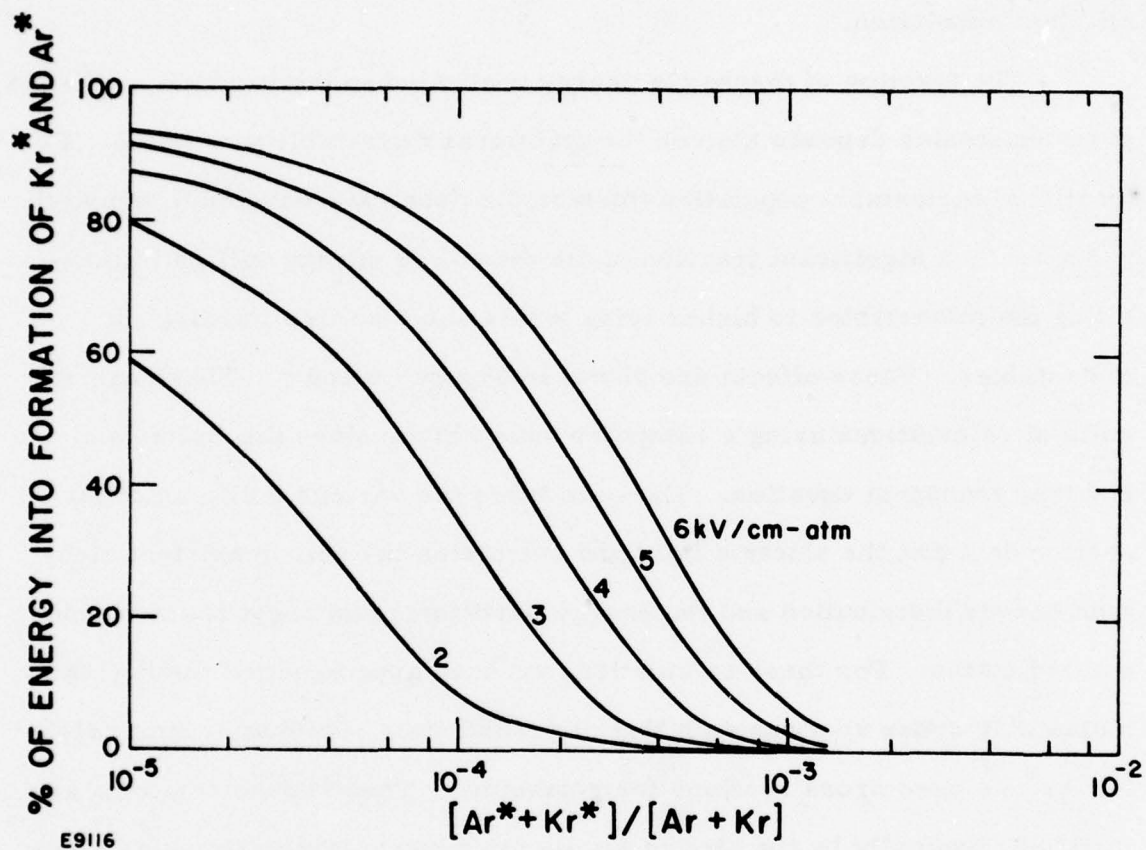
Figure 4   Percentage at Discharge Energy into Ar* and Kr* as a Function of Fractional Metastable Density for Ar/Kr Mixtures

22
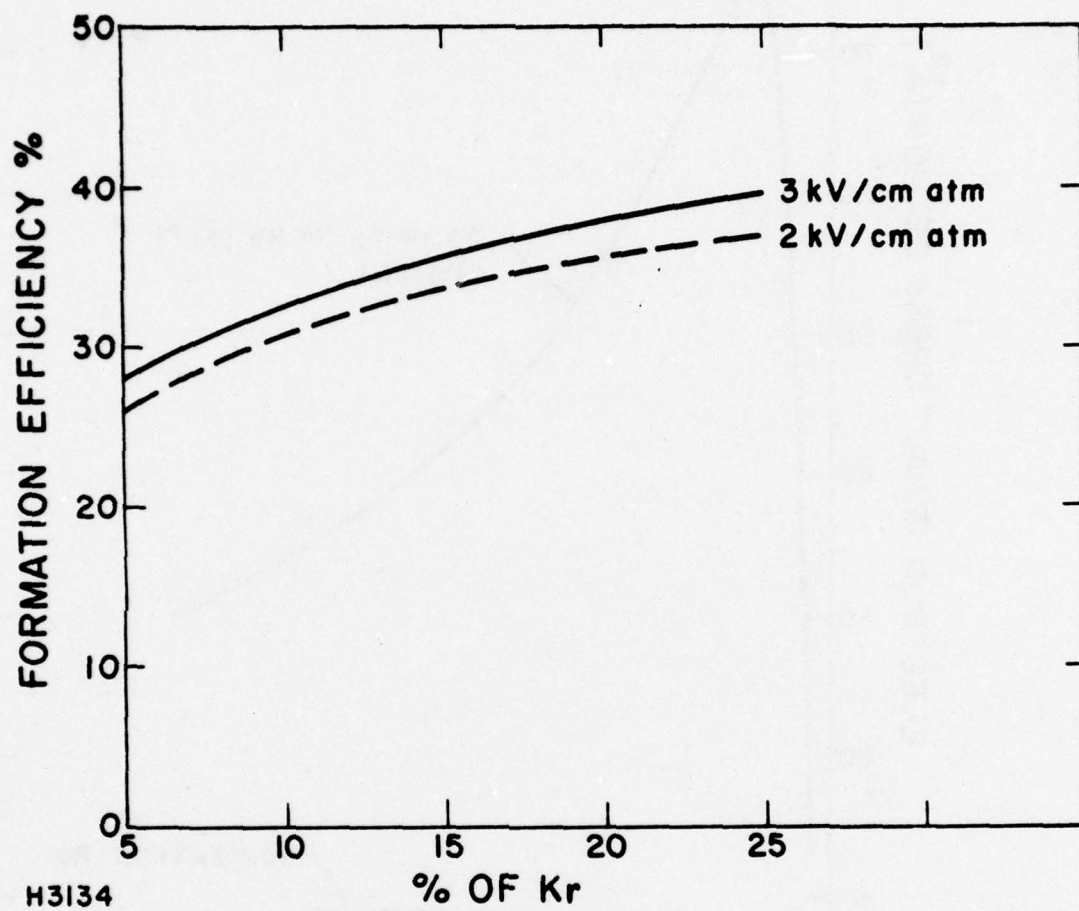
Figure 5   Formation Efficiency of KrF* as a Function of Fractional Kr Density

23
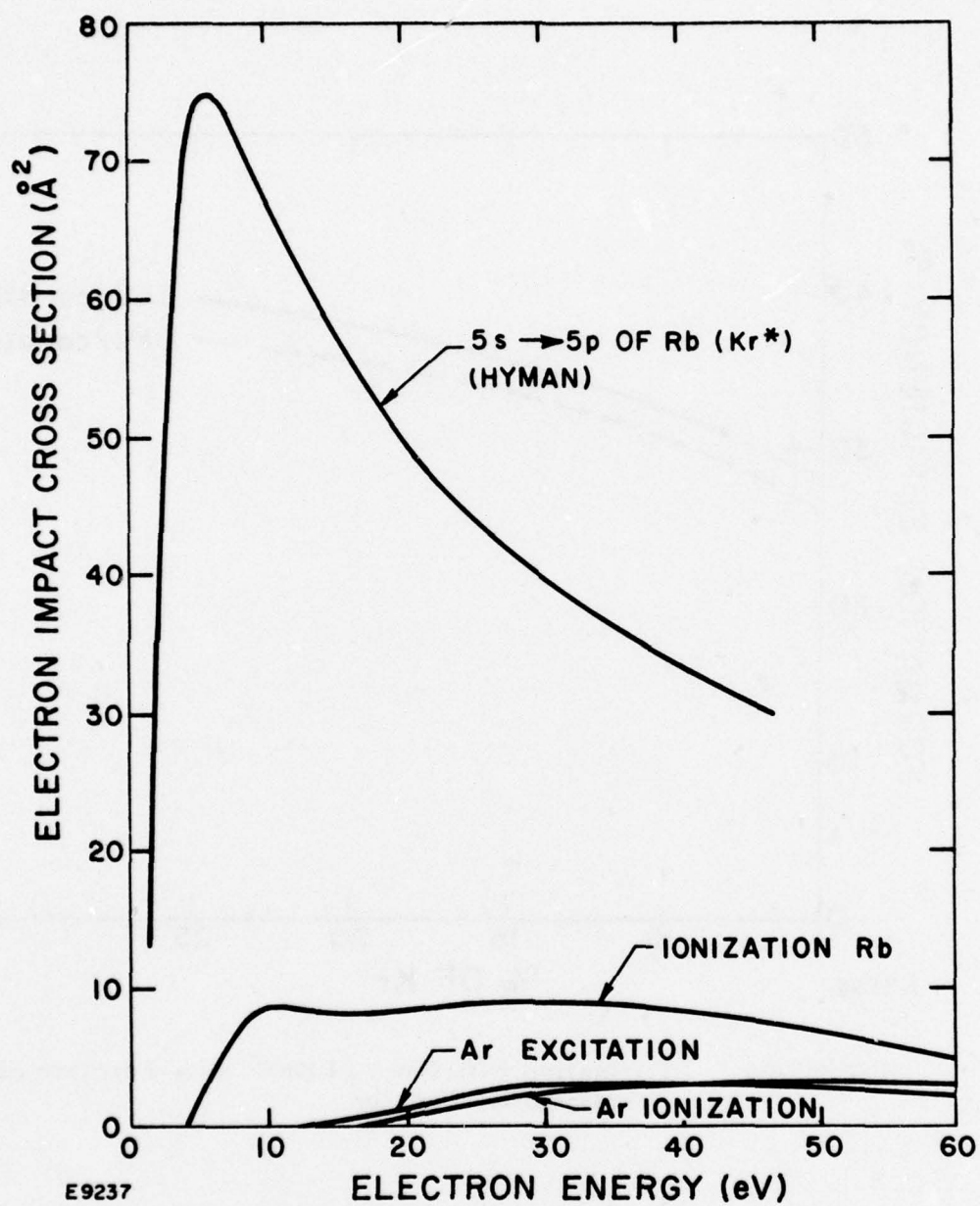
Figure 6　　Electron Impact Cross Section for Rb(Kr*) and Ar as a Function of Electron Energy

transition is $\lesssim$ 2 eV, and since it peaks at $\approx$ 6 eV, most of the electrons can excite the transition resulting in a cooling of the electrons, whereas only the high energy tail of the electron energy distribution can produce metastables from the ground state. Therefore, for high metastable densities discharge energy is channeled preferentially into the excitation of the metastables. The decrease in metastable formation can be made up by increasing the electric field. However, the ionization rate (Figure 7) rapidly becomes so large that it precludes discharge stabilization by electron attachment by F_2. From this it is clear that for efficient energy channeling and discharge stability, the fractional metastable density must be kept small.

For small metastable densities, the KrF^* production efficiency (energy into KrF^*/total discharge energy) is calculated versus Kr concentration in Figure 5, for electric fields of 2 and 3 kV/cm-atm. Note that efficiencies as high as 30 to 35% (compared with 22% for pure e-beam pumping) is possible. To achieve this high efficiency the fractional metastable density must be $\lesssim 3 \times 10^{-5}$. However, for efficient laser energy extraction the small signal gain must be kept high. This means that one must run at high metastable densities and consequently there exists only a small range of fractional metastable densities around 3×10^{-5} where both high formation and extraction efficiencies can be maintained. To see this, one can use the quenching rates for KrF^* reported in the previous period and taking a rate constant of $K = 7 \times 10^{-10}$ cm^3/sec for the reactions

$$Kr^* + F_2 \rightarrow KrF^* + F$$

$$Ar^* + F_2 \rightarrow ArF^* + F$$

25
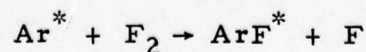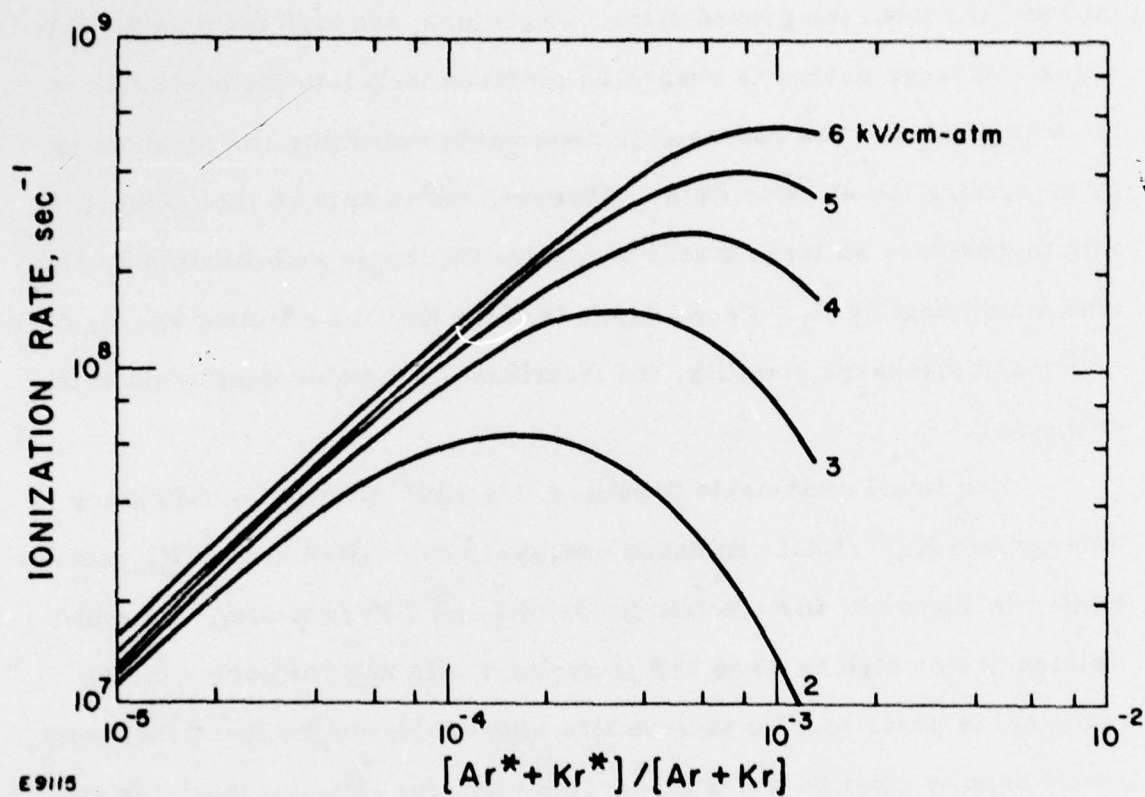
Figure 7   Ionization Rate as a Function of Fraction at Metastable
            Density

26

one can express the small signal gain g_o as a function of metastable density.
Then if one assumes a constant laser medium absorption, (not strictly true,
in general absorption depend on excitation, but constant absorption is assumed
here for illustration) one can plot the extraction efficiency as a function of
metastable density by using the extraction model presented in the previous
report.[1] Results of such a calculation are shown in Figure 8. Here we
have assumed an electric field of 3 kV/cm-atm, and we have taken an ab-
sorption coefficient α of 4×10^{-3} cm^{-1}. The intrinsic laser efficiency is
the product of the formation and the extraction efficiencies. This is also
shown in Figure 8.

For efficient laser operation suitable conditions must be maintained
over the entire pulse. Therefore the discharge must be stable. The dis-
charge stability of these mixtures is strongly affected by the rare gas ex-
cited states. Under typical operating conditions with 3×10^{-5} fractional
metastable density, electron impact ionization of the metastables is typi-
cally 4 orders of magnitude higher than direct ionization from the ground
state. Therefore, in the stability analysis we can assume all the ionization
produced by the secondaries arises from a two step (metastable) ionization
process.

The equation describing the production and loss of discharge electrons
n_e is given by

$$\frac{dn_e}{dt} = S + (\nu_i - \beta) \, n_e \tag{6}$$

where S is the rate of e-beam ionization. The production and loss of meta-
stables can be written

$$\frac{dM^*}{dt} = \langle \sigma \, v \rangle \, n_e \, M - \frac{M^*}{\tau_d} \tag{7}$$

27
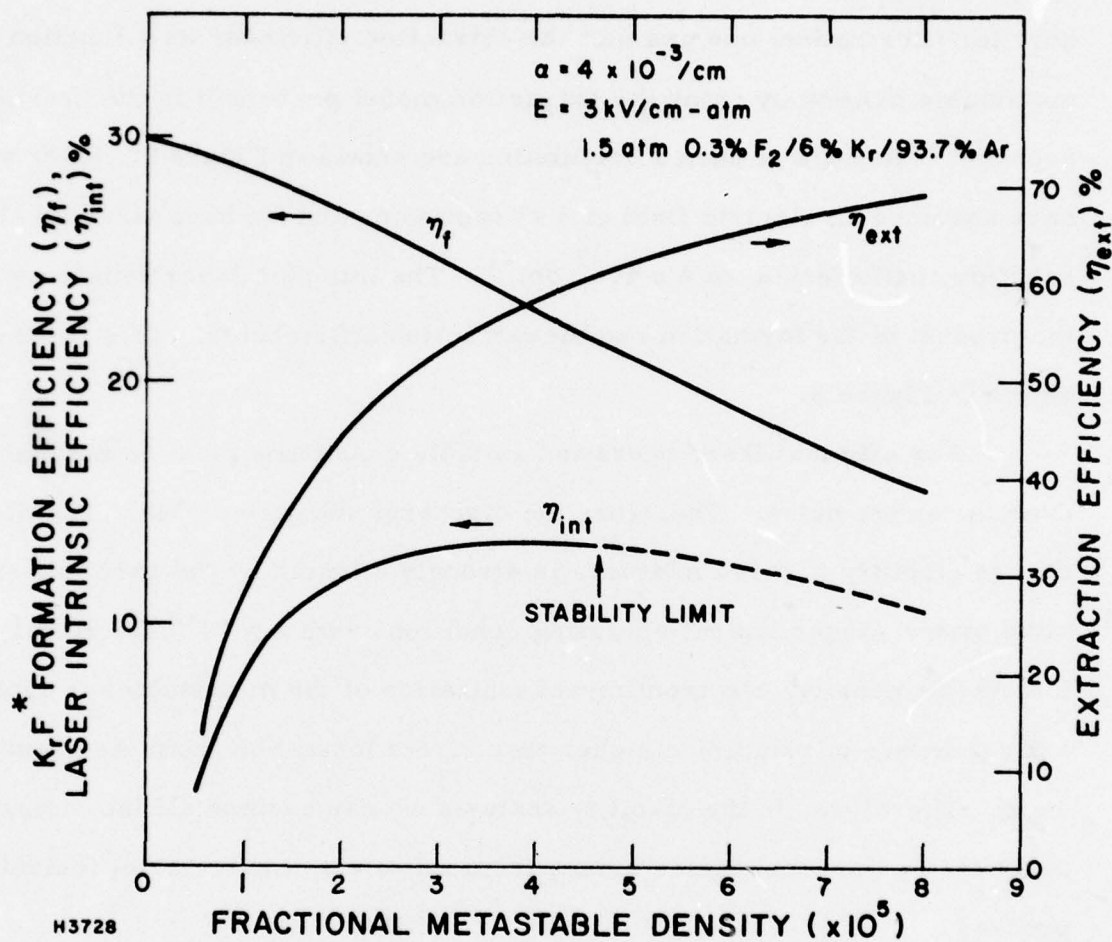
Figure 8   Formation and Extraction Efficiency as a Function of
            Fractional Metastable Density

where M is the ground state density, M^* is the metastable density, τ_D is the metastable lifetime and $\langle \sigma v \rangle$ is the electron impact metastable production rate. Since ionization is predominantly from the metastables we can write

$$\nu_i = \langle \sigma v \rangle_i \, M^* \tag{8}$$

Equations (6) and (7) are then a pair of coupled nonlinear differntial equations in n_e and ν_i. It can be shown by perturbation analysis[4] that this system of equations predict stable steady state solutions only if

$$\beta \geq 2 \, \nu_{i0} \tag{9}$$

where ν_{i0} is the equilibrium ionization rate.

We have numerically solved a system of nonlinear equations similar to Eqs. (6) and (7) for e-beam current of about 2 A/cm^2. In this analysis we have also included Penning ionization and ionization of the ground state atoms. Figure 9 shows the results of such an analysis. On the left-hand side we have the stable discharge condition, i.e., the attachment rate is slightly greater than the equilibrium ionization rate. Notice that the discharge current reaches a constant value asymptotically. Another important feature for the stable discharge case is that the metastable production efficiency η_M remains above 75%. If we keep everything constant but decrease the attachment rate by 20% we observe that the ionization rate increases and after about 70 ns becomes greater than the attachment rate. For this case the discharge current increases faster than exponentially in time and the metastable production efficiency falls steeply.

To fully utilize the advantages of discharge pumping one must also operate at large discharge enhancements. The discharge enhancement is

---

(4)   Daugherty, J. D., Mangano, J. A., and Jacob, J. H., Appl. Phys. Lett. **28**, 581 (1976).
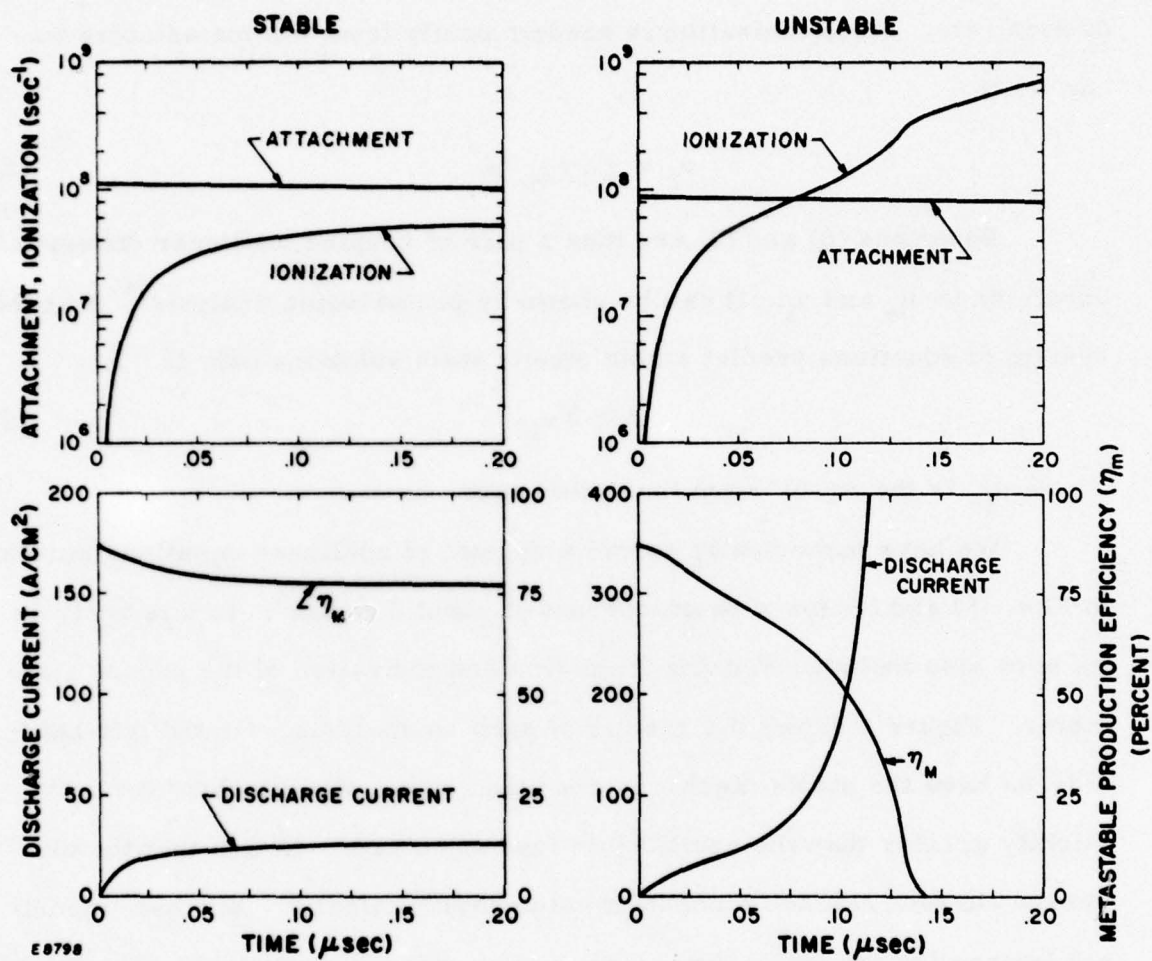
Figure 9   Results of Numerical Analysis of Discharge Characteristics

defined here as the ratio between power deposited in the laser mix by the discharge, P_d, to the power deposited by the e-beam, P_{eb}. This ratio is given by

$$\frac{P_d}{P_{eb}} = \frac{eV_D E}{(\beta - \nu_i) E_i} \tag{10}$$

where V_D is the electron drift velocity, E is the applied electric field, β is the electron attachment rate, ν_i is the secondary electron ionization frequency and E_i is the average energy required to produce an electron-ion pair by the e-beam.

At the limit of discharge stability the enhancement is given by

$$\frac{P_d}{P_{eb}} \leq \frac{eV_D E}{\nu_i E_i} = \frac{2V_D Ee}{\beta E_i} \tag{11}$$

For a given electric field, one can use the Boltzmann code to express the ionization rate ν_i as a function of metastable production efficiency. Then using Eq. (10) one can calculate the enhancement factor as a function of metastable production efficiency. A result of such a calculation is shown in Figure 10 where we have taken an electric field of 3 kV/cm-atm. The analysis shows that it is possible, under stable discharge conditions, to obtain an enhancement as high as 4 with metastable production efficiency $\approx 70\%$.

B. SMALL SCALE EXPERIMENTS

To compare in detail our experimental results to theoretical predictions we have developed a kinetics code which uses the rates predicted by the Boltzmann code and follows the temporal evolution of the secondary electrons, positive and negative ions, Ar^*, Kr^* and KrF^*. We couple our kinetics code to a simultaneous set of differential equations that

31
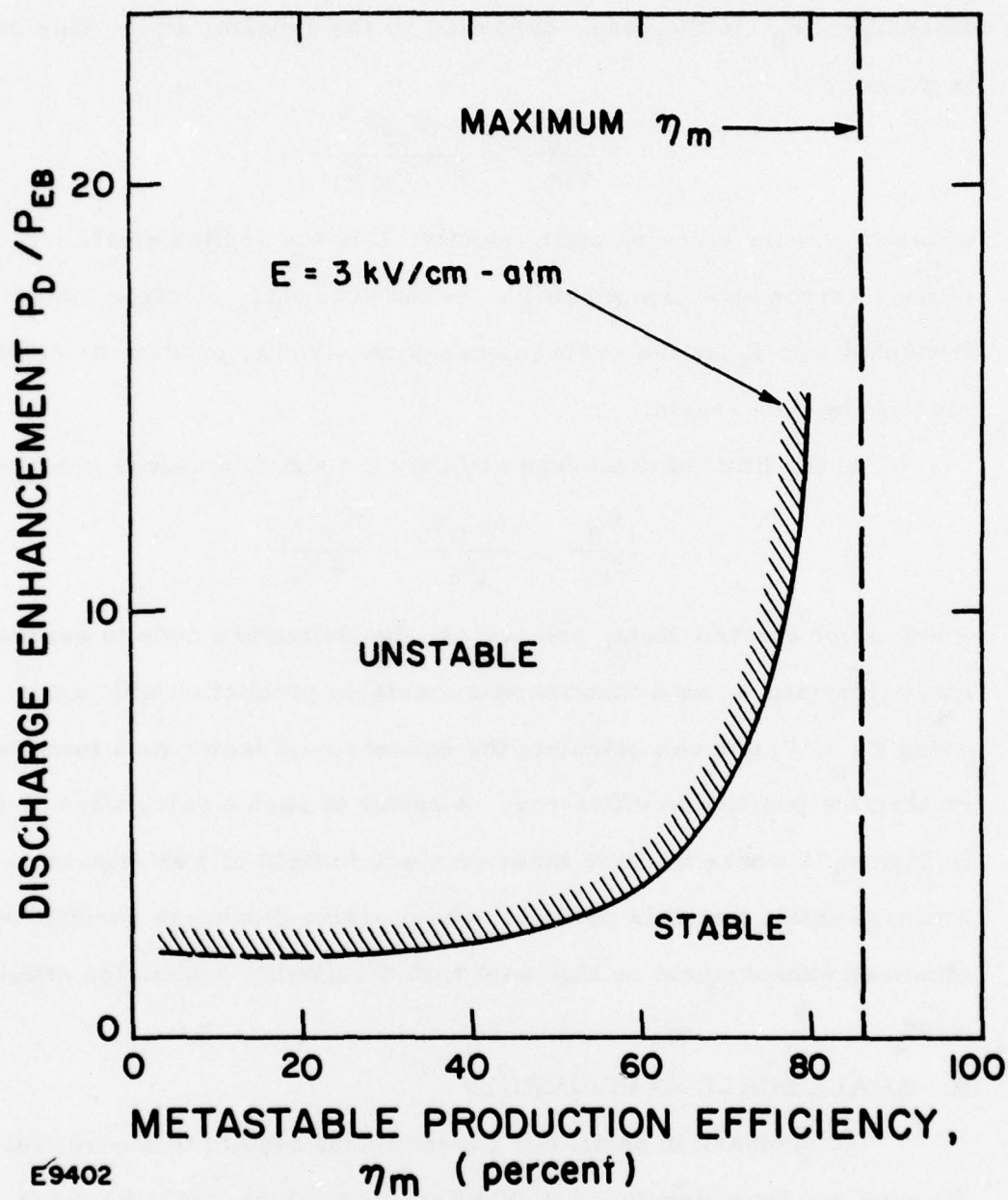
Figure 10   Plot of Discharge Enhancement Ratio as a Function of
               Metastable Production Efficiency at Limit of Discharge
               Stability

describe the external electrical circuit. The outputs of this code include the temporal evolution of the discharge current and voltage and the KrF* fluorescence for a given preionization level, discharge capacitor charge voltage and gas mixture. The predictions of this discharge model have been compared with our small scale (20 cm) KrF laser discharge experiments. Figure 11 compares the experimental results with model predictions for a case where the cavity was filled with a 2 atm mix of 93.7% Ar/6% Kr/0.3% F_2, and a 0.3 μF capacitor charged to 10 kV was used to power the discharge. The third trace is the KrF* fluorescence. By the end of the pulse the enhancement in the fluorescence is 3. The metastables are being produced with a maximum efficiency of 1.4 times the efficiency of metastable production by a pure e-beam. Figure 12 shows the results when the capacitor is charged to 16 kV. In this case the discharge current continually increases until the discharge goes through the glow to arc transition which is marked by an abrupt decrease in KrF* fluorescence. We believe that the initial (slow) increase in the discharge current is caused by a volumetric discharge instability discussed previously. The efficiency for producing the metastables rises rapidly to 1.7 times the efficiency of producing metastables in a pure e-beam and then begins to fall despite the fact that the voltage is constant. The KrF* production efficiency decreases because the metastable density increases and the discharge pumping efficiency of Ar^* and Kr^* falls.

The agreement between the kinetic code predictions and the small scale experiments demonstrates that the important physical processes governing the operation of e-beam controlled discharge excitation of KrF* lasers are adequately described by the kinetic model. Scaling calculations

33

STABLE
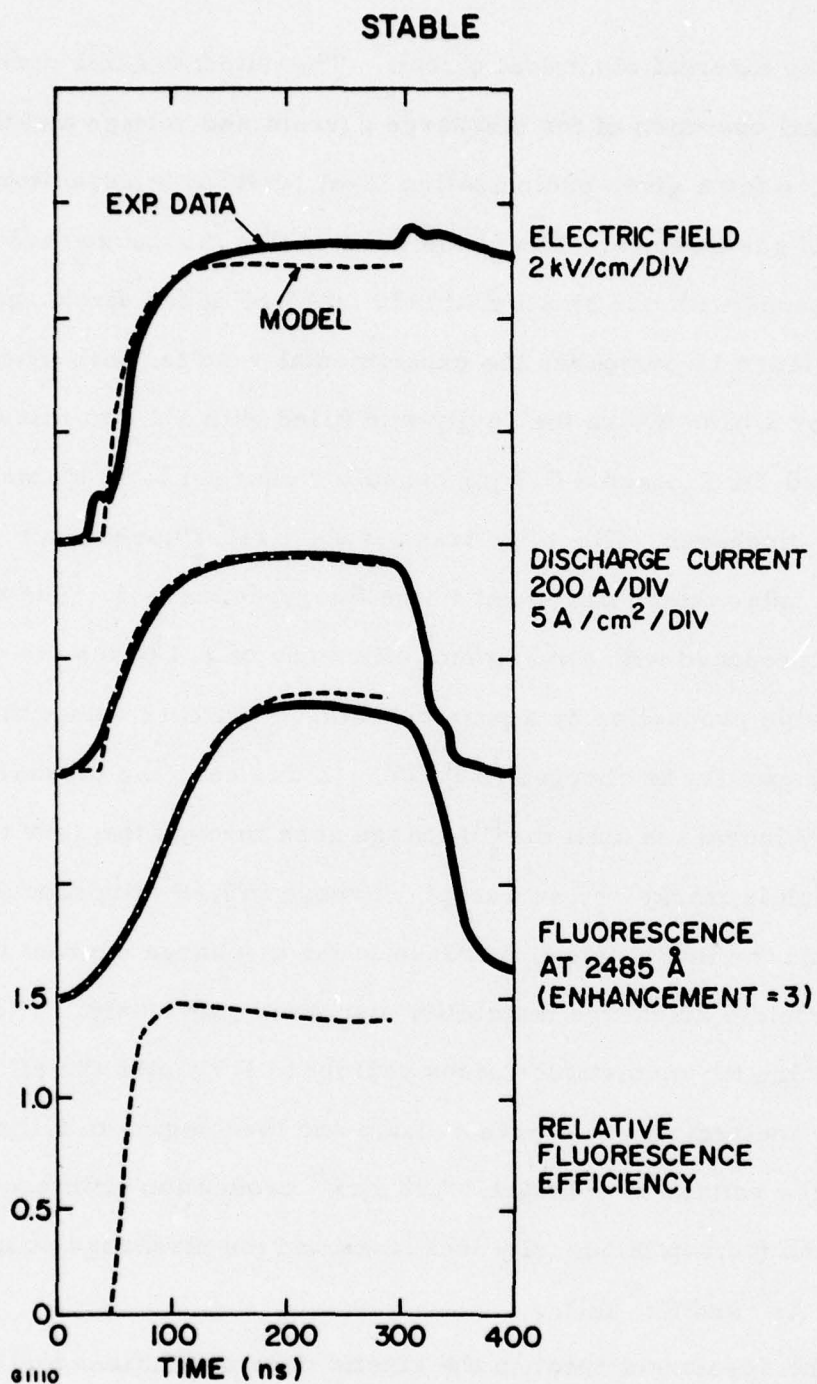
Figure 11   Measured and Predicted Fluorescence and Discharge
Characteristics When Discharge Capacitor is Charged
to 10 KV

34

UNSTABLE
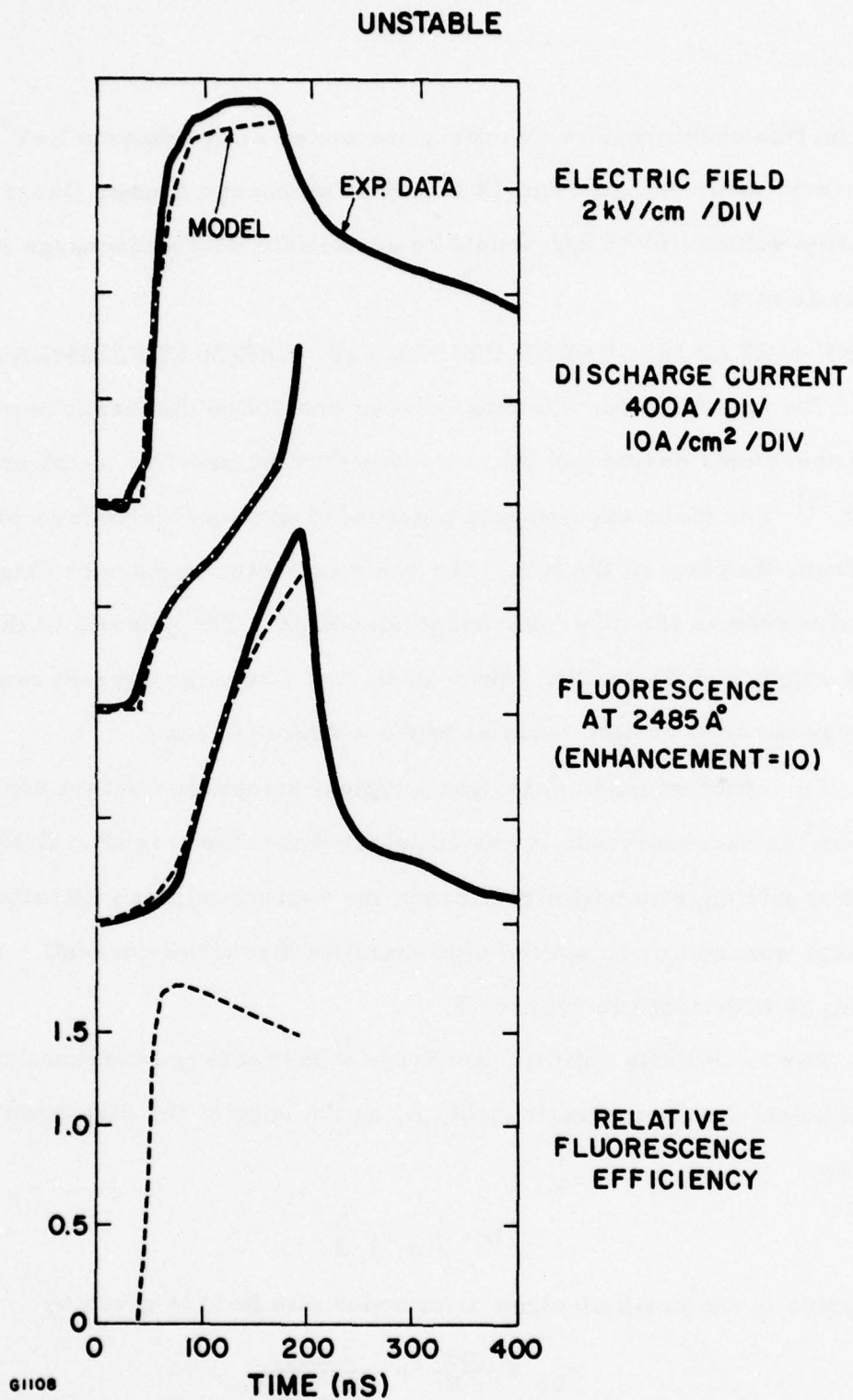
Figure 12   Measured and Predicted Fluorescence and Discharge
Characteristics when Discharge Capacitor is Charged
to 16 KV

based on this code predicts that for a one meter active volume KrF* device, an intrinsic laser efficiency of 12 to 13% at an energy density (laser energy out/active volume) of 15 J/ℓ should be achievable with a discharge enhancement ratio of 4.

C. ONE-METER DISCHARGE PUMPED KrF* LASER EXPERIMENTS

The apparatus for studying e-beam controlled discharge pumping on the one-meter device has been described in the previous semi-annual report.[1] For these experiments a grounded screen electrode is placed 2 cm from the plane of the foil. The beam collector is pulsed to high voltage and serves as the other discharge electrode. The polarity of the discharge supply can be readily reversed so that discharge current can either be driven parallel or anti-parallel to the e-beam current.

For efficient laser operation a typical discharge current density of 50 A/cm^2 is necessary and it was anticipated that the magnetic field generated by this current will either cause the e-beam to pinch (parallel discharge current) or to spread (anti-parallel discharge current). Beam pinching is illustrated in Figure 13.

For an initially uniform discharge with discharge current density J_d and height h, the magnetic field, B, at the edge of the discharge is given by

$$B = \mu_o J_d \frac{h}{2}$$

The radius of the beam electron orbit under this field is given by

$$r_{be} = \frac{mu}{eB} = \frac{2\,mu}{e\mu_o J_d h} \ ,$$

where mu is given by

$$mu = (2\,m_o E)^{1/2} (1 + \frac{E}{2\,m_o C^2})^{1/2}$$

36
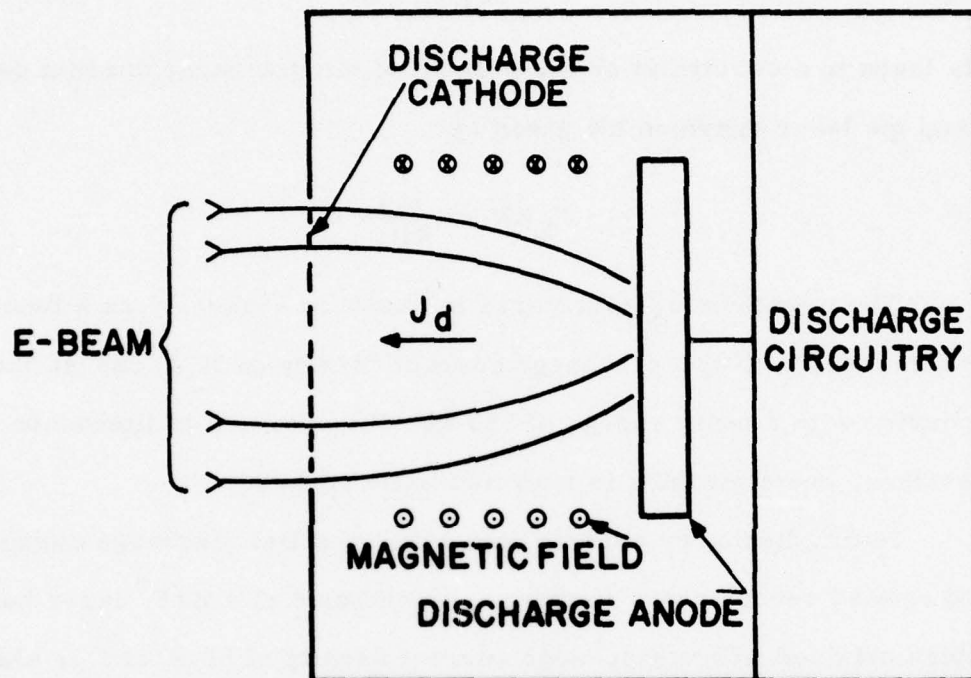
G3080

Figure 13   E- Beam Pinching by the Magnetic Field Generated by the
Discharge Current

m_o is the electron rest mass, and E is the beam energy. The width, W, of the discharge is limited to $\approx r_{be}/2$, that is

$$W < \frac{mu}{e\,\mu_o\,J_d\,h}$$

This leads to a constraint on the product of the discharge current density J_d and the laser aperture hW given by

$$J_d\,hW < \frac{mu}{e\,\mu_o} \quad .$$

The maximum aperture area is shown in Figure 14 as a function of e-beam energy. For a discharge current density of 50 A/cm^2 in the present device with a beam energy of 250 kV, the aperture is limited to 30 cm^2. Therefore, beam pinching is expected to be severe.

Initial discharge experiments using parallel discharge current indeed showed severe beam pinching. An example of a KrF* laser burn pattern obtained with a discharge current density of 50 A/cm^2 is shown in Figure 15. The laser optical resonator consisted of two flat mirrors with high output coupling. With this configuration the laser output burn profile reflected the variation in energy deposition across the laser aperture. At the foil the e-beam was 10 cm high. As the beam propagated across the discharge region the beam was pinched by the magnetic field due predominately to the discharge current, so that the ionization by the e-beam was more intense at the center of the beam. The higher e-beam ionization at the center in turn led to increased discharge current at the beam center. Since the electric field E was essentially constant over the height of the discharge, more discharge energy was deposited into the center of the beam, resulting in a constricted burn pattern shown in Figure 15. Note that for

38
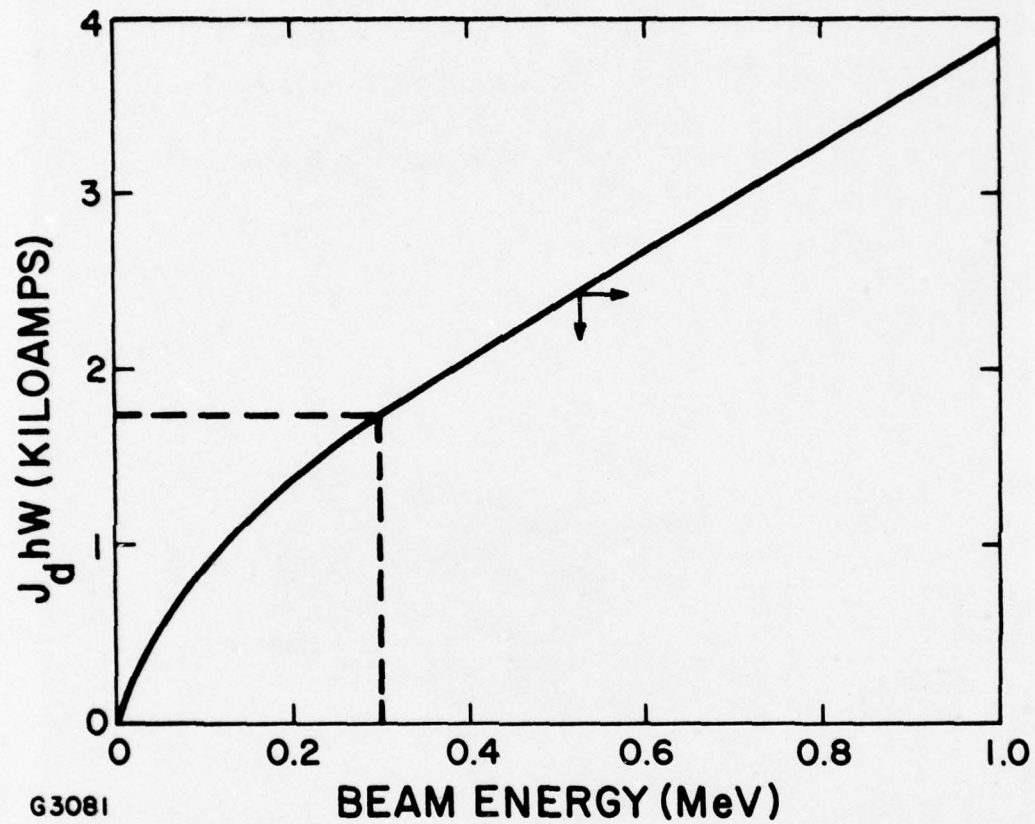
Figure 14   Maximum Aperture Area and Discharge Current Density
              Product as a Function of E-Beam Energy
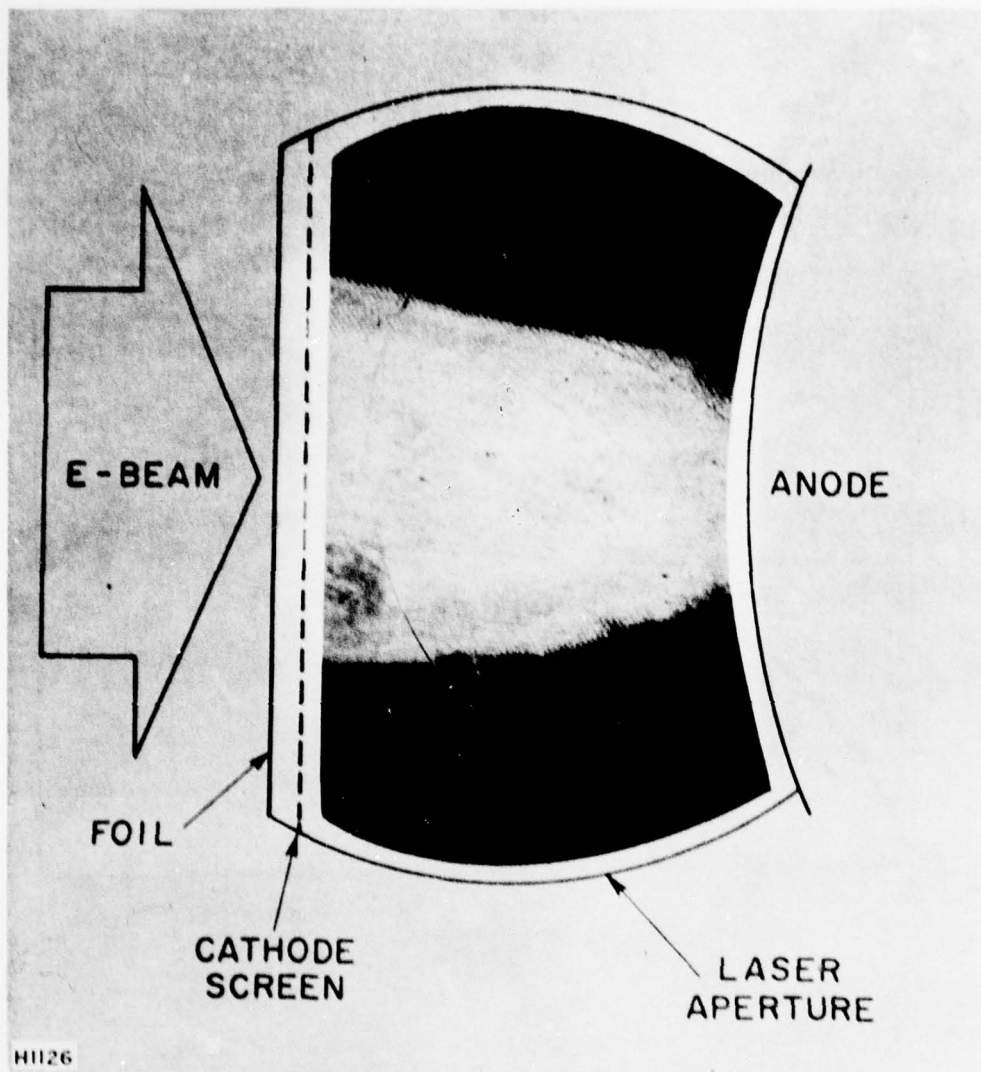
Figure 15   Laser Burn Pattern Showing E-Beam Pinching

interesting discharge enhancements, the discharge current J_D must be typically $> 10 J_{eb}$, therefore, the magnitude of the magnetic field generated by anti-parallel current operation will be comparable and the e-beam will diverge leading to large transverse deposition gradients and inefficient laser performance.

The application of an external magnetic field in the direction of the e-beam with intensity much larger than field produced by the discharge current eliminates beam pinching or spreading. In the present device, at 50 A/cm^2 discharge current, the magnetic field generated at the edge of the discharge is ≈ 300 G. When an external field of 800 G was applied, beam pinching was effectively eliminated and a typical burn pattern is shown in Figure 16. This result demonstrates that by using an external magnetic field the constraint on discharge cross sectional area shown in Figure 14 can be overcome and e-beam controlled discharge pumping can be scaled to very large single pulse energies.

The above also underscores the importance of uniform e-beam energy deposition in e-beam controlled discharge excitation. We have shown previously that, for optimum KrF^* formation and laser energy extraction, the level of excitation must be kept within a narrow range just below the limit of discharge stability. Equations (10) and (11) show that the highest discharge enhancements are also achieved close to the stability limit. Therefore if the e-beam energy deposition is not uniform over the discharge region, then when conditions are chosen for stability at regions of high e-beam deposition, the regions of low e-beam deposition will be insufficiently excited for efficient extraction and the overall laser efficiency will be lower than that achievable with uniform e-beam deposition. The average discharge enhancement will also be lower than that given by Eq. (11).

41
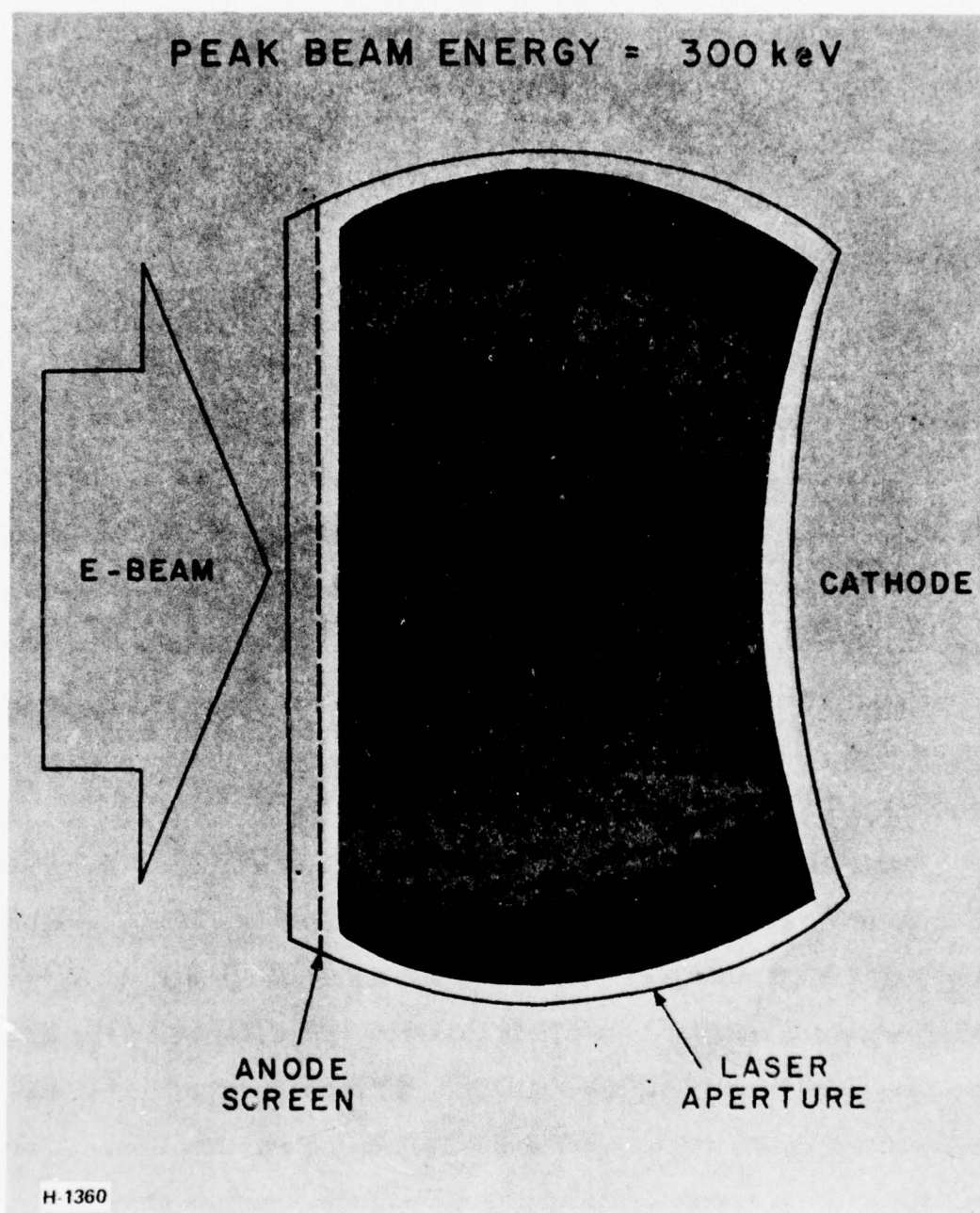
Figure 16   Laser Burn Pattern with an Externally Applied 800 Gauss
Magnetic Field

One can raise the average e-beam current so that the regions of low beam deposition can be effectively excited. However since stability must be maintained over the entire volume, the peak discharge enhancement will be lowered. This can be seen clearly if one rewrite Eq. (11) in a slightly different form. Since two step ionization implies that local ionization rate, ν_i is proportional to P_d, at the limit of stability we have

$$\frac{P_d}{P_{eb}} \leq \frac{e \, V_d \, E}{A \, P_d \, E_i} \tag{12}$$

where A is a constant. This implies that

$$\frac{P_d}{P_{eb}} \propto \frac{1}{P_{eb}^{1/2}} \tag{13}$$

or that when the e-beam intensity is raised the peak discharge enhancement is necessarily lowered.

In the one meter device, the application of an external magnetic field effectively eliminated large scale e-beam nonuniformities due to beam pinching by the discharge current. However, in spite of this, substantial e-beam nonuniformities still exist. The inhomogeneity is caused predominently by (1) stopping of the e-beam in the high pressure laser gas and (2) the localized beam intensity fluctuations believed to arise from the bipolar diode effect in the e-gun. These effects together with measured spatial beam variations are discussed in detail in the previous report. [1] Stopping of the beam gives rise to a factor of 1.6 variation in e-beam energy deposition in the direction of the beam current as one moves across the discharge region from the anode to the cathode. The fast localized beam fluctuations can give rise to transverse beam variations greater than a factor of 2.

43

In addition diode closure in the e-gun give rise to a continuously
rising beam current during a pulse so that the optimum beam current den-
sity for discharge excitation can only be maintained for a fraction of the
e-beam pulse. The percentage of e-beam variation during the pulse depends
on the e-gun anode-cathode spacing and e-gun voltage. Typically at 6 cm
anode-cathode spacing and 300 kV applied, the variation in 0.5 μs is of order
30%.

Compared with the one meter device, e-beam uniformity in the 20 cm
device is significantly better. The e-gun on the 20 cm experiment is driven
by a cable which, inspite of diode closure, yields a relatively constant e-beam
current during its 300 nsec pulse. The discharge anode-cathode spacing in
the 20 cm device is only 2 cm and typically at 1.5 atm, beam stopping and
scattering gives rise to only 30% beam deposition variation over the discharge
volume. Furthermore, since the pulse length in that device is limited to 300 nsec
and it takes ~300 nsec for the fast beam fluctuations to appear, the fast fluctua-
tions did not contribute significantly to e-beam nonuniformity. Therefore the
e-beam in the 20 cm approximated the uniform e-beam condition assumed in the
discharge kinetic model and all major predictions of the model agree well with
experimental measurements. However in the one meter device, with the
measured e-beam nonuniformities, close agreement with kinetics model pre-
diction can not be reasonably expected.

Nevertheless attempts were made to run the laser discharge at con-
ditions calculated to be optimum assuming an uniform e-beam. The code
calculations indicated that at an e-beam current of 2.5 A/cm^2, a discharge
enhancement ratio of 4 could be maintained at an applied field of 3 kV/cm-
atm in 1.5 atm laser mixtures containing 0.3% F_2. Under these conditions

44

the excitation was calculated to be 2.2×10^5 W/cm^3 at a discharge current density of 40 A/cm^2.

The e-beam current was adjusted by choosing the e-gun anode cathode spacing. At 7 cm spacing a transmitted e-beam intensity of 2 to 3 A/cm^2 in the discharge region was obtained. Figure 17 shows oscillograms of the e-gun cathode voltage and current pulse shapes. Also shown is the transmitted e-beam current density measured in the laser cavity. Because of diode closure in the e-gun,[5] the current density monotonically increased during the pulse. However, from 0.6 μs to 1.4 μs after the initiation of the e-beam, the transmitted current in the discharge region averaged ~2.5 A/cm^2.

When a discharge voltage was applied across the electrodes it was found that the desired operating electric field of 3 kV/cm-atm can only be maintained for 200 to 300 nsec. Typical discharge voltage and current oscillograms are displayed in Figure 18. Shown are three shots taken with discharge supply capacitor bank charged to 60, 80 and 100 kV respectively. At the higher applied fields the average electric field in the discharge is initially high, but quickly collapsed. At the same time the discharge current increased until limited by the external circuitry. Open shutter photographs of the discharge showed no evidence of a glow to arc transition resulting in the formation of a constricted arc. An example is shown in Figure 19. The electron density appeared to have increased volumetrically which resulted in high discharge currents and low electric fields.

Under these conditions efficient excitation occurred only for a short time during which the electric field was high. Efficient lasing was observed only during that time with laser output pulses typically lasting 200 to 300 nsec and typical output energy was 10 to 20 J.

---

(5)   Parker, R. K., Anderson, R. E., and Duncan C. V., J. Appl. Phys., 45, 2463 (1974).

7 CM E−GUN ANODE−CATHODE SPACING
2 MIL KAPTON

CATHODE
VOLTAGE
↓150 kV/div

TRANSMITTED
E−BEAM
CURRENT ↑
1 A/cm^2/div

CATHODE
↑CURRENT
5 kA/div

TIME 200 ns/div ⟶
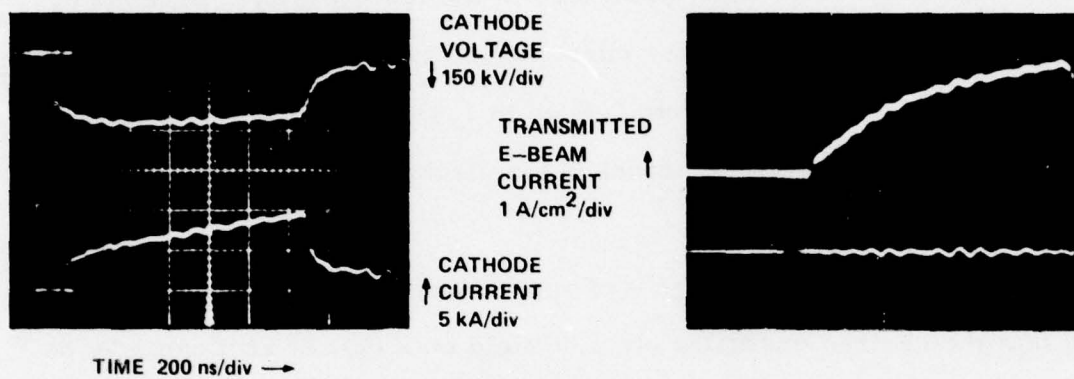
H3724

Figure 17   E-Gun Cathode Voltage and Current, and Transmitted
E-Beam Current Measured in the Laser Cavity

0.3% F_2/6% Kr/93.7% Ar @ 1.5 ATM

CAPACITOR VOLTAGE 60 kV   80 kV   100 kV

E-GUN CATHODE
VOLTAGE 150 kV/div →

DISCHARGE E
1.5 kV/cm/div ←

TIME 200 ns/div →

DISCHARGE J
35 A/cm^2/div →

H 3727
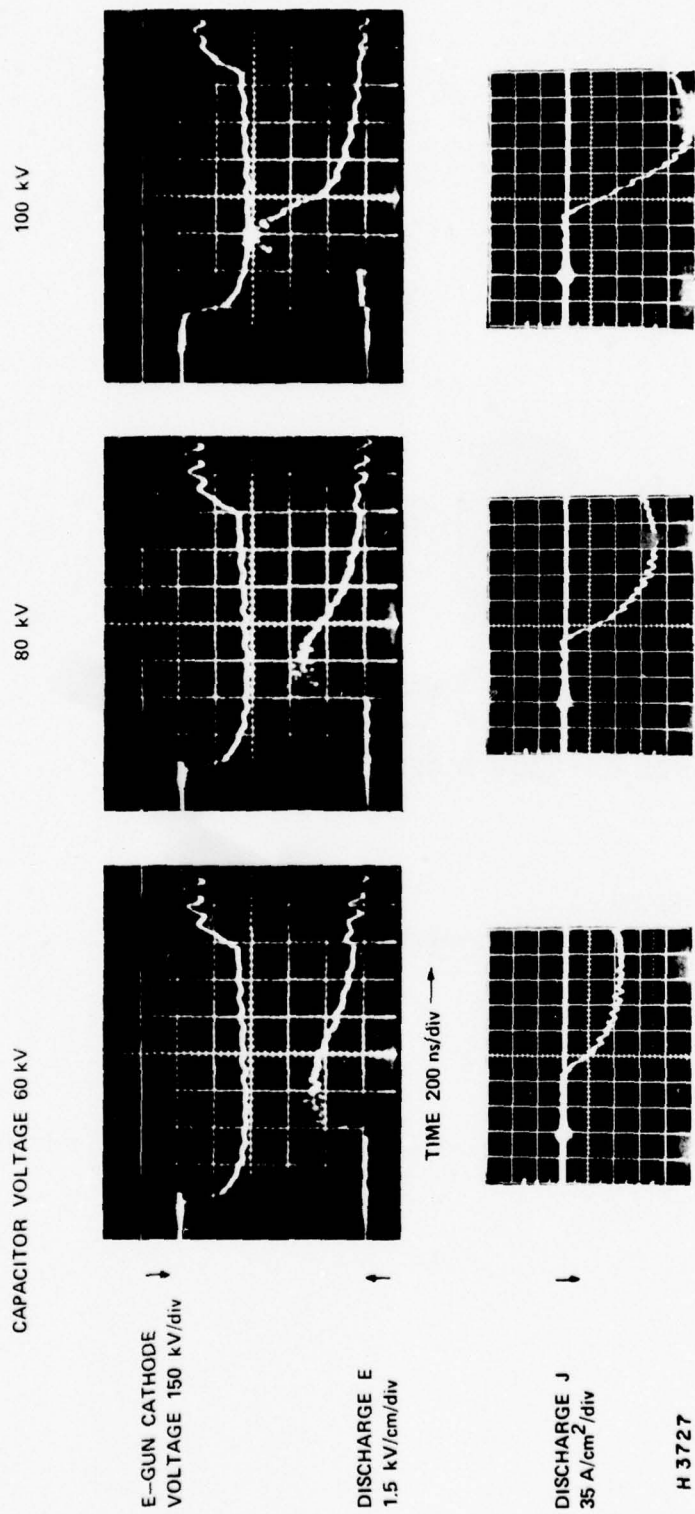
Figure 18   Discharge Voltage and Current Characteristics

47

E—BEAM

FOIL

DISCHARGE CATHODE SCREEN

DISCHARGE ANODE

LASER APERTURE
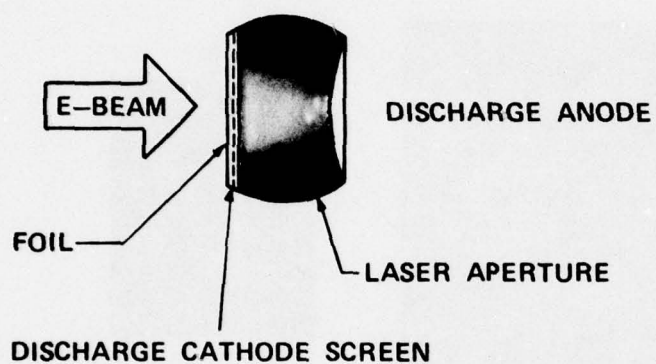
1 μs PULSE
2.5 A/cm^2 E—BEAM
$\approx$ 70 A/cm^2 AVERAGE DISCHARGE CURRENT
.3% F$_2$/6% Kr/93.7% Ar
1.5 ATM

H 3730

Figure 19   Open Shutter Photograph of Visible Fluorescence from
Discharge Excited Laser Mixture

48

Attempts to stabilize the discharge with higher attachment (higher F_2 mixtures) resulted in lower discharge enhancements as expected. Therefore, to reach interesting laser operating regimes with higher F_2 concentrations, the e-beam current density was raised to 4 A/cm^2.

With 4 A/cm^2 e-beam density and 0.5% F_2/10% Kr/89.5% Ar mixture, a discharge enhancement of 2 with electric fields of 2 to 3 kV/cm could be maintained for up to 500 nsec. Efficient lasing was observed during that time. Best results achieved are summarized in Table 1 while typical discharge current, voltage and output laser pulse oscillagrams are shown in Figure 20. In Figure 20 we also compare these to predictions of the kinetic model.

The comparison shows that the calculated e-field assuming uniform e-beam deposition is higher than those actually obtained. We attribute this to e-beam nonuniformities which led to regions of high electron density and low electric field. The calculated discharge voltage decreased for the latter part of the pulse because of F_2 consumption. The observed voltage decrease is faster than that calculated. A possible explanation for this is that F_2 is consumed in the discharge somewhat faster than that accounted for by the model. F_2 is consumed by the following reactions:

$$F_2 + e \rightarrow F^- + F \quad (1)$$
$$F_2 + Kr^* \rightarrow KrF^* + F \quad (2)$$
$$F_2 + h\nu \text{ (laser)} \rightarrow 2F \quad (3)$$
$$F_2 + Ar^* \rightarrow ArF^* + F \quad (4)$$
$$F_2 + KrF^* \rightarrow \text{products} \quad (5)$$
$$F_2 + e \rightarrow 2F + e \quad (6)$$
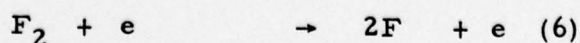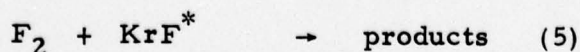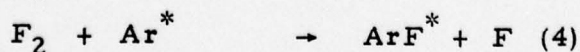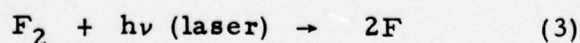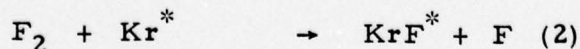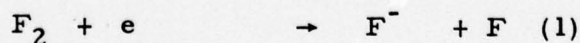
TABLE 1

E-BEAM CONTROLLED DISCHARGE PUMPING OF KrF*
1 METER DEVICE (0.5% F_2/10% Kr/89.5% Ar AT 1.5 ATM)

- **LASER PERFORMANCE**
    - Laser Energy   = 75 Joules
    - Active Volume   = 7.5 Liters
    - Laser Energy Density   = 10 J/Liter
    - Laser Energy/Energy Deposited   = 9.5%
    - Laser Pulse Length   = 500 nsec
    - Output Coupling   = 71%

- **DISCHARGE CHARACTERISTICS**
    - Discharge Electric Field $\simeq$ 2 kV/cm-atm
    - Discharge Current Density   = 70 A/cm^2
    - Discharge Energy Deposited   = 70 J/Liter

- **E-BEAM CHARACTERISTICS**
    - Beam Current Density   = 4 A/cm^2
    - Beam Energy   = 300 keV
    - Beam Energy Deposited   = 35 J/Liter

DISCHARGE PUMPING Kr F LASER COMPARISONS
OF EXPERIMENT AND MODEL PREDICTIONS
(0.5% F$_2$/10% K$_r$/89.5% Ar AT 1.5 ATM)
8 cm ANODE-CATHODE SPACING
1.5 μF CAP, 50 KV, 150 nH SERIES INDUCTANCE
4A/cm^2 ·BEAM CURRENT DENSITY
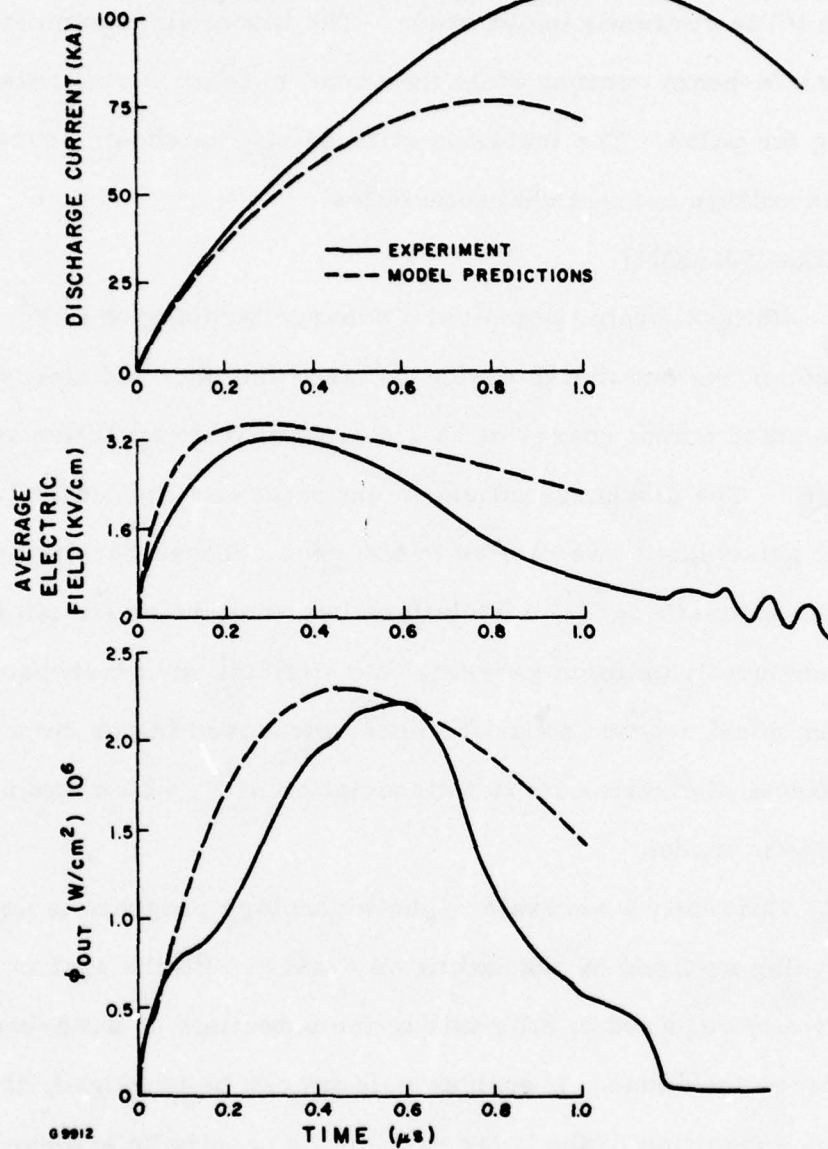
Figure 20   Comparison of Predicted and Measured Discharge and
Laser Output Characteristics

51

In the model reactions (1) through (5) have been included, but (6) have not because the relevant cross sections are not known. The importance of re-action (6) is currently under study. The model also assumes a temporally constant e-beam current while the actual e-beam current rises monotonically during the pulse. The inclusion of these effects should account for the observed voltage current characteristics.

D. CONCLUSIONS

Using e-beam controlled discharge pumping of KrF^* we have demonstrated, in the one meter device, a laser intrinsic efficiency of 10% with a single pulse output energy of 75 J extracted from an active volume of 7.5 ℓ (10 J/ℓ). The discharge enhancement ratio was limited to 2.5 and the laser output pulselength was limited to 600 nsec. These results do not agree with results of kinetic model calculations based on the assumption of a spatially and temporally uniform e-beam. We attribute the discrepancy to the spatial and temporal e-beam nonuniformities measured in our device and to possible effects of electron impact dissociation of F_2 which was not included in the kinetic model.

Currently a separate e-gun technology program is underway at AERL to develop methods of generating an e-beam with the spatial and temporal uniformity required to fully utilize the potentials of the e-beam controlled discharge technique. If such an e-beam can be produced, then uniform energy deposition in the laser medium can easily be achieved by going to two magnetically guided face to face e-beams. A calculated energy deposition profile of such a system is shown in Figure 21. The face to face geometry effectively smoothes out the longitudinal deposition nonuniformities introduced by beam stopping in the laser gas. The implimentation of these techniques should lead to discharge enhancements of > 4 and intrinsic laser efficiencies of > 12% under stable long pulse conditions.

52
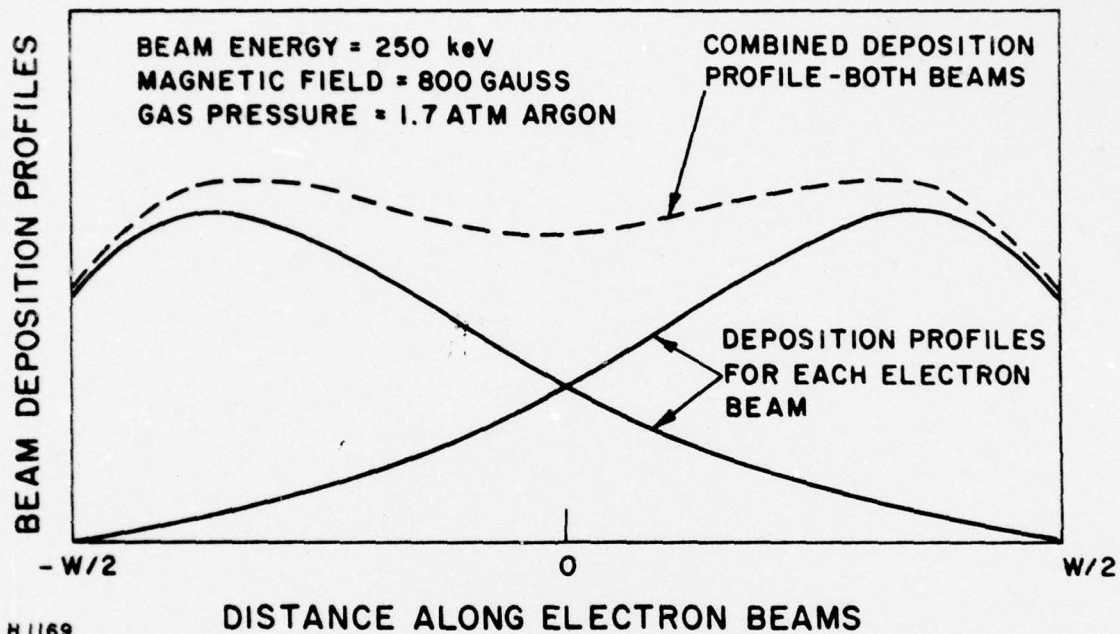
Figure 21   Predicted Longitudinal E-Beam Deposition Profile when
            Two Face to Face E-Beams are Used

IV. E-BEAM PUMPED XeF* LASER

Based on the molecular similarity to KrF*, the XeF* system is expected to possess many of the characteristics of KrF* (e.g., high formation efficiency, high gain, low self-adsorption, etc.). In this section, the results of formation, quenching, gain and adsorption measurements carried out on the small scale device will first be briefly summarized. Results of laser performance calculations based on these measurements will be presented. Then, e-beam pumped XeF* laser experiments will be described and results will be compared with calculations. A series of sidelight experiments performed to resolve the discrepancy between the observed laser efficiency and calculated laser efficiency will be described. The implications of the sidelight measurement results on energy extraction in the XeF* laser will be discussed and finally methods of improving XeF* laser efficiency will be proposed.

A. FORMATION, QUENCHING, GAIN AND ABSORPTION MEASUREMENTS

Efficient scaling of XeF* lasers to high average power requires knowledge of the processes responsible for the formation and quenching of the upper laser level. From the formation kinetics, one can determine the upper level production efficiency, and from quenching rates one can choose appropriate laser mixtures and determine the laser saturation flux.

In XeF* laser mixtures using Ar as a diluent and F_2 as the halogen donor, the dominant kinetic pathways leading to XeF* $(B^2\Sigma^+_{1/2})$ formation have been determined by Rokni et al.,[6] in a series of experiments done on the 20 cm device. Table 2 lists the dominant formation reactions and

_____

(6)   Rokni, et al., Appl. Phys. Lett. 30, 458 (1977).

Figure 22 shows schematically the various pathways. In mixtures containing sufficient Xe so that the rate of reaction (6) in Table 2 is much greater than the rate of decay of ArF^*, the formation of XeF^* from e-beam ionization of Ar and Xe proceeds essentially with unit branching. This implies a XeF^* formation efficiency in suitable mixtures of approximately 17%.

In these mixtures the dominant quenching of XeF^* is by two body reactions with Ar, Xe and F_2, and three body reactions with Ar and Xe with the third body being mainly Ar. These reactions together with their measured rate constants are listed in Table 3. The rates for reaction (1) and (2) were measured by Brashears et al.,[7] while the remaining were measured by Rokni et al. Using these rate constants one can calculate the saturation flux, ϕ_s. ϕ_s is defined as the flux at which the rate of stimulated emission is equal to the sum of the rates for radiative decay and collisional quenching. In mixtures of $Ar/Xe/F_2$ ϕ_s is given by

$$\phi_s = \frac{h\nu}{\sigma_s}\left[\frac{1}{\tau_r} + K_{Xe} N_{Xe} + K_{F_2} N_{F_2} + K_{Ar} N_{Ar} + K_{2Ar} N_{Ar}^2 \right.$$

$$\left. + K_{ArXe} N_{Ar} N_{Xe}\right] \tag{14}$$

where the K's are the rate constants given in Table 3, N are the number densities for the gas species, σ_s is the stimulated emission cross section and τ_r is the radiative lifetime. Taking $\sigma_s = 4 \times 10^{-16}$ cm^2 [8] and $\tau_r = 16$ nsec[9] we get for typical laser mixtures at 2 at total pressure

$$\phi_s = 2\text{-}3 \times 10^5 \text{ W/cm}^2$$

The formation and quenching described above have been incorporated into a comprehensive kinetic code. In Figure 23 the fluorescence versus

(7)   Brashears, H. C., Setser, D. W., and Des Marteau (Unpublished).

(8)   Rokni, M. (Unpublished).

(9)   Eden, G. J. and Searles, S. K. (Unpublished).
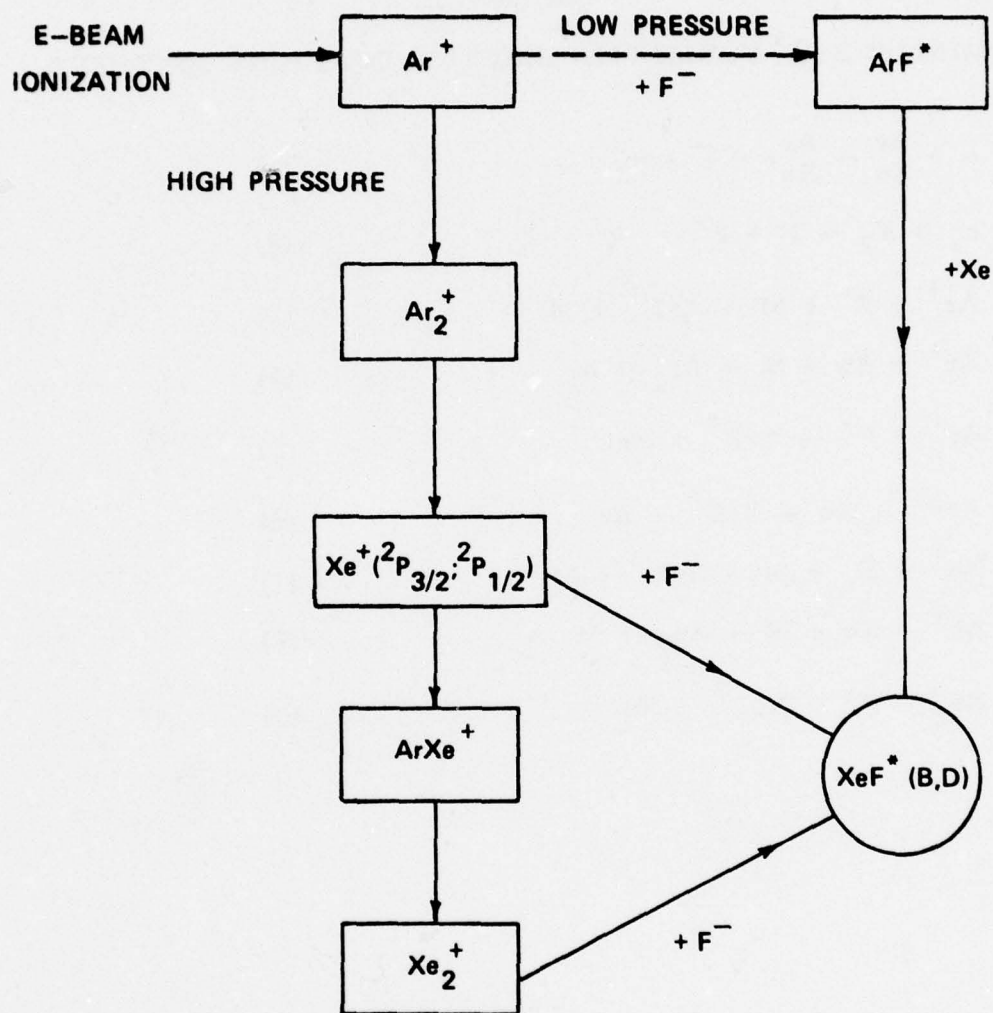
H1443

Figure 22   Dominant XeF* Formation Kinetics in Ar/Xe/F$_2$ Mixtures

57

TABLE 2

DOMINANT XeF* FORMATION KINETICS IN Ar RICH MIXTURES

$$e + \begin{array}{c} Ar \\ Xe \end{array} \rightarrow \begin{array}{c} Ar^+ \\ Xe^+ \end{array} + \vec{e} + e_s \qquad (1)$$

$$e_s + F_2 \rightarrow F + F^- \qquad (2)$$

$$Ar^+ + F^- + M \rightarrow ArF^* + M \qquad (3)$$

$$Ar^+ + Ar + M \rightarrow Ar_2^+ + M \qquad (4)$$

$$Ar_2^+ + F^- \rightarrow ArF^* + Ar \qquad (5)$$

$$ArF^* + Xe \rightarrow XeF^* + Ar \qquad (6)$$

$$Xe^+ + F^- + M \rightarrow XeF^* + M \qquad (7)$$

$$Xe^+ + Xe + M \rightarrow Xe_2^+ + M \qquad (8)$$

$$Xe_2^+ + F^- \rightarrow XeF^* + Xe \qquad (9)$$
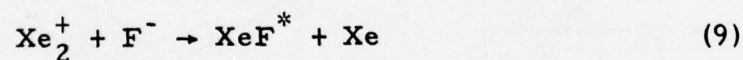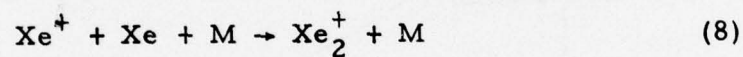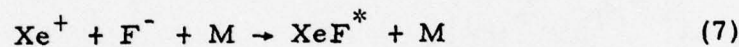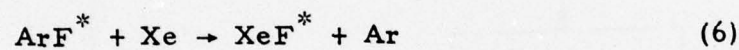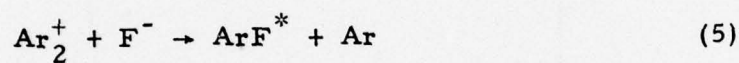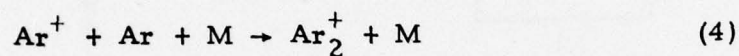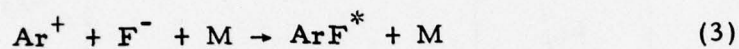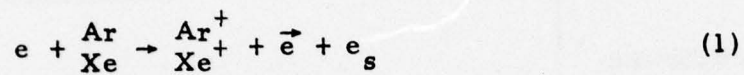
TABLE 3

DOMINANT XeF* QUENCHING KINETICS IN Ar/Xe/F$_2$ MIXTURES

$$XeF^* + Xe \rightarrow products \qquad 3.4 \times 10^{-11} \, cm^3/sec \qquad (1)$$

$$XeF^* + F_2 \rightarrow products \qquad 3 \times 10^{-10} \, cm^3/sec \qquad (2)$$

$$XeF^* + A_r \rightarrow products \qquad 8 \pm 4 \times 10^{-13} \, cm^3/sec \qquad (3)$$

$$XeF^* + A_r \rightarrow products \qquad 1.5 \pm .5 \times 10^{-32} \, cm^6/sec \qquad (4)$$

$$XeF^* + Xe + M \rightarrow products \qquad 3 \pm 1.5 \times 10^{-31} \, cm^6/sec \qquad (5)$$

G8557
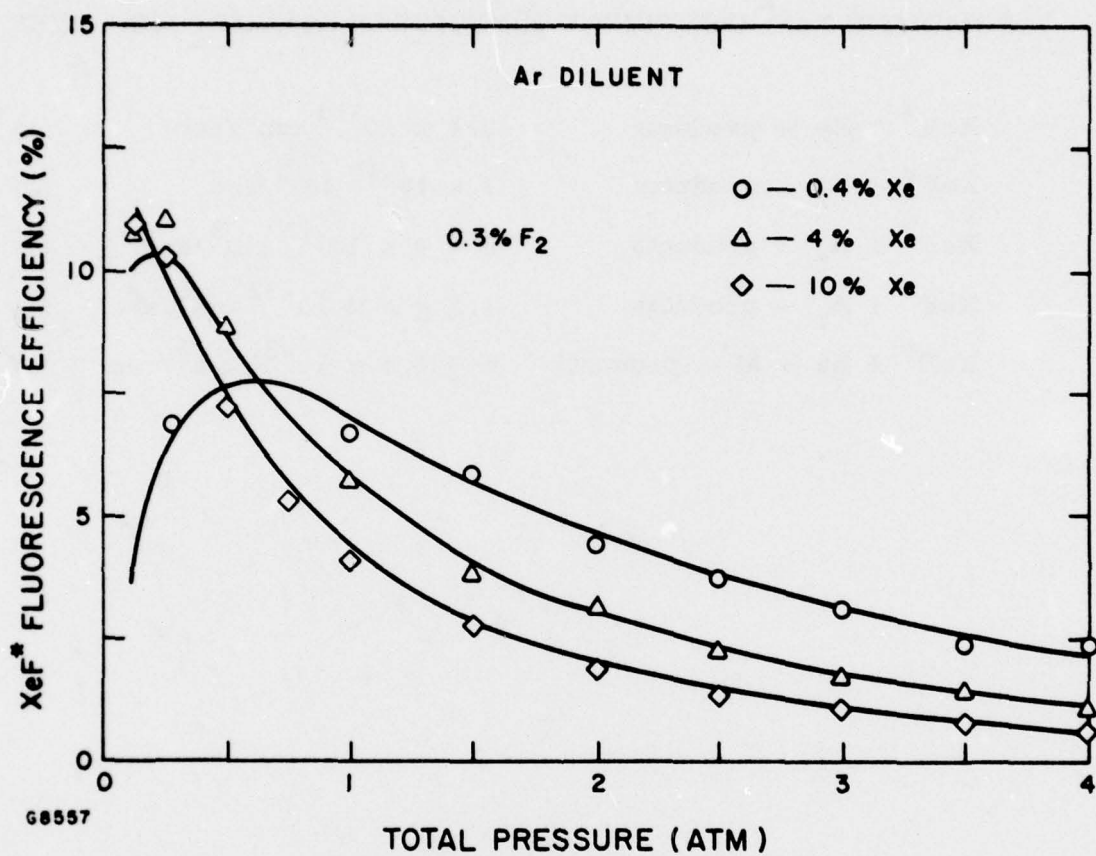
Figure 23   Predicted and Measured XeF* Fluorescence vs Pressure
for Various Xe Concentrations in Ar/Xe/F$_2$ Mixtures

pressure and mixture predictions of the kinetic code are compared with experimental measurements. At low pressures the fluorescence efficiency is higher for mixtures with high Xe concentration because the displacement reaction $Xe + ArF^* \rightarrow XeF^* + Ar$ competes more effectively with the decay of ArF^* while at higher pressures, two and three body quenching by Xe cause the fluorescence to roll over faster for high Xe concentrations.

Beside Ar and F_2, NF_3 have been used as the halogen donor and Ne have been used as a diluent. The use of NF_3 has the advantage that NF_3 quenches XeF^* some 16 times slower than F_2.[7] Further NF_3 does not absorb at the laser wavelength. The use of Ne as a diluent has been shown to lead to higher XeF^* laser efficiency.[10, 11] As will be shown below this is due predominantly to lower excited species absorption and slower quenching.

The formation kinetics in Ne rich mixtures have not been firmly established, however measurements show that the branching into XeF^* is near unity for appropriate mixtures. A possible formation chain that is consistent with our fluorescence observations is given in Table 4 and Figure 24.[12] An interesting feature of this chain is that Xe^+ is formed through reactions. with NeF^*, F^* and F_2^*. All these species have enough energy only to form Xe^+ in the $(^2P_{3/2})$ state but not $^2P_{1/2}$ state. Since $Xe^+ (^2P_{1/2})$ generates XeF^* (D) states, one expects to find, in Ne rich mixture, much weaker D-X emission at 260 nm. This is indeed what is observed.

The dominant quenching reactions in $Ne/Xe/NF_3$ mixes are listed in Table 5. Also shown are the measured rate constants. The rate constants for three body quenching by Xe and Ne with Ne as the third body was measured by Rokni et al.,[13] in the 20 cm device. Two body quenching by Ne

(10)   Champagne, L. F., et al., presented at the 7th Winter Colloquium on High Power Visible Lasers.

(11)   Mangano, J. A., Hsia, J., and Hawryluk, A. M. (Unpublished).

(12)   Rokni, M. and Jacob, J. (Unpublished).

(13)   Rokni, M. et al. (to be published in Appl. Phys. Lett.)

TABLE 4

XeF^* FORMATION KINETICS IN $Ne/Xe/NF_3$ MIXTURES

$$\vec{e} + Ne \rightarrow Ne^+ + e_s + \vec{e} \tag{1}$$

$$e_s + NF_3 \rightarrow NF_2 + F^- \tag{2}$$

$$Ne^+ + 2Ne \rightarrow Ne_2^+ + Ne \tag{3}$$

$$Ne^+ + F^- + M \rightarrow NeF^* + M \tag{4}$$

$$Ne_2^+ + F^- \rightarrow NeF^* + M \tag{5}$$

$$NeF^* \rightarrow Ne + F^* \tag{6}$$

$$F^* + NF_3 \rightarrow F_2^* + NF_2 \tag{7}$$

$$\left. \begin{array}{c} F^* \\ NeF^* \\ F_2^* \end{array} \right\} + Xe \rightarrow Xe^+ \tag{8}$$

$$Xe^+ + F^- + M \rightarrow XeF^* + M \tag{9}$$
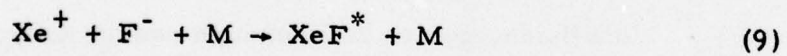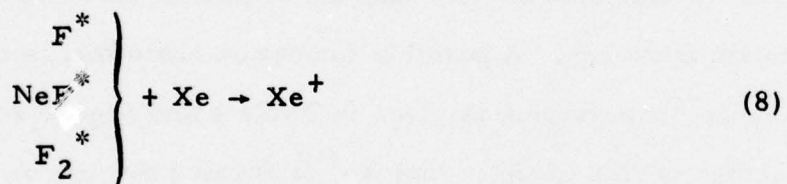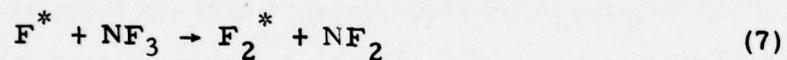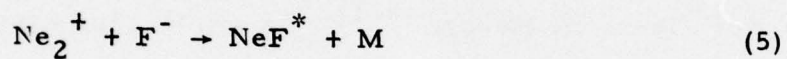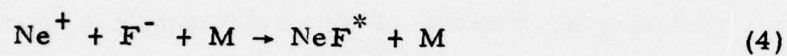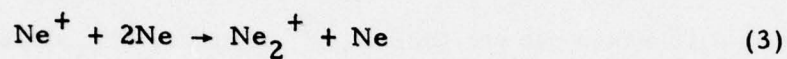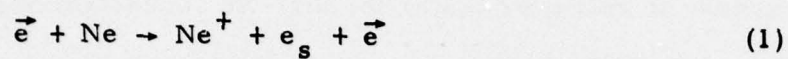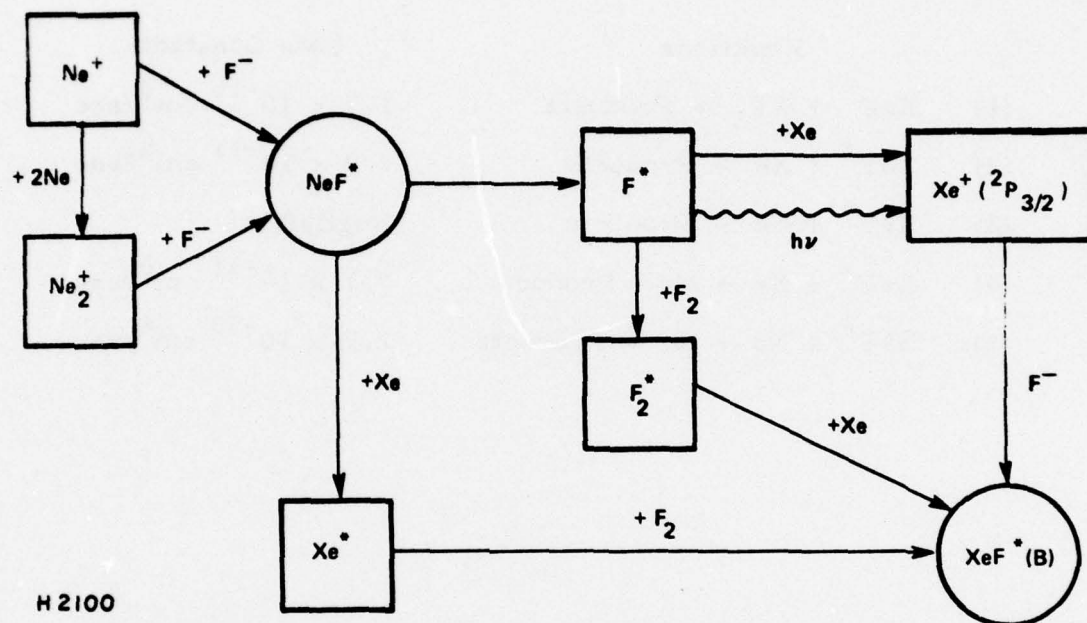
Figure 24   Possible YeF* Formation Processes in E- Beam Excited Ne/Xe/F$_2$ Mixtures

H 2100

TABLE 5

DOMINANT XeF^* QUENCHING PROCESSES IN $Ne/Xe/NF_3$ MIXTURES

	Reactions	Rate Constants
(1)	$XeF^* + NF_3 \rightarrow$ Products	1.7×10^{-11} cm^3/sec
(2)	$XeF^* + Xe \rightarrow$ Products	2.9×10^{-11} cm^3/sec
(3)	$XeF^* + Ne \rightarrow$ Products	Negligible
(4)	$XeF^* + Xe + M \rightarrow$ Products	7.7×10^{-31} cm^6/sec
(5)	$XeF^* + Ne + Ne \rightarrow$ Products	2.7×10^{-33} cm^6/sec

is small and can in general be neglected. Using these quenching rate constants we calculate for typical laser mixtures at 4 atm total pressure a saturation flux

$$\phi_s \approx 1\text{-}2 \times 10^5 \text{ W/cm}^2$$

The fluorescence efficiency versus pressure and mixture predictions of the kinetics code which incorporates the above rates are compared in Figure 25 with experimental measurements. Note that since branching from Ne^+ and Xe^+ is near unity for appropriate mixtures, and the formation efficiency is 14% (3.52 eV per XeF^* formed/25 eV per electron ion pair formed by the e-beam in mixtures of Ne and Xe).[14] The observed fluorescence efficiency is lower because of quenching. If extraction can occur efficiently the laser efficiency can be significantly higher than the peak fluorescence efficiency observed.

For efficient laser operation another key issue is medium absorption at the laser wavelength. Here for XeF^*, laser medium absorption is expected to be lower than KrF^*. First by using NF_3 as a halogen donor there is no ground state absorption at 3500 Å and second XeF^* is not expected to self-adsorb.

Systematic adsorption measurements have been carried out in XeF^* mixtures. A schematic of the measurement apparatus is shown in Figure 26. A dye laser tuned to 340 nm was used to probe the active medium. Part of the probe beam was reflected by a beam splitter and monitored by a photodiode. The optical path through the active medium was doubled by a total reflector placed at the far end of the cell. After emerging from the cell, the beam was monitored with a second photodiode narrow band interference filter with peak transmission at 340 nm was used in front of the detector to

(14) Jesse, W. P. and Sadauskis, J., Phy. Rev. 88, 417L (1952).
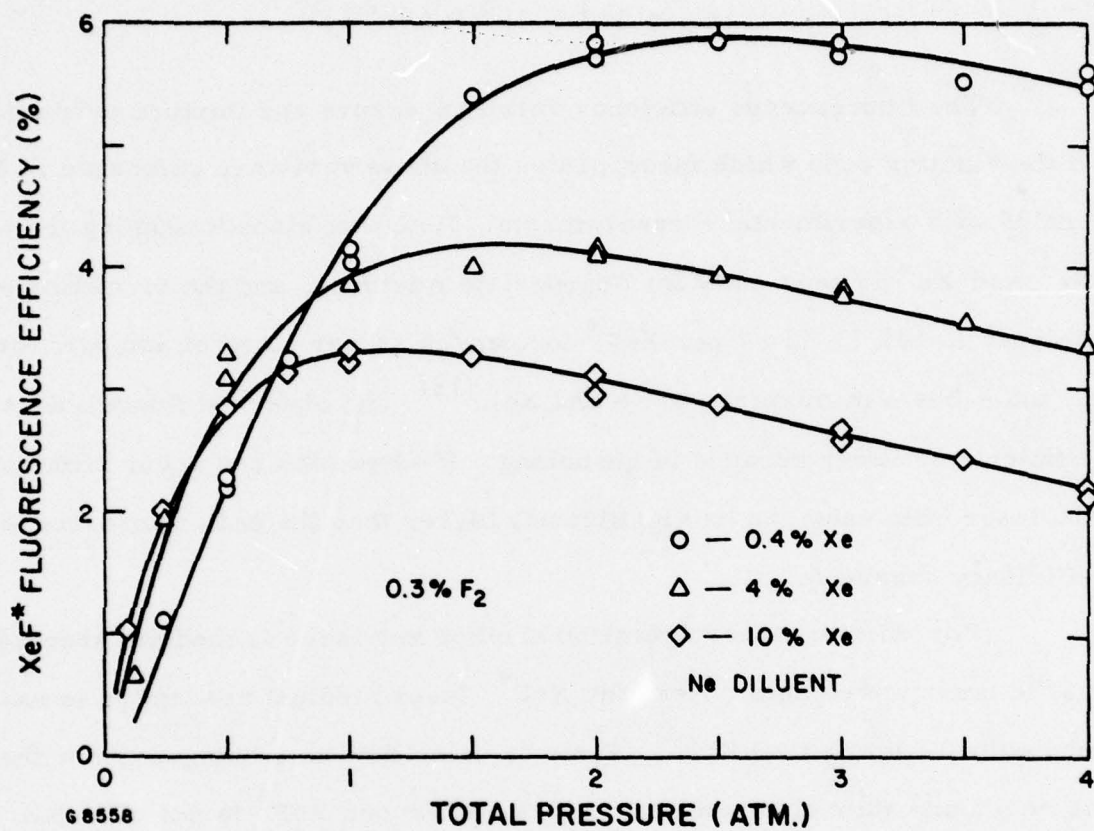
Figure 25   Predicted and Measured Fluorescence Efficiencies in
E-Beam Excited Ne/Xe/NF$_3$ Mixtures
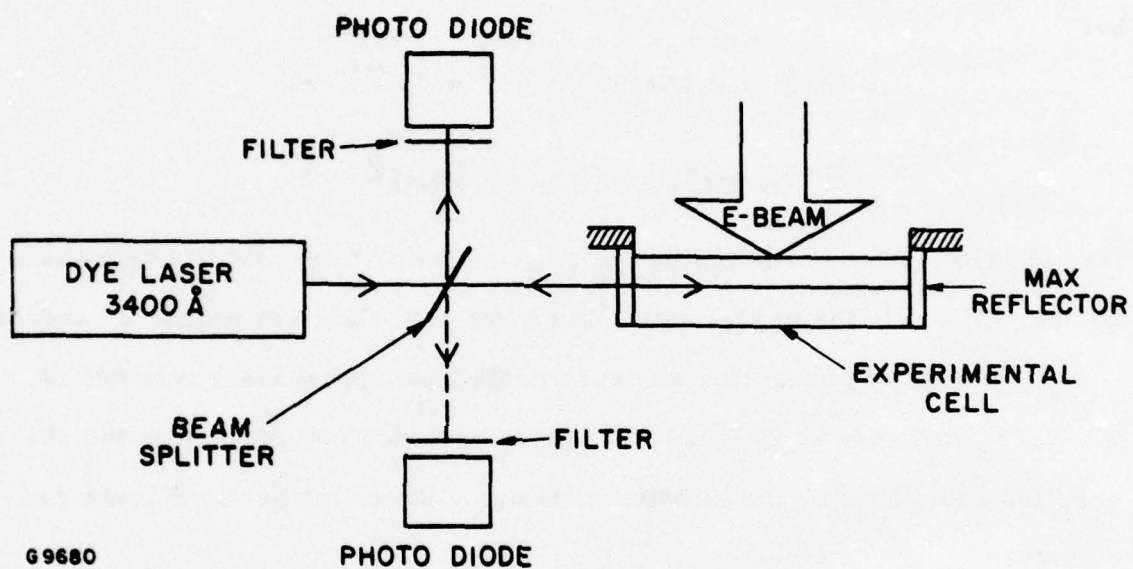
Figure 26   Schematic of Experimental Apparatus for Absorption
Measurements in XeF^* Mixtures

minimize optical noise. The dye laser was synchronized with the e-beam. The adsorption of the active medium was measured by comparing the ratio of the signals with and without 5 A/cm^2 of e-beam irradiation.

Results of adsorption measurements in 0.3% F_2/99.7% Ar and in 0.3% F_2/99.7% Xe are shown in Figures 27 and 28. If Ar_2^+, Ar_2F^* and Xe_2^+ are identified as the dominant adsorbing species with cross sections given by:

$$\sigma (Ar_2^+) = \sigma (Ar_2F^*) = 1.7 \times 10^{-17} \ cm^2$$

$$\sigma (Xe_2^+) = 1.3 \times 10^{-16} \ cm^2$$

then the absorption predicted by the kinetics code yield good fits to measured values. The calculated absorption lines are also shown in Figure 27 and 28.

Results of absorption measurements in a typical laser mixture of Ar/Xe/F_2 are shown in Figure 29. Also shown for comparison is the absorption calculated by the kinetics code using the cross sections found previously.

Photoabsorption in Ne/Xe/F_2 mixtures have also been investigated. The measured excited species absorption in 0.3% F_2/0.5% Xe/99.2% Ne and 0.3% F_2/2% Xe/97.7% Ne are shown in Figure 30. Note that the absorption is much less than mixtures with Ar. The two main reasons for the reduced absorption are (1) Ne_2^+ absorbs much less than Ar_2^+ and (2) Xe_2^+ formation is slower in mixtures containing mostly Ne because the intermediate complex $NeXe^+$ is more weakly bound than $ArXe^+$. From these measurements one can establish an upper bound for Ne_2^+ absorption cross-section of 2×10^{-17} cm^2. Table 6 compares the experimentally derived cross sections to those calculated theoretically. The theoretical cross sections are expected to be good to a factor of 2. [15]

(15)   Wadt, W. (to be published).

68
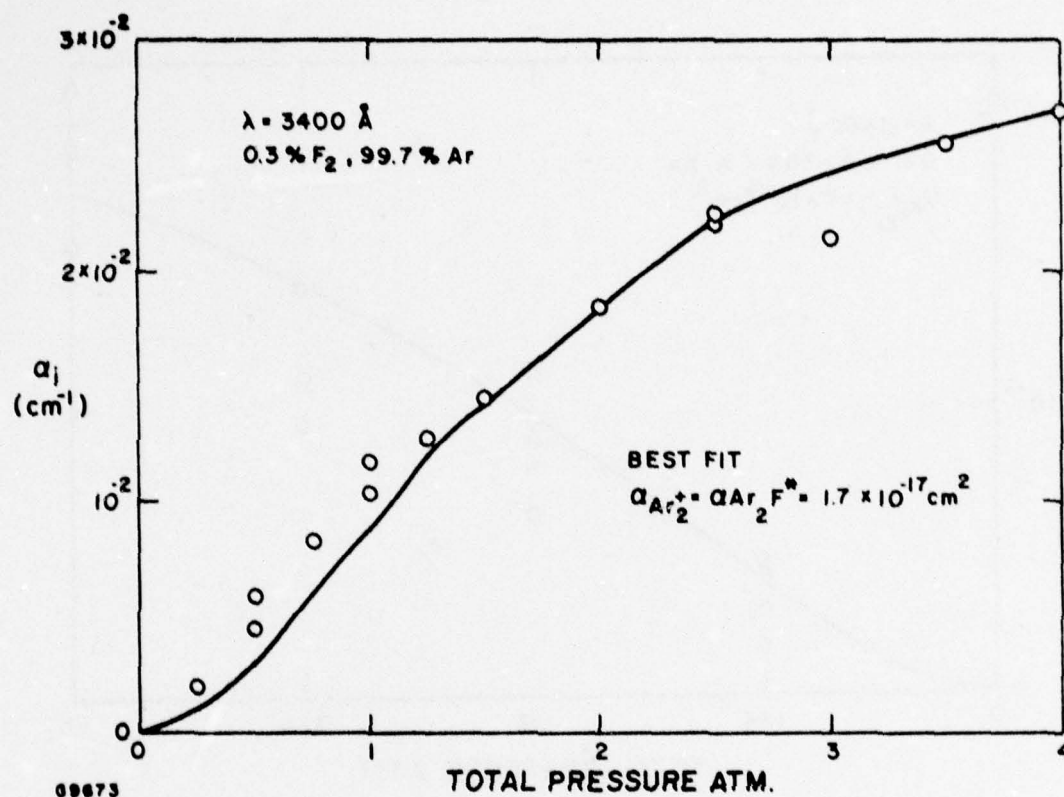
Figure 27   3400 Å Absorption in E-Beam Excited F_2/Ar Mixtures
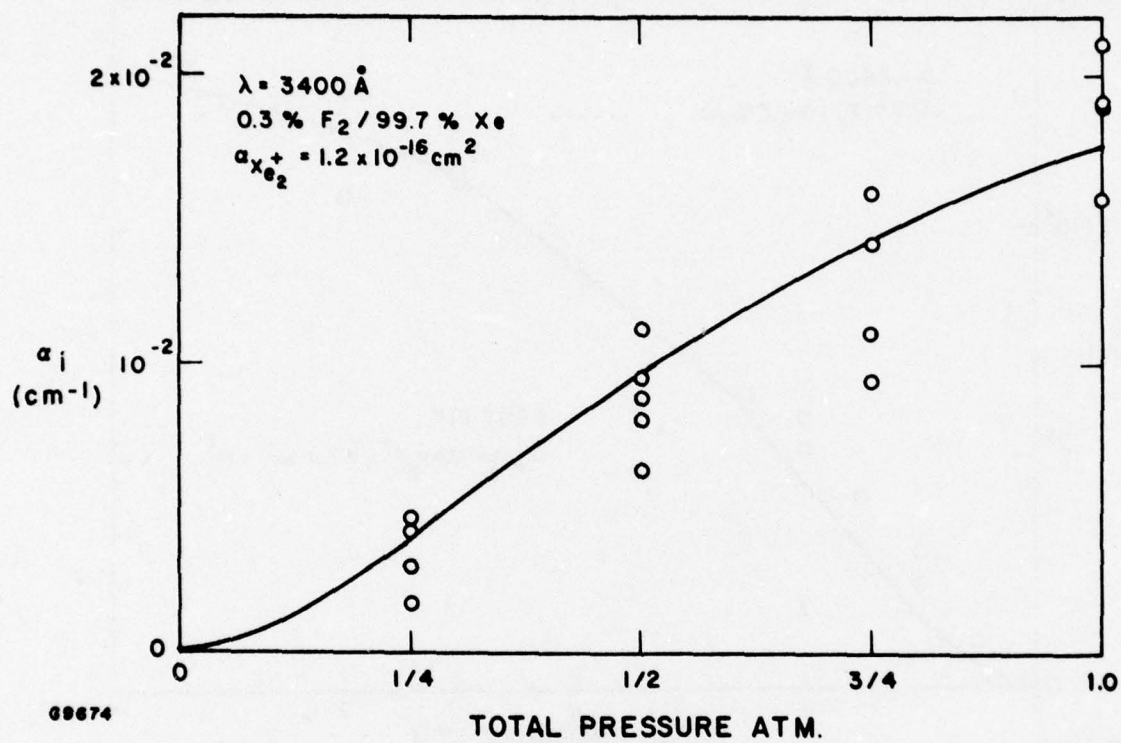
Figure 28   3400 Å Absorption in E-Beam Excited F_2/Xe Mixtures
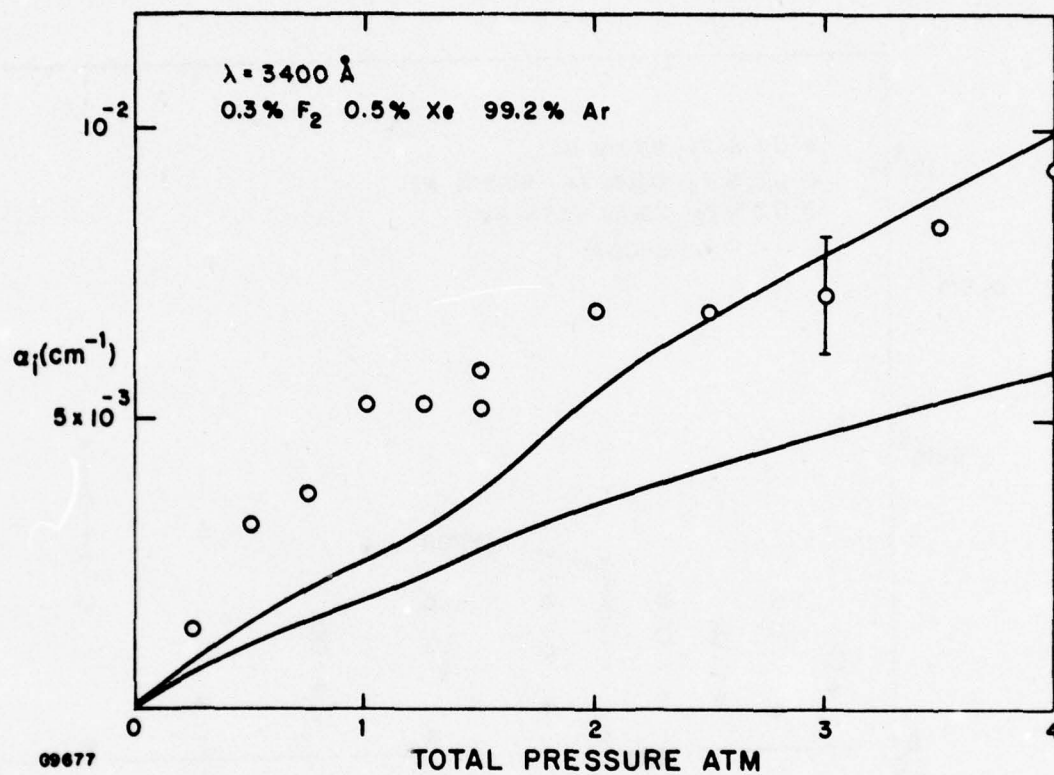
Figure 29   3400 Å Absorption in E-Beam Excited Ar/Xe/F_2 Mixtures
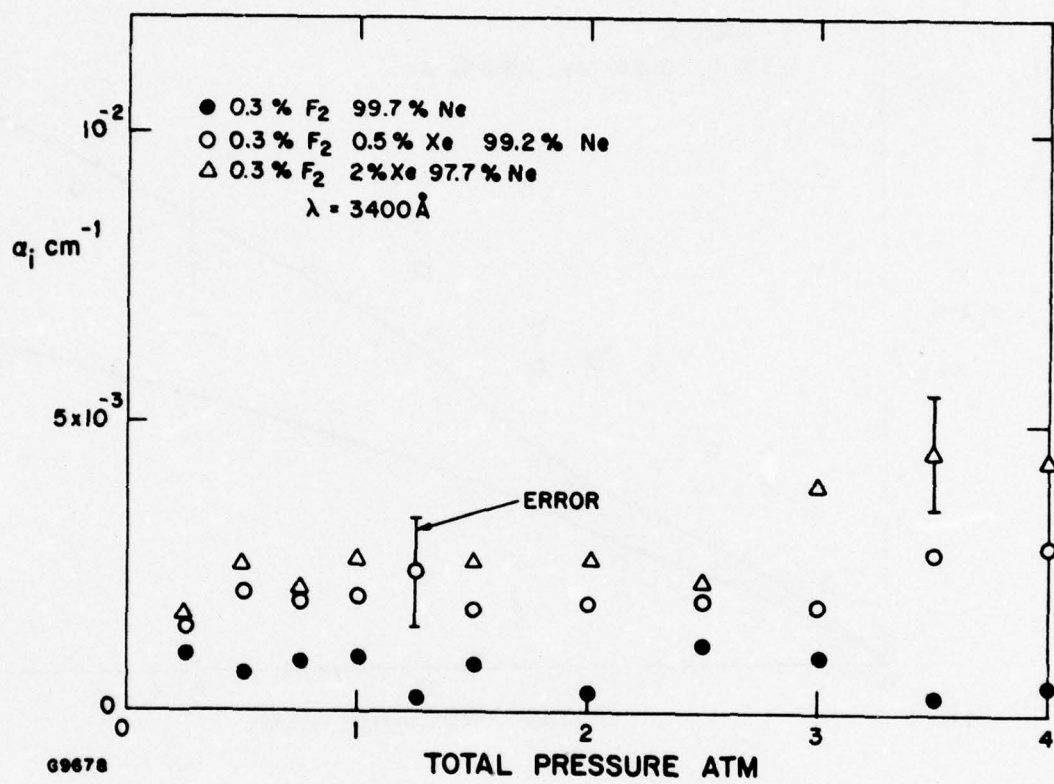
Figure 30   3400 Å Absorption in E- Beam Excited Ne/Xe/F$_2$ Mixtures

72

TABLE 6

DOMINANT ABSORPTION SPECIES IN XeF LASERS

$\sigma \ (cm^2)$

Species	Exp	Theor (300 °K)
Ar_2^+	1.7×10^{-17}	8.7×10^{-18}
Xe_2^+	1.3×10^{-16}	4.8×10^{-17}
Ne_2^+	$< 2 \times 10^{-17}$	9.6×10^{-19}

Now the superiority of Ne as a diluent is apparent. Since both two and three body by Ne is much less than Ar, and since the branching into XeF^* is just as efficient, one expects, for the same level of excitation a higher small signal gain. Further since the absorption in Ne mixtures is some 3 times less than that with Ar, the extraction efficiency should be much higher when Ne is used.

B. LASER EFFICIENCY CALCULATIONS AND COMPARISON WITH EXPERIMENT

If one assumes that the vibrational relaxation of the $XeF^*(B)$ manifold and the removal of the lower laser state $XeF(x)$, occurs much faster than the rate of radiative decay and collisional quenching of $XeF^*(B)$, then using the formation and quenching kinetics measured in the previous section one can calculate the extraction efficiency and intrinsic laser efficiency.

Since the branching into $XeF^*(B)$ is near unity the rate equation for $XeF^*(B)$ can be written

$$\frac{d\,N_{XeF^*}}{dt} = S_{eb} - \frac{N_{XeF^*}}{\tau_E} \tag{15}$$

Where N_{XeF^*} is the density of XeF^*, S_{eb} is the e-beam ionization rate and τ_E is the lifetime of XeF^*. In mixture of $Ne/Xe/NF_3$ τ_E is given by

$$\frac{1}{\tau_E} = \frac{1}{\tau_r} + K_{NF_3} N_{NF_3} + K_{Xe} N_{Xe} + K_{XeNe} N_{Xe} N_{Ne} + K_{2Ne} N_{Ne}^2 \tag{16}$$

In 4 atm of 0.2% NF_3/0.5% Xe/99.3% Ne we have, using the quenching rates presented previously,

$$\frac{1}{\tau_E} = 1.46 \times 10^8 \text{ sec}^{-1}$$

74

For a 250 kV e-beam at 10 A/cm^2 in 4 atm of Ne

$$S_{eb} = 5 \times 10^{22}/\text{sec} - \text{cm}^3$$

and $N_{XeF^*} \approx 3.5 \times 10^{14}$.

The small signal gain g_o is then given by

$$g_o = \sigma_s N_{XeF^*} = 1.4 \times 10^{-1}/\text{cm}.$$

Using the laser power extraction model which includes distributed medium absorption presented in the previous semi-annual report[1] and assuming a medium absorption of $a = 3 \times 10^{-3}$ cm^{-1} we have for the maximum extraction tion for a 1-meter active medium, $\eta_{ext} \approx 0.7$. The intrinsic laser efficiency η_{int} is then just the product of the formation efficiency, η_f and η_{ext}. The maximum expected laser intrinsic efficiency is then

$$\eta_{int} = \eta_f \eta_{ext} \approx 9.8\%.$$

The results of laser experiments carried out in 4 atm of 0.2% NF$_3$/ 0.5% Xe/97.3% Ne are summarized in Table 7. Note that the maximum laser efficiency obtained is a factor of 4 lower than that calculated above. To resolve this discrepancy and to understand the possible sources of inefficiency a series of laser sidelight experiments were performed. These experiments will be described in the following section. The results of these experiments and their implications on power extraction in the XeF* laser will also be discussed in detail.

C. SIDELIGHT EXPERIMENTS AND POWER EXTRACTION IN XeF* LASERS

The laser transiton in XeF* occurs between bound-bound molecular energy levels. The energy level diagram for the XeF*(B) and XeF(x) states

TABLE 7

E-BEAM PUMPED XeF* LASER PERFORMANCE
(0.2% NF$_3$/0.4% Xe/99.4% Ne AT ATM)

- **Laser Performance**

  - Laser Energy   = 36 Joules

  - Active Volume   = 4.5 Liters

  - Laser Energy Density   = 8 J/Liter

  - Laser Energy/Energy   = 2.6%
    Deposited

  - Laser Pulse Length   = 1.2 μsec

- **E-Beam Characteristics**

  - Beam Current Density   = 10 A/cm^2

  - Beam Energy   = 250 keV

are illustrated in Figure 31. These have been derived from spectroscopic analysis of the B → X emission by J. Tellinghuise[16] and others.[17] Note that the lower laser level is bound by approximately 1200 cm^{-1}. This is quite different from the case of KrF* where the lower laser level is repulsive.

In the case of a laser working from bound-bound transitions, there is first the possibility of "bottlenecking". That is the deactivation of the lower level (which presumably occurs through collisions) may not be sufficiently fast to allow high extraction efficiency. Second, because radiation from bound-bound transitions typically have discrete vibrational band structure, if lasing occurs predominantly in one V' → V'' transition, then the laser cavity flux can only stimulate transitions from one vibrational level in th upper level manifold. In that case if the vibrational relaxation in the upper manifold is not sufficiently fast, then extraction can only occur from one vibrational level in the upper manifold, and molecules formed in the other vibrational levels are simply lost to spontaneous radiation and collisional quenching.

To see if indeed these processes are limiting the extraction efficiency in the XeF* laser a series of laser sidelight experiments were performed. A schematic of the experimental apparatus is shown in Figure 32. Fluorescence emerging from the side of the 1-meter laser cavity was monitored with photodiodes and a Hilgar spectrograph. The laser cavity flux was also monitored by photodiodes located behind one of the optical cavity mirrors. Thin film interference filters were used in front of the photodiodes so that emission in specific V' → V'' transitions could be monitored. Sidelight intensities were then compared with and without a laser cavity flux under otherwise identical discharge conditions.

(16) Tellinghuisen, J., et al., "Analysis of Spontaneous and Laser Emission from XeF" (to be published).

(17) Smith, A. L., and Kobrinsky, P. C. (to be published).
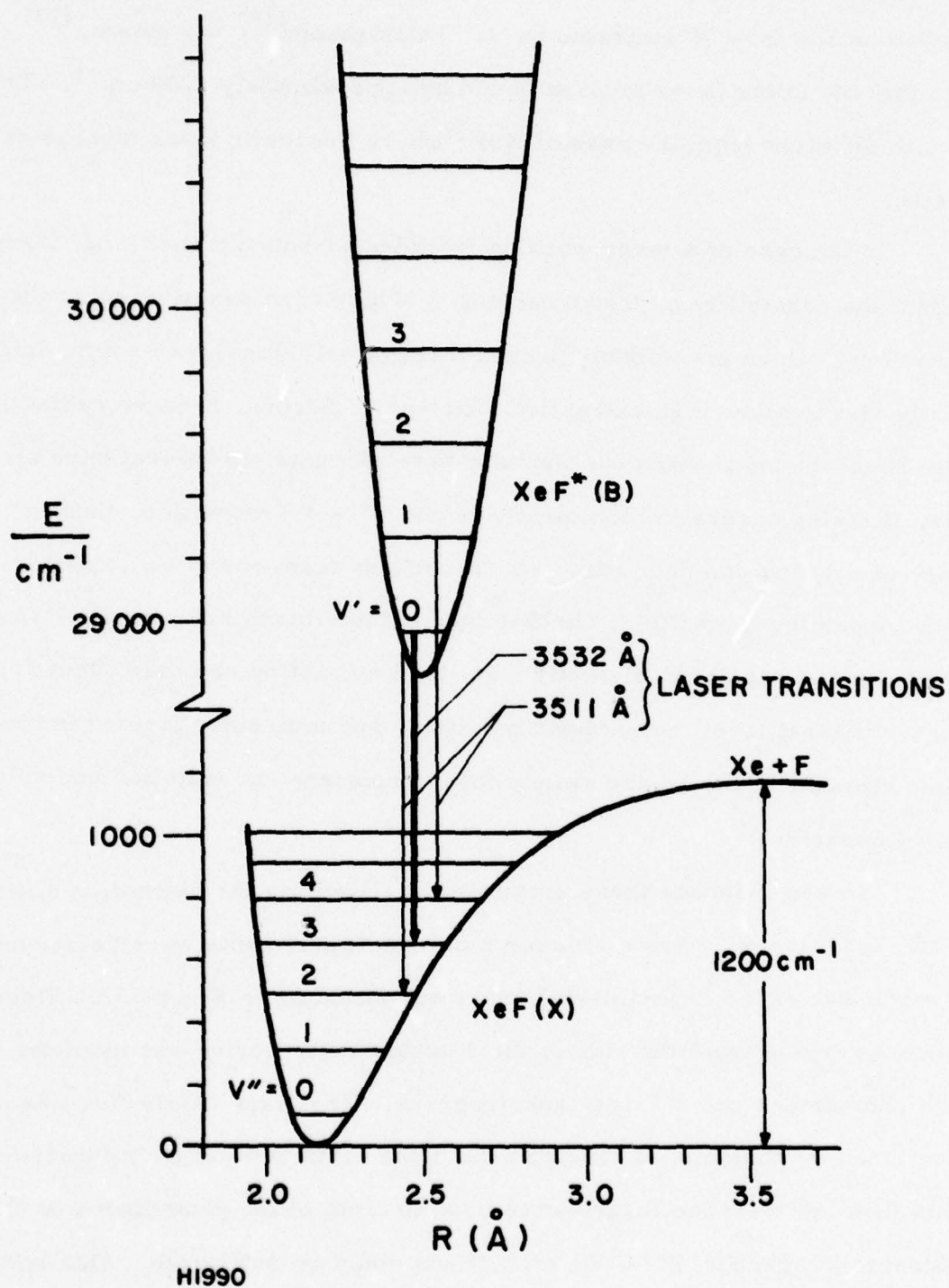
Figure 31   Energy Level Diagram for XeF*(B) and XeF(x) States
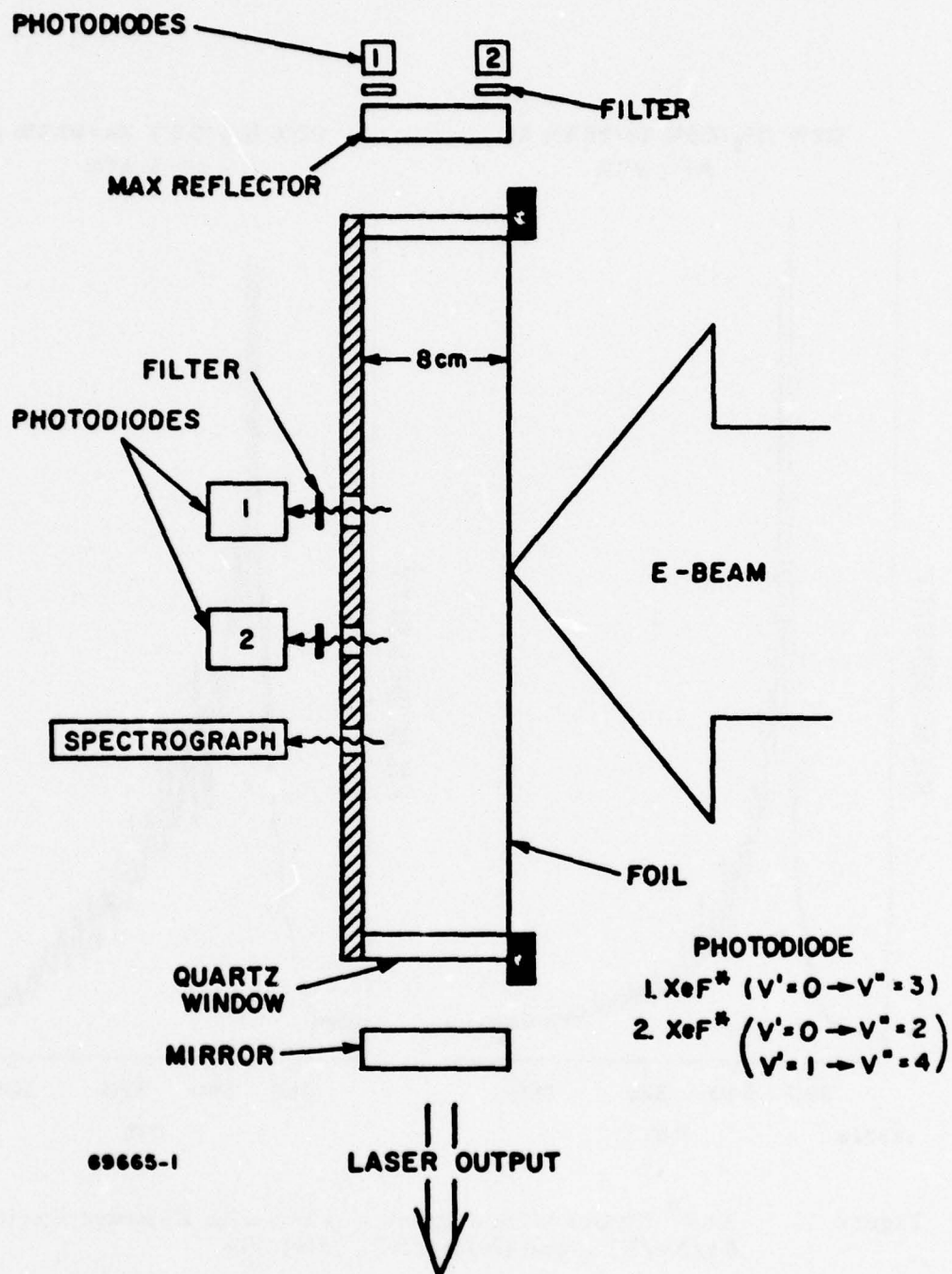
Figure 32   XeF* Sidelight Measurement Apparatus

PHOTODIODES

FILTER

MAX REFLECTOR

FILTER

PHOTODIODES

1

2

8cm

E -BEAM

SPECTROGRAPH

FOIL

QUARTZ WINDOW

MIRROR

PHOTODIODE
1. XeF* $(V'=0 \rightarrow V''=3)$
2. XeF* $\begin{pmatrix} V'=0 \rightarrow V''=2 \\ V'=1 \rightarrow V''=4 \end{pmatrix}$

69665-1   LASER OUTPUT
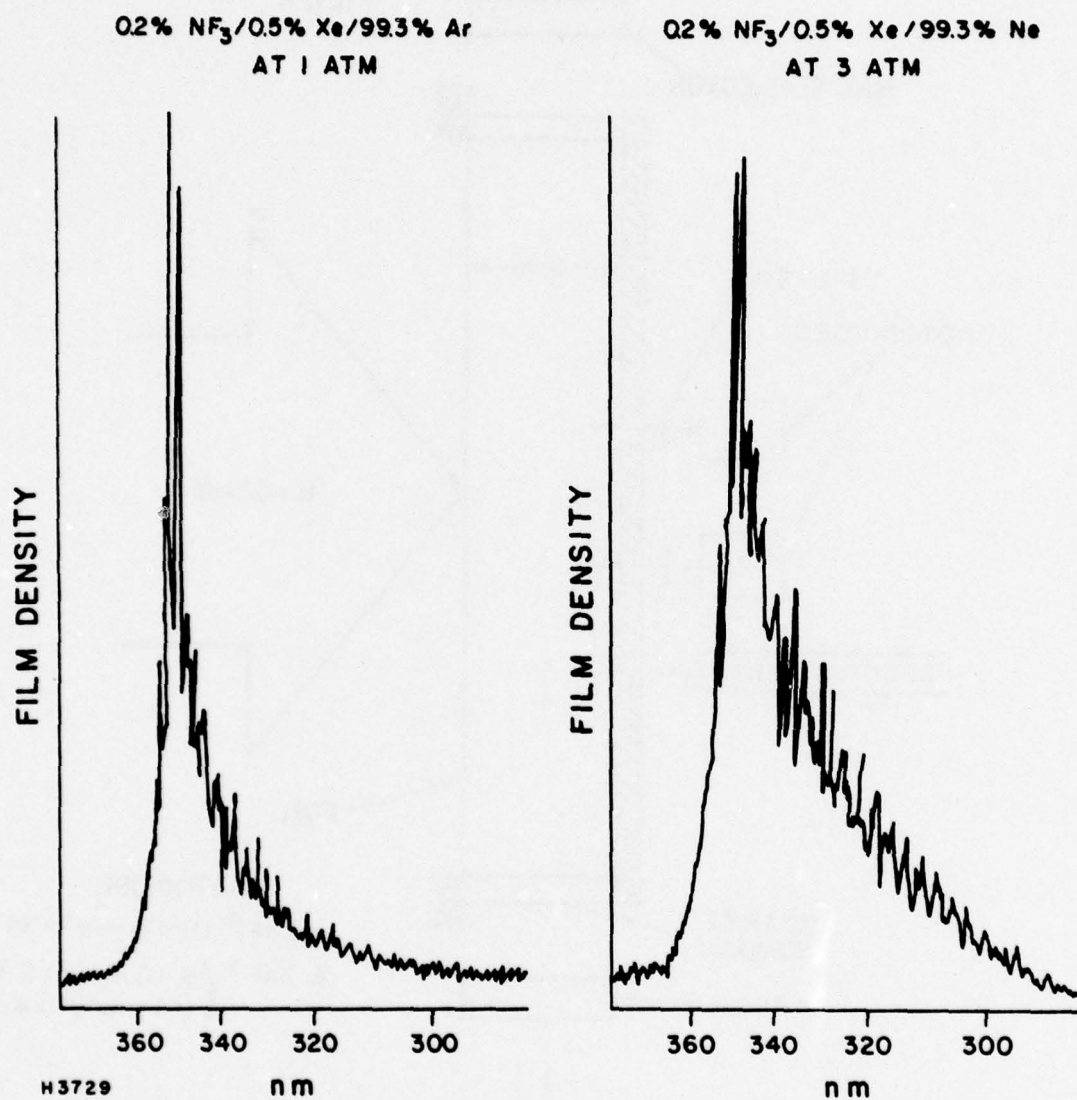
Figure 33   XeF* Fluorescence Spectra taken with E- Beam Excited
Ar/Xe/NF₃ and Ne/Xe/NF₃ Mixtures

80

In Figure 33 we compare $XeF^*(B \to X)$ fluorescence spectra taken
in 1 atm of 0.2% NF_3/0.5% Xe/99.3% Ar to that taken in 3 atm of 0.2% NF_3/
0.5% Xe/99.3% Ne. Note that since the spectra shown were obtained from
microdensitometer tracings, the vertical scales in Figure 33 corresponds to
film density which in turn is approximately proportional to the log of the time
integrated fluorescence intensity. A striking difference in the two spectra is
that in 1 atm of Ar the spectrum is considerably narrower than that from
3 atm of Ne, indicating that in Ar, vibrational relaxation of the upper mani-
fold is more complete than in Ne. This suggests that vibrational relaxation
of $XeF^*(B)$ in Ar mixtures probably does not occur through a V - T process,
since in that case one would expect greater vibrational relaxation in Ne mix-
tures. One possible explanation is that vibrational relaxation in Ar mixture
proceed via the formation of an intermediate complex. Since $ArXe^+$ is bound
by approximately 0.2 eV, vibrational relaxation can occur through

$$XeF^* (high \; V') + Ar \to ArXeF^* \to XeF^* (low \; V') + Ar \,.$$
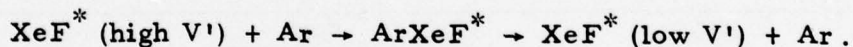
This process is probably not as effective in Ne because $NeXe^+$ is either very
weakly bound or unbound.

Spectra taken of the laser output indicates that in both Ar and Ne mix-
tures lasing occur predominantly in the $V' = 0$ to $V'' = 3$ transition at
3532 Å. Very weak lasing is detected in the band corresponding to a blend
of $V' = 0$ to $V'' = 2$ and $V' = 1$ to $V'' = 4$ transitions at 3511 Å. Figure
34 compares sidelight spectra taken in 3 atm of Ne with and without a laser
cavity flux. The location of the band heads for various $V' \to V''$ transitions
are also shown. With lasing one sees that the fluorescence was significantly
depressed only in those lines corresponding to transitions originating from
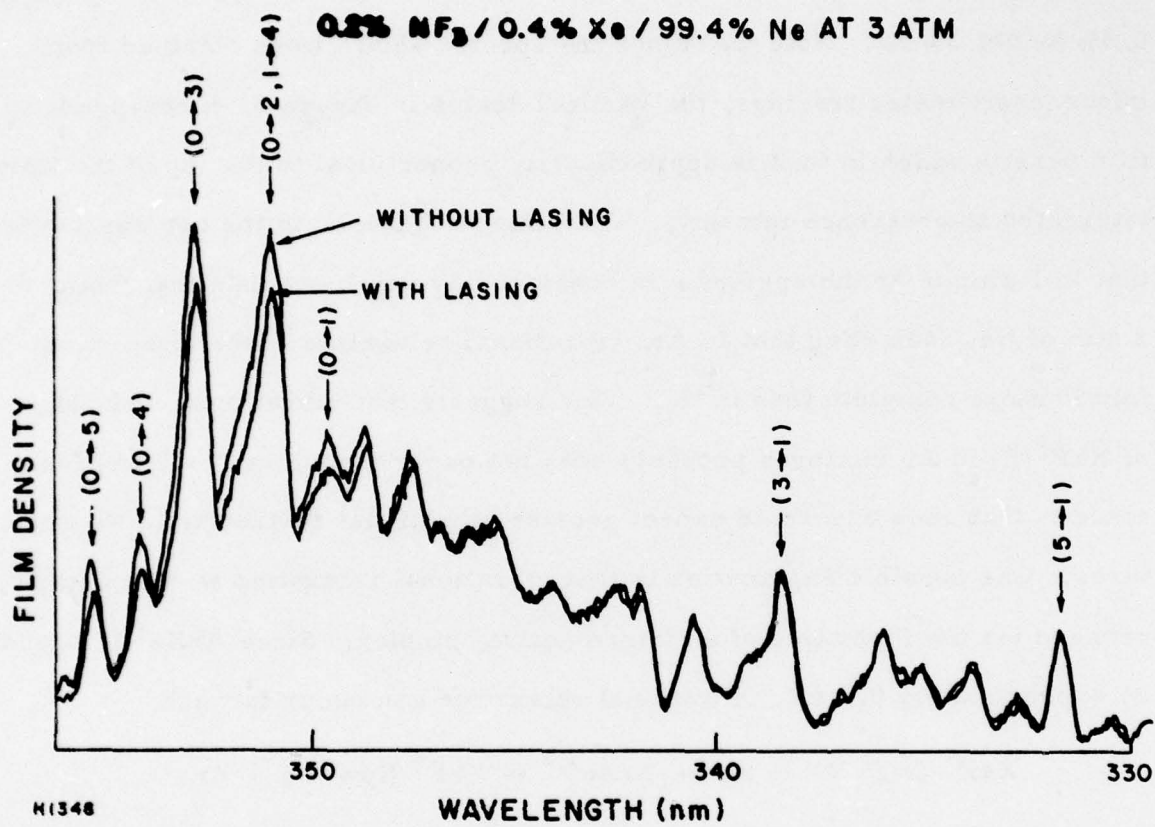
Figure 34   XeF* Sidelight Spectra with and without Lasing in
Ne/Xe/NF$_3$ Mixtures

82

V' = 0 while those from higher V' remained unchanged. This shows that the laser cavity flux only extracted efficiently from one vibrational level in the upper level manifold and that the vibrational relaxation time was larger than the lifetime of the upper laser levels so that there was no significant feeding of the V' = 0 level from higher V' levels during one lifetime.

Photodiode measurements also show the same behavior. Figure 35 shows signal traces from photodiodes looking at sidelight in the V' = 0 → V'' = 3 transition and at sidelight in the entire B → X band. Comparing signal intensities with and without lasing at 400 nsec into the pulse we have approximately

$$\frac{I_{0 \to 3} \text{ (Lasing)}}{I_{0 \to 3} \text{ (Non-Lasing)}} \approx 0.7$$

and

$$\frac{I_{B \to X} \text{ (Lasing)}}{I_{B \to X} \text{ (Non-Lasing)}} \approx 0.82$$

which again show the sidelight is not uniformly depressed over the B → X band. Quantitatively, one can estimate from these ratios, the fluorescence intensity from V' = 0 transition compared with fluorescence from the entire band. One can write

$$I_{B \to X} \text{ (Non-Lasing)} = I_{V' = 0} \text{ (Non-Lasing)} + I_{V' \neq 0} \text{ (Non-Lasing)}$$

$$I_{B \to X} \text{ (Lasing)} = I_{V' = 0} \text{ (Lasing)} + I_{V' \neq 0} \text{ (Lasing)}.$$

We have already shown that for V' ≠ 0 transitions the fluorescence intensity does not vary with the presence of a laser cavity flux so $I_{V' \neq 0}$ (Lasing) = $I_{V' \neq 0}$ (Non-Lasing). Solving the above equations and using the measured ratio, one gets

83

Ne DILUENT 2 ATM PRESSURE

LASING   NON—LASING

SIDELIGHT AT
3532 $\overset{o}{A}$
$(V' = 0 \rightarrow V'' = 3)$ ↓

SIDELIGHT OF
ENTIRE B→X   BAND ↑

TIME

200 nsec/div

$$\frac{\text{FLUORESCENCE FROM } V' = 0}{\text{FLUORESCENCE FROM ENTIRE BAND}} = 0.6$$
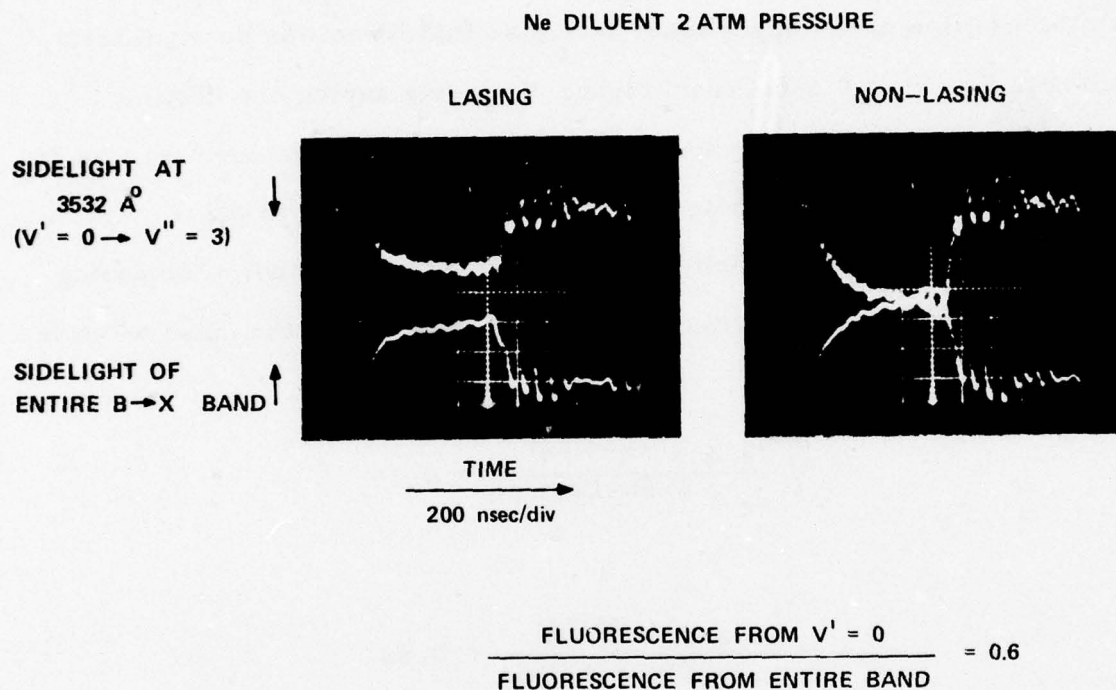
H1989

Figure 35   XeF[*] Sidelight Oscillograms

$$\frac{I_{V'=0} \ (\text{Non-Lasing})}{I_{B \to X} \ (\text{Non-Lasing})} \approx 0.6 .$$

If one assumes comparable quenching rates for all the different vibrational levels in the upper level manifold then this implies that the laser cavity flux was extracting only from 60% of the molecules formed in the $XeF^*(B)$ state.

Figure 36 shows similar spectra taken in an Ar mixture. Here because the vibrational relaxation is faster one does see sidelight depression in bands with $V' \neq 0$. This implies that when the population in the $V' = 0$ level is depressed by stimulated emission, molecules in the other V' levels feed into $V' = 0$ through vibrational relaxation so that the populations in the higher V' states get depressed as well.

Calculations based on photodiode measurements of sidelight in the $V' = 0 \to V'' = 3$ transition and in the entire $B \to X$ band in Ar show that greater than 90% of the molecules formed in the upper manifold are effectively reached by the laser cavity flux. Apparently in Ar, the reduction in laser efficiency, due to finite vibrational relaxation time in the upper manifold, is small. Despite this fact the observed laser efficiency using Ar is in general lower than that using Ne. This is because of higher medium absorption in Ar mixtures and low g_0 due to higher quenching rates results in a low extraction efficiency which more than offsets this advantage in vibrational relaxation.

Sidelight measurements also show evidence of bottlenecking. Figure 37 shows data taken in 3 atm of Ne diluted laser mixture. Also shown are laser output pulse shape and e-gun cathode current. First, since the laser output pulse lasted 1 μsec we conclude that the bottlenecking was not total.

85
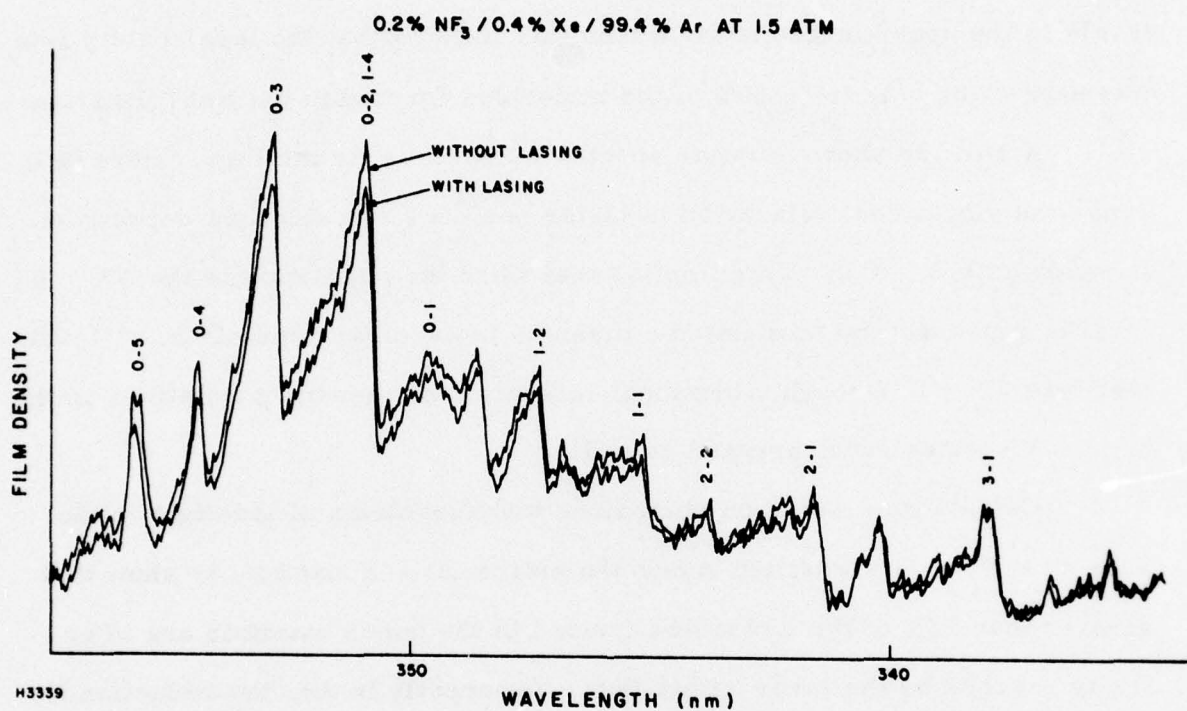
Figure 36   XeF* Sidelight Spectra with and without Lasing in
Ar/Xe/NF₃ Mixtures

86

NO LASING

LASING
CAVITY FLUX ≥ 10 × SATURATION FLUX

SIDELIGHT

$\lambda = 3532 \text{ Å}$
$V' = 0 \rightarrow V'' = 3$

LASER
PULSE
SHAPE

CATHODE
CURRENT

TIME
200 n sec/div

G9863-1
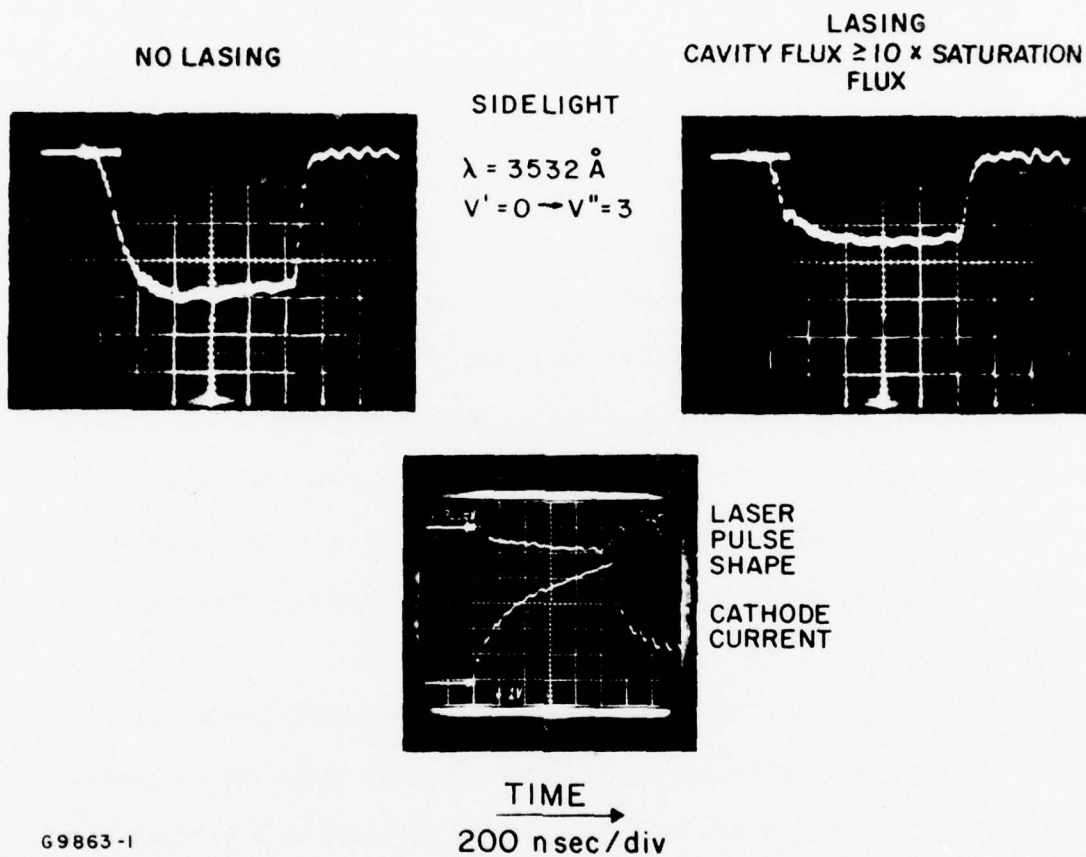
Figure 37   XeF* Sidelight Oscillograms Showing Evidence of Bottlenecking

87

That is deactivation of the $V'' = 3$ lower level must have occurred at a rate greater than the rate of upper level removal by spontaneous radiation and collisional quenching. Otherwise the laser would have shut off in a time equal to the lifetime of the upper level (< 10 nsec in this laser mixture). The data also shows that sidelight emission in the $V' = 0 \rightarrow V'' = 3$ transition decreased by a factor of 0.6 in going from nonlasing to lasing. The laser cavity flux calculated from measured laser output flux and mirror reflectivities was 10 times the saturation flux calculated from quenching rate constants given previously. Consequently, if bottlenecking is not a factor, one expects a factor of 11 decreases in sidelight emission from $XeF^*(V' = 0)$ states. A likely explanation for the observed data is that the lower state builds up to a population which depends on its rate of dissociation and vibrational mixing.

A buildup in population of the lower state seriously limits the extraction efficiency. This can be seen quantitatively if we write the extraction efficiency η_{ext} (laser photons out/upper states formed) as a product of two efficiencies. The first of these, η_s, is defined as the ratio of the number of upper states stimulated to the number of upper states formed. The remainder of the upper states formed are collisionally quenched or spontaneously radiated. The second of these efficiencies is then the ratio of laser photons out to the number of upper states stimulated. The remainder of the photons are absorbed in the laser medium or in the optical cavity.

η_s can be calculated by using the rate equation for the upper laser state. In Ne there is effectively no feeding of the $XeF^*(B, V' = 0)$ from other $XeF^*(B, V' \neq 0)$ states therefore we need only consider the rate equation for $V' = 0$, and write in steady-state

88

$$\frac{dN^*}{dt} = 0 = S_0 - \frac{\sigma_s \phi}{h\nu} (N^* - N) - \frac{N^*}{\tau_R} - \frac{N^*}{\tau_Q} \qquad (17)$$

Where

$N^* = XeF^* (B, V' = 0)$ density

$S_0 = XeF^* (B, V' = 0)$ production rate

σ_s = stimulated emission cross-section

$N = XeF (X, V'' = 3)$ density

ϕ = laser cavity flux

τ_R = radiative lifetime of $XeF^*(B)$

τ_Q = collisional quenching time of $XeF^*(B)$

Under fluorescence conditions when $\phi = 0$ we have

$$S_0 = N_0^* \left(\frac{1}{\tau_R} + \frac{1}{\tau_Q}\right) = \frac{N_0^*}{\tau_E} \qquad (18)$$

Where N_0^* denotes N^* when $\phi = 0$ and τ_E is the lifetime of $XeF^*(B, V' = 0)$. In steady-state, η_s as defined above is simply the stimulated rate over the production rate,

$$\eta_s = \frac{\sigma_s \phi (N^* - N)}{h\nu S_0}$$

Now using Eq. (8) and $\phi_s = \frac{h\nu}{\sigma_s \tau_E}$ we have

$$\eta_s = \phi_s \left(\frac{N^*}{N_o^*} - \frac{N}{N_0^*}\right) \qquad (19)$$

If Eq. (17) is solved for $\frac{N}{N_0^*}$ in terms of $\frac{\phi}{\phi_s}$ and $\frac{N^*}{N_0^*}$, and the result inserted into Eq. (19), the following simple equation results.

$$\eta_s = 1 - \frac{N^*}{N_0^*}$$

89

Now the sidelight intensity, I, in the $V' = 0 \to V'' = 3$ line is proportional to N^* therefore η_s can be written in terms of measured quantities as

$$\eta_s = 1 - \frac{I_{0 \to 3}(\phi)}{I_{0 \to 3}(0)} .$$

For the case shown in Figure 37 we have $\eta_s \approx 0.4$.

Taking into account laser medium absorption, it can be shown[18] that at optimum output coupling the extraction efficiency is given by

$$\eta_{ext} = \eta \, \eta_s \, (\phi \gg \phi_s)$$

Where η is the extraction efficiency assuming zero lower state lifetime (see Figure 7 of the previous semi-annual report)[1] and $\eta_s (\phi \gg \phi_s)$ is η_s at cavity flux, much greater than ϕ_s.

The intrinsic laser efficiency taking into account the lack of vibrational equilibration and finite lower level lifetime can now be calculated. For Ne with unity channeling to $XeF^*(B)$ but only 60% of those formed are available for extraction (the balance are in higher vibrational levels), the effective formation efficiency η_f, into $XeF^*(B, V' = 0)$ is then 8.4%. At 4 atm total pressure, 10 A/cm^2 e-beam excitation, and a medium absorption coefficient of $3 \times 10^{-3} \, cm^{-1}$, η is approximately 0.65. The measured sidelight intensity ratio with $\phi = 0$ to $\phi \approx 30 \, \phi_{sat}$ is 0.5 at 4 atm. Therefore $N_s = 0.5$. The laser intrinsic efficiency is then

$$N_{int} = \eta_f \, \eta \, \eta_s = 2.7\% .$$

This agrees very well with the measured value of 2.6%.

D. LOWER LEVEL DEACTIVATION

If the process of bottlenecking, proposed in the previous section to explain the sidelight data, is correct, then the lower level XeF (x, v'' = 3)

(18) Rokni, M. and Jacob, J., Private Communication.

90

deactivation time can be deduced from the measured quantities. The deactivation time τ_D for the processes

$$XeF(x, v'' = 3) \overset{\tau_D}{\to} XeF(x, v'' \neq 3)$$

and

$$\to Xe + F$$
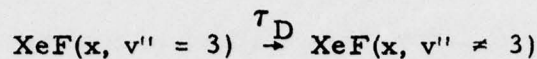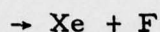
in Ne mixtures is given by (see Appendix A)

$$\tau_D = T_E \frac{\left[\frac{N^*}{N_0^*} (1 + \frac{\phi}{\phi_s}) - 1 \right]}{\frac{\phi}{\phi_s} (1 - \frac{T_E}{\tau_Q} \frac{N^*}{N_0^*})} \tag{20}$$

τ_E, τ_Q and ϕ_s, defined previously, can be calculated from measured values of quenching rate constants, stimulated emission cross section and radiative lifetime. N^*/N_0^* is just given by the ratio of the sidelight intensities in the $v'' = 0 \to v'' = 3$ line. ϕ can be determined by measuring the laser output flux and relating it to ϕ, the laser cavity flux, through known output coupling.

This was done using sidelight data from experiments 1, 2, 3 and 4 atm Ne diluted mixtures. The deactivation time calculated from the experimental data is summarized in Table 8. The approximate 1/pressure dependence indicated by these deactivation times is consistent with collisional deactivation through vibrational mixing and collisional dissociation processes,

$$XeF(x, v'' = 3) + Ne \to XeF(x, v'' \neq 3) \quad \text{or} \to Xe + F + Ne .$$
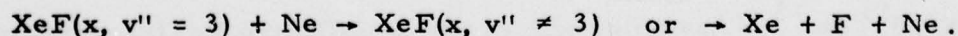
The rates for these processes are not sufficiently high so that the buildup of the lower state population reduces the intrinsic laser efficiency by as much as a factor of 2.

Since XeF(x) is slightly bound, even at thermal equilibrium, there will be a finite density of this species. To see if this can be a factor in limiting the laser efficiency, the equilibrium constant for the reaction

$$XeF(x) \rightleftarrows Xe + F$$
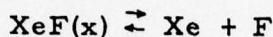
has been calculated by V. Shui[19] from XeF spectroscopic data obtained by Smith and Kobrinsky.[17] A plot of the equilibrium constant versus temperature is shown in Figure 38. Details of the calculational procedure are presented in Appendix B.

The XeF ground state population at thermal equilibrium can be calculated from this constant if the densities of Xe and F ar known. Typical laser mixtures contain 0.5% Xe, consequently at 4 atm, $N_{Xe} = 5 \times 10^{17}$ cm^{-3}. The F atom density increases with time during the excitation pulse since the three body recombination rate

$$F + F + M \rightarrow F_2 + M$$
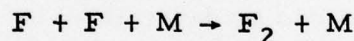
is small ($K \approx 10^{-32}$ cm^6/sec) and no significant recombination occurs during the pulse. At the end of a one μsec pulse with a typical pump power density of 5×10^{22} electron-ion pairs/cm^3/sec. $N_F \approx 5 \times 10^{16}$/$cm^3$; that is, one F atom is eventually produced for every electron-ion pair generated. The product of N_F and N_{Xe} is therefore 2.5×10^{34} cm^{-6}. Using the equilibrium constant for 300^OK we get an upper bound on the equilibrium XeF(x) density of 3.4×10^{13} cm^{-3}. Assuming vibrational equilibrium XeF(x) vibrational levels at 300^OK, the XeF(x, $v'' = 3$) population is then 1.56×10^{12} cm^{-3}.

To see if this XeF(x, $v'' = 3$) density significantly affects extraction efficiency we compare it to the upper level density N^* under lasing conditions.

(19) Shui, V. (Private Communication).

92
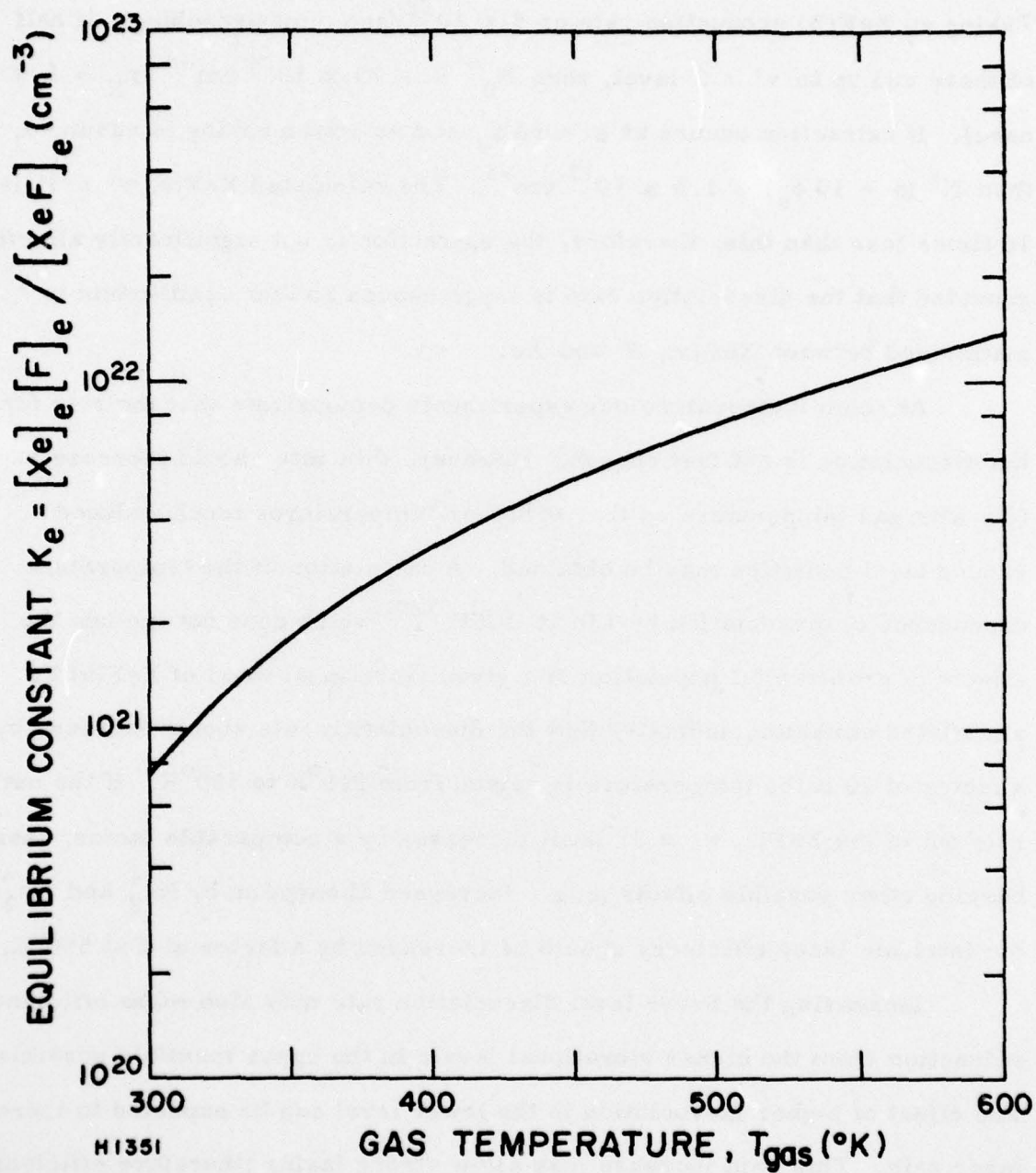
Figure 38   XeF $\rightleftarrows$ Yet F Equilibrium Constant as a Function
of Gas Temperature

Taking an XeF(B) production rate of 5×10^{22}/sec (unit branching), if half of these end up in $v' = 0$ level, then $N_0^* \approx 1.75 \times 10^{14}$ cm^{-3} ($\tau_E = 6.9$ nsec). If extraction occurs at $\phi = 10\,\phi_s$ and no bottlenecking is assumed, then $N^* (\phi = 10\,\phi_s) = 1.6 \times 10^{13}$ cm^{-3}. The calculated XeF(x, $v'' = 3$) is 10 times less than this, therefore, the extraction is not significantly affected provided that the dissociation rate is large enough so that equilibrium is maintained between XeF(x), F and Xe.

At room temperature our experiments demonstrate that the rate for the dissociation is not fast enough. However, this rate should increase rapidly with gas temperature so that at higher temperatures much reduced ground level densities may be obtained. A calculation of the temperature dependence of dissociation by Lin at UCSD, [20] which does not include the effects of preferential population of a given vibrational level of XeF(x) by stimulated emission, indicates that the dissociation rate should increase by a factor of 20 if the temperature is raised from 300°K to 550°K. If the net rate out of the XeF(x, $v'' = 3$) level increases by a comparable factor, then barring other possible effects (e.g., increased absorption by Ne$_2^+$ and Xe$_2^+$) the intrinsic laser efficiency should be increased by a factor of 2 at 550°K.

Increasing the lower level dissociation rate may also make efficient extraction from the higher vibrational levels in the upper manifold possible. The effect of higher dissociation in the lower level can be expected to increase laser gain. This gain increase may allow strong lasing (therefore efficient extraction) on lines that at room temperature are just barely over or even under laser threshold. In particular, if strong lasing occurs in the 3511 Å transition, then the $v' = 1$ level will be effectively stimulated. Also, at

(20)   Lin, S. C. (Private Communication).

94

room temperature, when very low output coupling optical cavity is used, weak lasing has been observed in the line at 3487 Å, indicating low but positive gain in that line. The band centered around 3487 Å has been identified as a blend of $0 \to 1$, $1 \to 3$ and $2 \to 5$ transitions. If strong lasing can be obtained in this line when hot then we can expect also efficient extraction from the v' = 2 level. In this case the fraction of the upper manifold available to stimulated emission will be greater than 95%.

E. SUMMARY OF MAJOR XeF* RESULTS

The major results on e-beam pumping of XeF* laser systems obtained in this reporting period are summarized as follows:

(1) The formation of the upper laser state, XeF*, from e-beam ionization is shown to proceed with essentially unit branching in both Ar and Ne rich mixtures. This implies maximum formation efficiencies of 17% in Ar mixtures and 14% in Ne mixtures.

(2) The rate constants for two body and three body quenching of XeF* by Xe, Ar and Ne have been measured. These allow the calculation of the saturation flux in typical Ar and Ne diluted mixtures.

(3) A formation chain for XeF* in Ne rich mixtures is proposed and kinetics calculations based on this chain agree with all the experimental observations.

(4) Medium photoabsorption at the laser wavelength has been measured in mixtures of $Ar/F_2/Xe$. Ar_2^+ and Xe_2^+ are identified as the dominant absorbing species. The estimated absorption cross sections based on these measurements are 1.7×10^{-17} cm^2 for Ar_2^+ and 1.3×10^{-16} cm^2 for Xe_2^+.

(5) Medium absorption in mixtures of $Ne/F_2/Xe$ have been measured. An upper bound on the Ne_2^+ photoabsorption cross section of 2×10^{-17} cm^2 is obtained.

(6) Higher laser efficiencies obtained in Ne mixtures compared with Ar mixtures are shown to be a consequence of much lower laser medium absorption and lower quenching of the upper laser level.

(7) 36 J of output energy was obtained from 4.5 ℓ of active laser volume (8 J/ℓ) with an intrinsic laser efficiency of 2.6% in 4 atm of $Ne/Xe/NF_3$ mixture.

(8) Vibrational relaxation of the upper level $(XeF^*(B))$ manifold is shown to be faster in Ar mixtures than in Ne mixtures. This is attributed to the formation of an intermediate complex, $ArXeF^*$, in Ar mixtures.

(9) The laser intrinsic efficiency is shown to be adversely affected by the lack of vibrational relaxation in the $XeF^*(B)$ manifold and by finite lifetime of the $XeF(x)$ lower laser level.

(10) Inclusion of these effects in laser efficiency calculations lead to calculated efficiencies very close to those actually observed.

(11) The rate constant for the deactivation of the lower level via

$$XeF(v'' = 3) + Ne \rightarrow XeF(v'' \neq 3) + Ne \rightarrow Xe + F + Ne$$
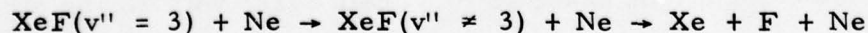
is estimated to be 3×10^{-12} cm^3/sec.

(12) Methods of improving XeF^* laser efficiency are identified.

96

REFERENCES

1. Hsia, J. C. , Jacob, J. H. Mangano, J. A. and Rokni, M. , "One Meter KrF Laser System", Semi-Annual Report, 23 August 1976 to 22 February 1977.

2. Chen, C. H. , Judish, J. P. , and Payne, M. G. , "Energy Transfer Processes in Ar-Xe and Ar-F_2 Mixtures" (Unpublished).

3. Brau, C. A. , and Ewing, J. J. , J. Chem. Phys. , 63, 4640 (1975).

4. Daugherty, J. D. , Mangano, J. A. , and Jacob, J. H. , Appl. Phys. Lett. 28, 581 (1976).

5. Parker, R. K. , Anderson, R. E. , and Duncan, C. V. , J. Appl. Phys. , 45, 2463 (1974).

6. Rokni, et al. , Appl. Phys. Lett. 30, 458 (1977).

7. Brashears, H. C. , Setser, D. W. , and Des Marteau (Unpublished).

8. Rokni, M. (Unpublished).

9. Eden, G. J. and Searles, S. K. (Unpublished).

10. Champagne, L. F. , et al. , presented at the 7th Winter Colloquium on High Power Visible Lasers.

11. Mangano, J. A. , Hsia, J. , and Hawryluk, A. M. (Unpublished).

12. Rokni, M. and Jacob, J. (Unpublished).

13. Rokni, M. et al. (to be published in Appl. Phys. Lett.)

14. Jesse, W. P. and Sadauskis, J. , Phy. Rev. 88, 417L (1952).

15. Wadt, W. (to be published).

16. Tellinghuisen, J. , et al. , "Analysis of Spontaneous and Laser Emission from XeF" (to be published).

17. Smith, A. L. , and Kobrinsky, P. C. (to be published).

18. Rokni, M. and Jacob, J. , (Private Communication).

19. Shui, V. (Private Communication).

20. Lin, S. C. (Private Communication).

APPENDIX A

CALCULATION OF XeF (X, v) DEACTIVATION RATE
FROM SIDELIGHT FLUORESCENCE DATA

In lasers having a non negligible lower state population, both the upper and lower state populations must be determined if the laser power extraction efficiency is to be calculated. These populations under lasing conditions depend on the deactivation rate of the lower laser level. In this appendix a formula for calculating this rate in the XeF laser is developed in terms of quantities which can be calculated and/or measured.

The equations which describe the production and loss of the upper and lower states in the XeF laser in steady state are given by

$$\frac{dN^*}{dt} = \frac{N_o^*}{\tau_E} - \frac{\sigma_s}{h\nu} (N^* - N)\phi - \frac{N^*}{\tau_R} - \frac{N^*}{\tau_Q} = 0 \qquad (A-1)$$

and

$$\frac{dN}{dt} = \frac{\sigma_s}{h\nu} (N^* - N)\phi - \frac{N}{\tau_D} + \frac{N^*}{\tau_R} = 0 \qquad (A-2)$$

where

$\quad N^* \quad = \quad XeF^* (B, v')$ density

$\quad N_o^* \quad = \quad XeF (B, v')$ density when $\phi = 0$

$\quad N \quad = \quad XeF (X, v'')$ density

$\quad \sigma_s \quad = \quad$ stimulated emission cross section

$\quad \tau_R \quad = \quad$ radiative lifetime

$\quad \tau_Q \quad = \quad$ collisional quenching time

99

$$\tau_E = \tau_R \tau_Q / (\tau_Q + \tau_R)$$

$$\tau_D = \text{XeF} (X, v'') \text{ deactivation time}$$

$$\phi = \text{laser cavity flux}$$

If Eqs. (A-1) and (A-2) are added, the following equation is obtained after some rearranging

$$N = \frac{\tau_D}{\tau_E} N_o^* - \frac{\tau_D}{\tau_Q} N^* \tag{A-3}$$

Substituting Eq. (A-3) into Eq. (A-1), an equation results which can be solved for τ_D in terms of ϕ / ϕ_c, N^* / N_o^*, τ_Q and τ_R.

$$\tau_D(X, v) = \tau_E \frac{\left[\frac{N^*}{N_o^*} \left(1 + \frac{\phi}{\phi_c} \right) - 1 \right]}{\frac{\phi}{\phi_c} \left(1 - \frac{\tau_E}{\tau_Q} \frac{N^*}{N_o^*} \right)} \tag{A-4}$$

where

$$\phi_c = \frac{h\nu}{\sigma_s \tau_E} .$$

APPENDIX B

EQUILIBRIUM NUMBER DENSITIES: $XeF \rightleftarrows Xe + F$

As a general rule we note that it has been well established both theoretically and experimentally that, over a wide range of pressures of practical interest, equilibrium dissociation of diatomic molecules is nearly complete when the temperature exceeds a few percent of the dissociation energy.

When more specific answers are needed, equilibrium number densities of molecules and atoms can be calculated by using statistical mechanics equations which are well documented in the literature.[1] For practical applications, various approximations have also been developed. In particular, the Morse-potential approximation has been used successfully[2] and has been adopted here to generate the results shown below. The spectroscopic data used in the present calculations are mostly those reported by Smith and Kobrinsky.[3]

At equilibrium the number densities are related by the equation

$$[XeF]_e = [Xe]_e [F]_e / Ke, \qquad (B-1)$$

where the subscript e denotes equilibrium values and K_e is the equilibrium constant which can be calculated from statistical mechanics Eqs.[1,2] and spectroscopic data.[3]

Furthermore the equilibrium number density of a particular vibrational state of the molecule can also be estimated from the equation

$$\frac{[XeF(v)]_e}{[XeF]_e} = \frac{Q_v(v)}{Q_v} \qquad (B-2)$$

where $Q_v(v)$ is the vibrational partition function for level v and Q_v is the total vibrational partition function.[1] Results for XeF and XeF ($v'' = 2$) are plotted in Figs. B-1 through B-3.
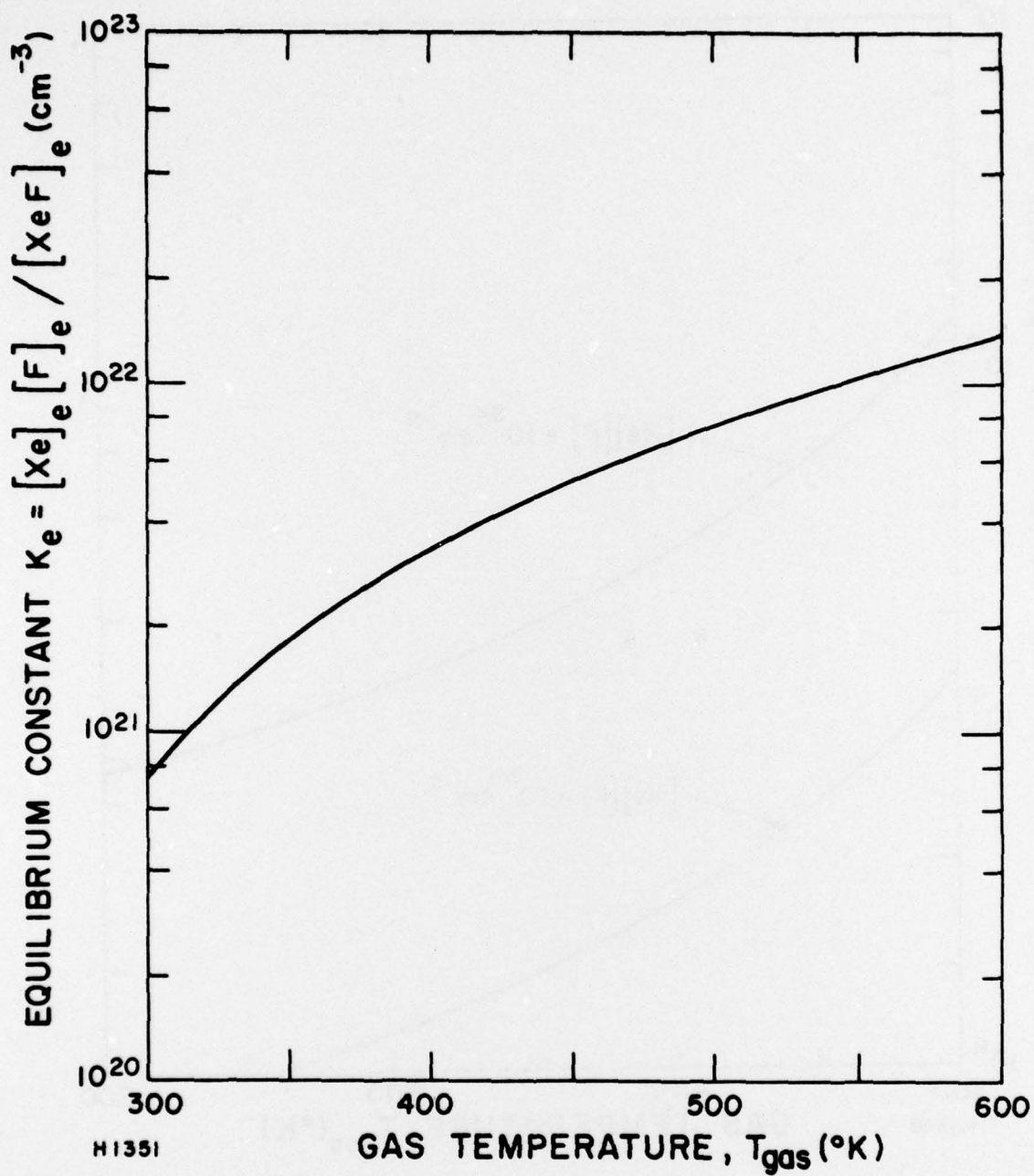
Fig. B-1   Equilibrium Constant for Xe + F $\rightleftarrows$ XeF vs Temperature

103
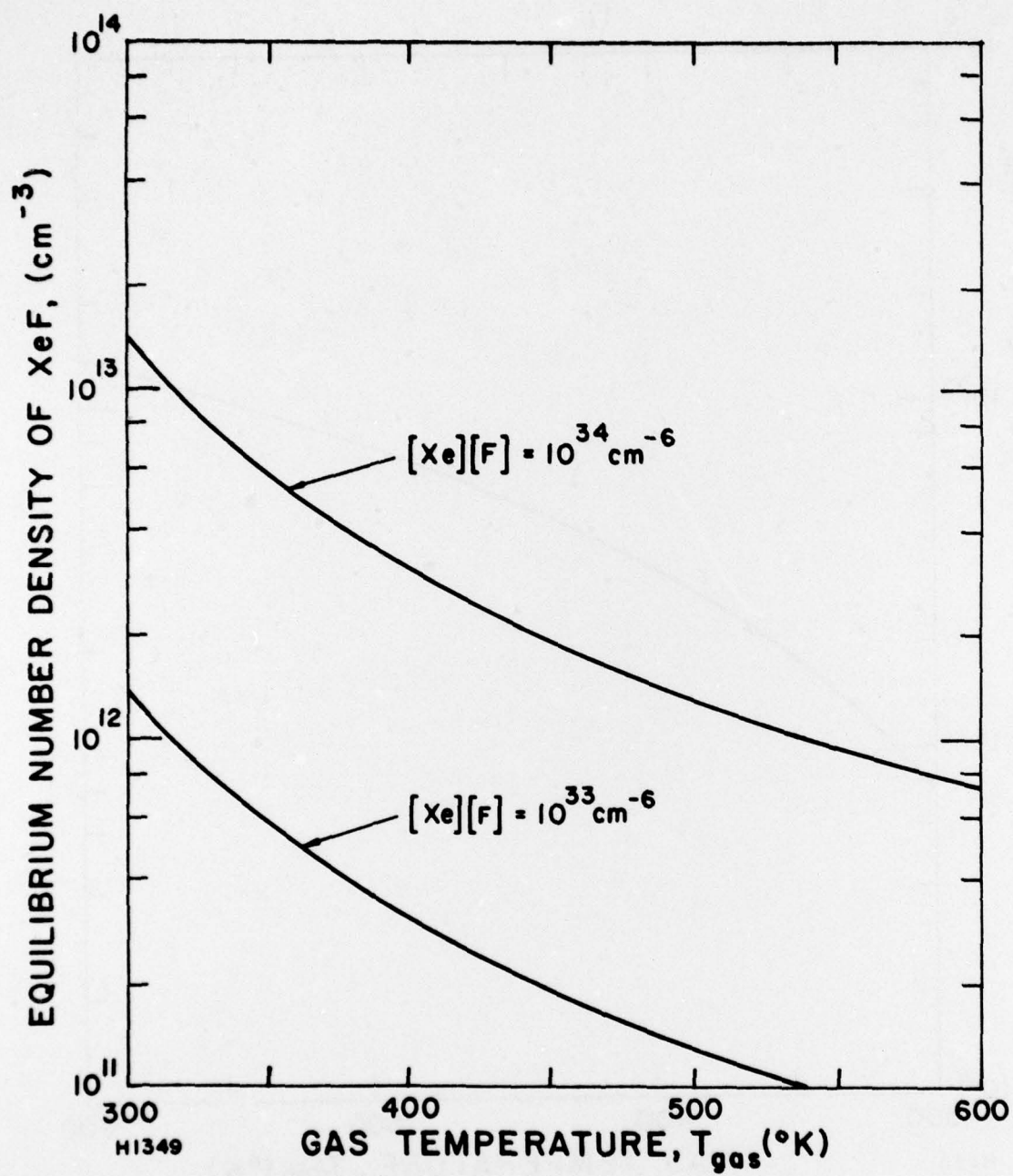
Fig. B-2   Equilibrium XeF Density vs Temperature

104

EQUILIBRIUM NUMBER DENSITY OF XeF (v = 3) (cm^{-3})

10^{13}

10^{12}

10^{11}

10^{10}

$[Xe][F] = 10^{34}$ cm^{-6}

$[Xe][F] = 10^{33}$ cm^{-6}

300   400   500   600

H1350   GAS TEMPERATURE, T_{gas} (°K)
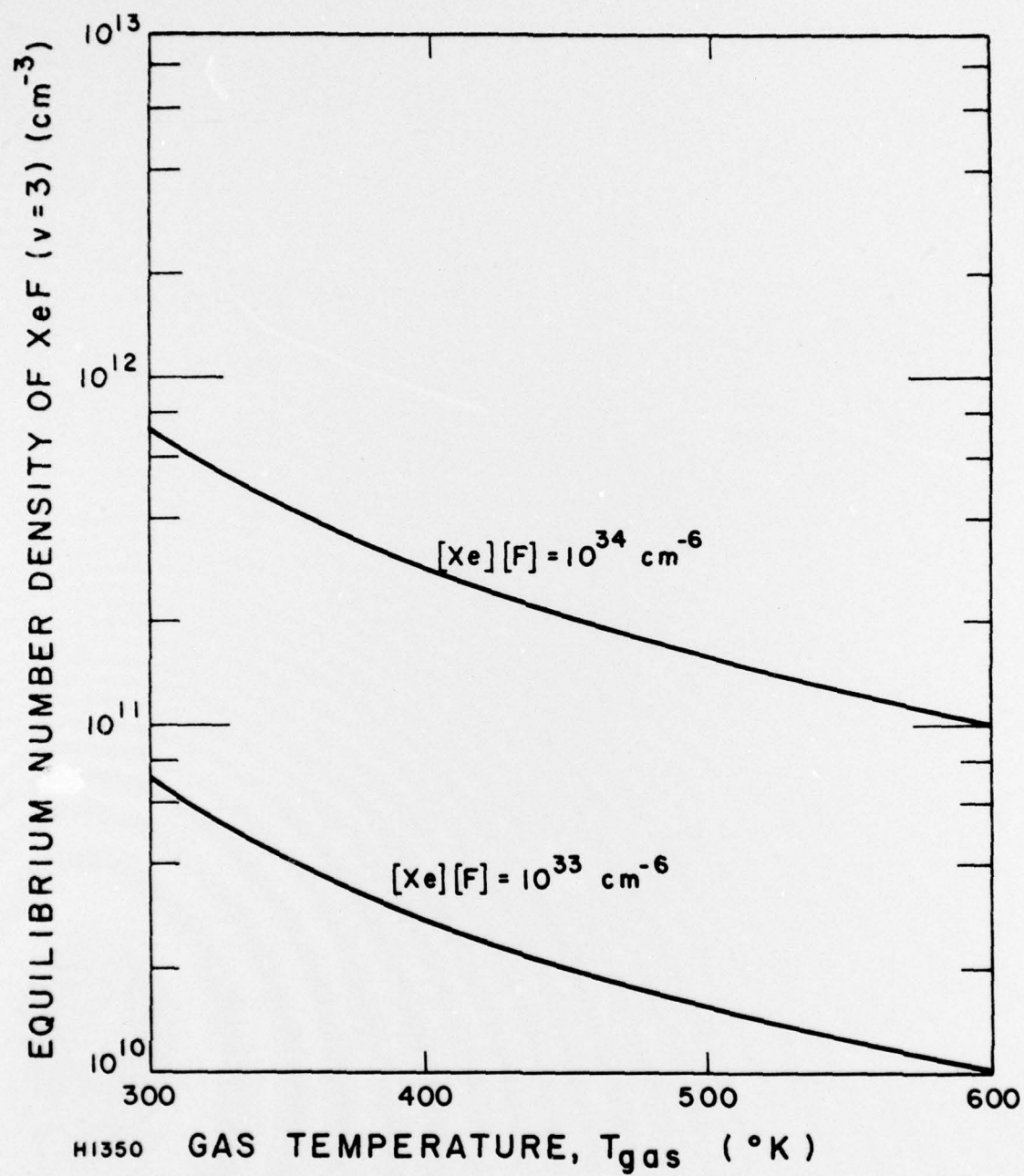
Fig. B-3   Equilibrium XeF (V = 3) Density vs Temperature

105

APPENDIX B

REFERENCES

1. For example: O.K. Rice, <u>Statistical Mechanics, Thermodynamics and Kinetics</u>, Freeman, San Francisco, 1967; <u>JANAF Thermodynamic Tables</u>, Second Editions, USNBS, NSRDS-37 (1970).

2. For example: J.C. Keck and G.F. Carrier, "Diffusion Theory of Nonequilibrium Dissociation and Recombination," J. Chem. Phys. $\underline{43}$, 2284 (1965); V.H. Shui, J.P. Appleton and J.C. Keck, "The Three-Body Recombination and Dissociation of Diatomic Molecules," Symposium Combustion $\underline{13}$, 21 (1971).

3. A.L. Smith and P.C. Kobrinsky, "Flash Photolysis Absorption Spectroscopy of Xenon Fluoride: Vibrational Analysis of the B-X Transition," to be published.

DISTRIBUTION LIST

Office of Naval Research, Department of the Navy, Arlington, VA 22217 - Attn: Physics Program (3 copies)

Naval Research Laboratory, Department of the Navy, Washington, D.C. 20375 - Attn: Technical Library (1 copy)

Office of the Director of Defense, Research and Engineering, Information Office Library Branch, The Pentagon, Washington, D.C. 20301 (1 copy)

U.S. Army Research Office, Box CM, Duke Station, Durham, N.C. 27706 (1 copy)

Defense Documentation Center, Cameron Station, Alexandria, VA 22314 (12 copies)

Defender Information Analysis Center, Battelle Memorial Institute, 505 King Avenue, Columbus, OH 43201 (1 copy)

Commanding Officer, Office of Naval Research Branch Office, 536 South Clark Street, Chicago, IL 60615 (1 copy)

New York Area Office, Office of Naval Research, 715 Broadway (5th Floor), New York, NY 10003 - Attn: Dr. Irving Rowe (1 copy)

San Francisco Area Office, Office of Naval Research, 760 Market Street, Room 447, San Francisco, CA 94102 (1 copy)

Air Force Office of Scientific Research, Department of the Air Force, Washington, D.C. 22209 (1 copy)

Office of Naval Research Branch Office, 1030 East Green Street, Pasadena, CA 91106 - Attn: Dr. Robert Behringer (1 copy)

Code 102 IP (ONRL), Office of Naval Research, 800 N. Quincy Street, Arlington, VA 22217 (6 copies)

Defense Advanced Research Projects Agency, 1400 Wilson Blvd., Arlington, VA 22209 - Attn: Strategic Technology Office (1 copy)

Office Director of Defense, Research & Engineering, The Pentagon, Washington, D.C. 20301 - Attn: Assistant Director (Space and Advanced Systems) (1 copy)

Office of the Assistant Secretary of Defense, System Analysis (Strategic Programs), Washington, D.C. 20301 - Attn: Mr. Gerald R. McNichols (1 copy)

U.S. Arms Control and Disarmament Agency, Dept. of State Bldg., Rm. 4931, Washington, D.C. 20451 - Attn: Dr. Charles Henkin (1 copy)

Energy Research Development Agency, Division of Military Applications, Washington, D.C. 20545 (1 copy)

National Aeronautics and Space Administration, Lewis Research Center, Cleveland, OH 44135 - Attn: Dr. John W. Dunning, Jr. (1 copy)
                                                                                        (Aerospace Res. Engineer)

National Aeronautics & Space Administration, Code RR, FOB 10B, 600 Independence Ave., SW, Washington, D.C. 20546 (1 copy)

National Aeronautics and Space Administration, Ames Research Center, Moffett Field, CA 94035 - Attn: Dr. Kenneth W. Billman (1 copy)

Department of the Army, Office of the Chief of RD&A, Washington, D.C. 20310 - Attn: DARD-DD (1 copy)
                                                                                      DAMA-WSM-T (1 copy)

Department of the Army, Office of the Deputy Chief of Staff for Operations & Plans, Washington, D.C. 20310 - Attn: DAMO-RQD - (1 copy)

Ballistic Missile Defense Program Office (BMDPO), The Commonwealth Building, 1300 Wilson Blvd., Arlington, VA 22209 - Attn: Mr. Albert J. Bast, Jr.
                                                                                                                    (1 copy)

U.S. Army Missile Command, Research & Development Division, Redstone Arsenal, AL 35809 - Attn: Army High Energy Laser Programs (2 copies)

Commander, Rock Island Arsenal, Rock Island, IL 61201, Attn: SARRI-LR, Mr. J.W. McGarvey (1 copy)

Commanding Officer, U.S. Army Mobility Equipment R&D Center, Ft. Belvoir, VA 22060 - Attn: SMEFB-MW (1 copy)

Commander, U.S. Army Armament Command, Rock Island, IL 61201 - Attn: AMSAR-RDT (1 copy)

Director, Ballistic Missile Defense Advanced Technology Center, P.O. Box 1500, Huntsville AL 35807 - Attn: ATC-O (1 copy)
                                                                                                        ACT-T (1 copy)

Commander, U.S. Army Material Command, Alexandria, VA 22304 - Attn: Mr. Paul Chernoff (AMCRD-T) (1 copy)

Commanding General, U.S. Army Munitions Command, Dover, NH 17801 - Attn: Mr. Gilbert F. Chesnov (AMSMU-R) (1 copy)

Director, U.S. Army Ballistics Res. Lab, Aberdeen Proving Ground, MD 21005 - Attn: Dr. Robert Eichenberger (1 copy)

Commandant, U.S. Army, Air Defense School, Ft. Bliss, TX 79916 - Attn: Air Defense Agency (1 copy)
                                                                        ATSA-CTD-MS (1 copy)

Commanding General, U.S. Army Combat Dev. Command, Ft. Belvoir, VA 22060 - Attn: Director of Material, Missile Div. (1 copy)

Commander, U.S. Army Training & Doctrine Command, Ft. Monroe, VA 23651 - Attn: ATCD-CF (1 copy)

Commander, U.S. Army Frankford Arsenal, Philadelphia, PA 19137 - Attn: Mr. M. Elnick SARFA-FCD Bldg. 201-3 (1 copy)

Commander, U.S. Army Electronics Command, Ft. Monmouth, NJ 07703 - Attn: AMSEL-CT-L, Dr. R.G. Buser (1 copy)

Commander, U.S. Army Combined Arms Combat Developments Activity, Ft. Leavenworth, KS 66027 (1 copy)

National Security Agency, Ft. Geo. G. Meade, MD 20755 - Attn: R.C. Foss A763 (1 copy)

Deputy Commandant for Combat & Training Developments, U.S. Army Ordnance Center and School, Aberdeen Proving Ground, MD 21005
Attn: ATSL-CTD-MS-R (1 copy)

Commanding Officer, USACDC CBR Agency, Ft. McClellan, AL 36201 - Attn: CDCCBR-MR (Mr. F.D. Poer) (1 copy)

Department of the Navy, Office of the Chief of Naval Operations, The Pentagon 5C739, Washington, D.C. 20350 - Attn: (OP 982F3) (1 copy)

Office of Naval Research Branch Office, 495 Summer Street, Boston, MA 02210 - Attn: Dr. Fred Quelle (1 copy)

Department of the Navy, Deputy Chief of Navy Material (Dev.), Washington, D.C. 20360 - Attn: Mr. R. Gaylord (MAT 032B) (1 copy)

Naval Missile Center, Point Mugu, CA 93042 - Attn: Gary Gibbs (Code 5352) (1 copy)

Naval Research Laboratory, Washington, D.C. 20375 - Attn: (Code 5503-EOTPO) (1 copy)
Dr. P. Livingston - Code 5560 (1 copy)
Dr. A. I. Schindler - Code 6000 (1 copy)
Dr. H. Shenker - Code 5504 (1 copy)
Mr. D.J. McLaughlin - Code 5560 (1 copy)
Dr. John L. Walsh - Code 5503 (1 copy)

High Energy Laser Project Office, Department of the Navy, Naval Sea Systems Command, Washington, D.C. 20360 - Attn: Capt. A. Skolnick, USN (PM 22) (1 copy)

Superintendent, Naval Postgraduate School, Monterey, CA 93940 - Attn: Library (Code 2124) (1 copy)

Navy Radiation Technology, Air Force Weapons Lab (NLO), Kirtland AFB, NM 87117 (1 copy)

Naval Surface Weapons Center, White Oak, Silver Spring, MD 20910 - Attn: Dr. Leon H. Schindel (Code 310) (1 copy)
Dr. E. Leroy Harris (Code 313) (1 copy)
Mr. K. Enkenhaus (Code 034) (1 copy)
Mr. J. Wise (Code 047) (1 copy)
Technical Library (1 copy)

U.S. Naval Weapons Center, China Lake, CA 93555 - Atn: Technical Library (1 copy)

HQ USAF (AF/RDPS), The Pentagon, Washington, D.C. 20330 - Attn: Lt. Col. A.J. Chiota (1 copy)

HQ AFSC/XRLW, Andrews AFB, Washington, D.C. 20331 - Attn: Maj. J.M. Walton (1 copy)

HQ AFSC (DLCAW), Andrews AFB, Washington, D.C. 20331 - Attn: Maj. H. Axelrod (1 copy)

Air Force Weapons Laboratory, Kirtland AFB, NM 87117 - Attn: LR (1 copy)
AL (1 copy)

HQ SAMSO (XRTD), P.O. Box 92960, Worldway Postal Center, Los Angeles, CA 90009 - Attn: Lt. Dorian DeMaio (XRTD) (1 copy)

AF Avionics Lab (TEO), Wright Patterson AFB, OH 45433 - Attn: Mr. K. Hutchinson (1 copy)

Dept. of the Air Force, Air Force Materials Lab. (AFSC), Wright Patterson AFB, OH 45433 - Attn: Maj. Paul Elder (LPS) (1 copy)
Laser Window Group

HQ Aeronautical Systems Div., Wright Patterson AFB, OH 45433 - Attn: XRF - Mr. Clifford Fawcett (1 copy)

Rome Air Development Command, Griffiss AFB, Rome, NY 13440 - Attn: Mr. R. Urtz (OCSE) (1 copy)

HQ Electronics Systems Div. (ESL), L.G. Hanscom Field, Bedford, MA 01730 - Attn: Mr. Alfred E. Anderson (XRT) (1 copy)
Technical Library (1 copy)

Air Force Rocket Propulsion Lab., Edwards AFB, CA 93523 - Attn: B.R. Bornhorst, (LKCG) (1 copy)

Air Force Aero Propulsion Lab., Wright Patterson AFB, OH 45433 - Attn: Col. Walter Moe (CC) (1 copy)

Dept. of the Air Force, Foreign Technology Division, Wright Patterson AFB, OH 45433 - Attn: PDTN (1 copy)

Commandant of the Marine Corps, Scientific Advisor (Code RD-1), Washington, D.C. 20380 (1 copy)

Aerospace Research Labs., (AP), Wright Patterson AFB, OH 45433 - Attn: Lt. Col. Max Duggins (1 copy)

Defense Intelligence Agency, Washington, D.C. 20301 - Attn: Mr. Seymour Berler (DTIB) (1 copy)

Central Intelligence Agency, Washington, D.C. 20505 - Attn: Mr. Julian C. Nall (1 copy)

Analytic Services, Inc., 5613 Leesburg Pike, Falls Church, VA 22041 - Attn: Dr. John Davis (1 copy)

Aerospace Corp., P.O. Box 92957, Los Angeles, CA 90009 - Attn: Dr. G.P. Millburn (1 copy)

Airesearch Manuf. Co., 9851-9951 Sepulveda Blvd., Los Angeles, CA 90009 - Attn: Mr. A. Colin Stancliffe (1 copy)

Atlantic Research Corp., Shirley Highway at Edsall Road, Alexandria, VA 22314 - Attn: Mr. Robert Naismith (1 copy)

Avco Everett Research Lab., 2385 Revere Beach Parkway, Everett, MA 02149 - Attn: Dr. George Sutton (1 copy)
Dr. Jack Daugherty (1 copy)

Battelle Columbus Laboratories, 505 King Avenue, Columbus, OH 43201 - Attn: Mr. Fred Tietzel (STPIAC) (1 copy)

Bell Aerospace Co., Buffalo, NY 14240 - Attn: Dr. Wayne C. Solomon (1 copy)

Boeing Company, P.O. Box 3999, Seattle, WA 98124 - Attn: Mr. M.I. Gamble (2-, 460, MS 8C-88) (1 copy)

Electro-Optical Systems, 300 N. Halstead, Pasadena, CA 91107 - Attn: Dr. Andrew Jensen (1 copy)

ESL, Inc., 495 Java Drive, Sunnyvale, CA 94086 - Attn: Arthur Einhorn (1 copy)

General Electric Co., Space Division, P.O. Box 8555, Philadelphia, PA 19101 - Attn: Dr. R.R. Sigismonti (1 copy)

General Electric Co., 100 Plastics Avenue, Pittsfield, MA 01201 - Attn: Mr. D.G. Harrington (Rm. 1044) (1 copy)

General Research Corp., P.O. Box 3587, Santa Barbara, CA 93105 - Attn: Dr. R. Holbrook (1 copy)

General Research Corp., 1501 Wilson Blvd., Suite 700, Arlington, VA 22209 - Attn: Dr. Giles F. Crimi (1 copy)

Hercules, Inc., Industrial System Dept., Wilmington, DE 19899 - Attn: Dr. R.S. Voris (1 copy)

Hercules, Inc., P.O. Box 210, Cumberland, MD 21502 - Attn: Dr. Ralph R. Preckel (1 copy)

Hughes Research Labs., 3011 Malibu Canyon Road, Malibu, CA 90265 - Attn: Dr. D. Forster (1 copy)

Hughes Aircraft Co., Aerospace Group - Systems Division, Canoga Park, CA 91304 - Attn: Dr. Jack A. Alcalay (1 copy)

Hughes Aircraft Co., Centinela and Teale Streets, Bldg. 6, MS E-125, Culver City, CA 90230 - Attn: Dr. William Yates (1 copy)

Institute for Defense Analyses, 400 Army-Navy Drive, Arlington, VA 22202 - Attn: Dr. Alvin Schnitzler (1 copy)

Johns Hopkins University, Applied Physics Lab., 8621 Georgia Avenue, Silver Spring, MD 20910 - Attn: Dr. Albert M. Stone (1 copy)

Lawrence Livermore Laboratory, P.O. Box 808, Livermore, CA 94550 - Attn: Dr. R.E. Kidder (1 copy)
Dr. E. Teller (1 copy)
Dr. Joe Fleck (1 copy)

Los Alamos Scientific Laboratory, P.O. Box 1663, Los Alamos, NM 87544 - Attn: Dr. Keith Boyer (1 copy)

Lulejian and Associates, Inc., Del Amo Financial Center, 21515 Hawthorne Blvd. - Suite 500, Torrance, CA 90503 (1 copy)

Lockheed Palo Alto Res. Lab., 3251 Hanover St., Palo Alto, CA 94303 - Attn: L.R. Lunsford, Orgn. 52-24, Bldg. 201 (1 copy)

Mathematical Sciences Northwest, Inc., P.O. Box 1887, Bellevue, WN 98009 - Attn: Dr. Abraham Hertzberg (1 copy)

Martin Marietta Corp., P.O. Box 179, Mail Station 0471, Denver, CO 80201 - Attn: Mr. Stewart Chapin (1 copy)

Massachusetts Institute of Technology, Lincoln Laboratory, P.O. Box 73, Lexington, MA 02173 - Attn: Dr. S. Edulberg (1 copy)
Dr. L.C. Marquet (1 copy)

McDonnell Douglas Astronautics Co., 5301 Bolsa Avenue, Huntington Beach, CA 92647 - Attn: Mr. P.L. Klevatt, Dept. A3-830-BBFO, M/S 9 (1 copy)

McDonnell Douglas Research Labs., Dept. 220, Box 516, St. Louis, MO 63166 - Attn: Dr. D.P. Ames (1 copy)

MITRE Corp., P.O. Box 208, Bedford, MA 01730 - Attn: Mr. A.C. Cron (1 copy)

North American Rockwell Corp., Autonetics Div., Anaheim, CA 92803 - Attn: Mr. T.T. Kumagi, C/476 Mail Code HA18 (1 copy)

Northrop Corp., 3401 West Broadway, Hawthorne, CA 90250 - Attn: Dr. Gerard Hasserjian, Laser Systems Dept. (1 copy)

Dr. Anthony N. Pirri, Physical Sciences, Inc., 18 Lakeside Office Park, Wakefield, MA 01880 (1 copy)

RAND Corp., 1700 Main Street, Santa Monica, CA 90406 - Attn: Dr. C.R. Culp/Mr. G.A. Carter (1 copy)

Raytheon Co., 28 Seyon Street, Waltham, MA 02154 - Attn: Dr. F.A. Horrigan (Res. Div.) (1 copy)

Raytheon Co., Boston Post Road, Sudbury, MA 01776 - Attn: Dr. C. Sonnenschien (Equip. Div.) (1 copy)

Raytheon Co., Bedford Labs, Missile Systems Div., Bedford, MA 01730 - Attn: Dr. H.A. Mehlhorn (1 copy)

Riverside Research Institute, 80 West End Street, New York, NY 10023 - Attn: Dr. L.H. O'Neill (1 copy)
Dr. John Bose (1 copy)
(HPEGL Library) (1 copy)

R&D Associates, Inc., P.O. Box 3580, Santa Monica, CA 90431 - Attn: Dr. R.E. LeLevier (1 copy)

Rockwell International Corporation, Rocketdyne Division, Albuquerque District Office, 3636 Menaul Blvd., NE, Suite 211, Albuquerque, NM 87110 - Attn: C.K. Kraus, Mgr. (1 copy)

SANDIA Corp., P.O. Box 5800, Albuquerque, NM 87115 - Attn: Dr. Al Narath (1 copy)

Stanford Research Institute, Menlo Park, CA 94025 - Attn: Dr. F.T. Smith (1 copy)

Science Applications, Inc., 1911 N. Ft. Meyer Drive, Arlington, VA 22209 - Attn: L. Peckam (1 copy)

Science Applications, Inc., P.O. Box 328, Ann Arbor, MI 48103 - Attn: R.E. Meredith (1 copy)

Science Applications, Inc., 6 Preston Court, Bedford, MA 01703 - Attn: R. Greenberg (1 copy)

Science Applications, Inc., P.O. Box 2351, La Jolla, CA 92037 - Attn: Dr. John Asmus (1 copy)

Systems, Science and Software, P.O. Box 1620, La Jolla, CA 92037 - Attn: Alan F. Klein (1 copy)

Systems Consultants, Inc., 1050 31st Street, NW, Washington, D.C. 20007 - Attn: Dr. R.B. Keller (1 copy)

Thiokol Chemical Corp., WASATCH Division, P.O. Box 524, Brigham City, UT 84302 - Attn: Mr. J.E. Hansen (1 copy)

TRW Systems Group, One Space Park, Bldg. R-1, Rm. 1050, Redondo Beach, CA 90278 - Attn: Mr. Norman Campbell (1 copy)

United Technologies Research Center, 400 Main Street, East Hartford, CT 06108 - Attn: Mr. G.H. McLafferty (3 copies)

DISTRIBUTION LIST (Continued)

United Technologies Research Center, Pratt and Whitney Aircraft Div., Florida R&D Center, West Palm Beach, FL 33402 Attn: Dr. R.A. Schmidtke (1 copy)
Mr. Ed Pinsley (1 copy)

VARIAN Associates, EIMAC Division, 301 Industrial Way, San Carlos, CA 94070 - Attn: Mr. Jack Quinn (1 copy)

Vought Systems Division, LTV Aerospace Corp., P.O. Box 5907, Dallas, TX 75222 - Attn: Mr. F.G. Simpson, MS 254142 (1 copy)

Westinghouse Electric Corp., Defense and Space Center, Balt-Wash. International Airport - Box 746, Baltimore, MD 21203 - Attn: Mr. W.F. List (1 copy)

Westinghouse Research Labs., Beulah Road, Churchill Boro, Pittsburgh, PA 15235 - Attn: Dr. E.P. Riedel (1 copy)

United Technologies Research Center, East Hartford, CT 06108 - Attn: A.J. DeMaria (1 copy)

Airborne Instruments Laboratory, Walt Whitorian Road, Melville, NY 11746 - Attn: F. Pace (1 copy)

General Electric R&D Center, Schenectady, NY 12305 - Attn: Dr. Donald White (1 copy)

Cleveland State University, Cleveland, OH 44115 - Attn: Dean Jack Soules (1 copy)

EXXON Research and Engineering Co., P.O. Box 8, Linden, NJ 07036 - Attn: D. Grafstein (1 copy)

University of Maryland, Department of Physics and Astronomy, College Park, MD 20742 - Attn: D. Currie (1 copy)

Sylvania Electric Products, Inc., 100 Fergeson Drive, Mountain View, CA 94040 - Attn: L.M. Osterink (1 copy)

North American Rockwell Corp., Autonetics Division, 3370 Miraloma Avenue, Anaheim, CA 92803 - Attn: R. Gudmundsen (1 copy)

Massachusetts Institute of Technology, 77 Massachusetts Avenue, Cambridge, MA 02138 - Attn: Prof. A. Javan (1 copy)

Lockheed Missile & Space Co., Palo Alto Research Laboratories, Palo Alto, CA 94304 - Attn: Dr. R.C. Ohlman (1 copy)

ILC Laboratories, Inc., 164 Commercial Street, Sunnyvale, GA 94086 - Attn: L. Noble (1 copy)

University of Texas at Dallas, P.O. Box 30365, Dallas, TX 75230 - Attn: Prof. Carl B. Collins (1 copy)

Polytechnic Institute of New York, Rt. 110, Farmingdale, NY 11735 - Attn: Dr. William T. Walter (1 copy)